DESIGN AND FABRICATION OF HIGH-EFFICIENCY BINARY-PHASE DIFFRACTION GRATINGS FOR SPECTROSCOPIC AND BEAM SPLITTING APPLICATIONS

by

Uma Subash

A dissertation submitted to the faculty of
The University of North Carolina at Charlotte
in partial fulfillment of the requirements
for the degree of Doctor of Philosophy in
Optical Science and Engineering

Charlotte

2024

Approved by:

Dr. Menelaos K Poutous

Dr. Glenn D. Boreman

Dr. Tino Hofmann

Dr. Thomas Suleski

Dr. Fareena Saqib

ABSTRACT

UMA SUBASH. Design And Fabrication of High-Efficiency Binary-Phase Diffraction Gratings for Spectroscopic and Beam Splitting Applications. (Under the direction of DR. MENELAOS K POUTOUS)

Binary-phase diffraction gratings are optical components that distribute an incident light beam to diffraction-order directions, due to the periodic modulation of the refractive index within the grating volume. Gratings are essential components in fields like acousto-optics, holography, spectroscopy, and are typically fabricated using lithography. High-efficiency first-order gratings are particularly important in spectroscopy, since first-order spectral diffraction spatially separates the incident wavelengths to be measured.

Designing a linear grating consists of iterations of numerical simulations for a given phase profile, to determine grating diffraction efficiencies. The inverse design process, specifying the efficiencies desired and obtaining the phase profile, is very challenging and can lead to unstable solutions. In this research effort, a two-step design process is used. The general parameter ranges are determined first based on design goals, and then more rigorous simulations are performed to "map-out" the diffraction efficiency as a function of a limited solution parameter-space search. The phase profile that matches the design goals is then chosen.

The first lithographic step in grating fabrication is to create a mask for the grating's features on a photoresist and develop the device profile. Etching the features into the substrate with a reactive-ion plasma process results in a permanent optical component. The study addresses certain fabrication challenges in binary grating fabrication, associated with areal scaling from a 25×25 mm^2 surface area to a much larger 101×101 mm^2 desired component size. The greatest challenge is to achieve the proper etch depth for the device function, which is mitigated by multiple masking and etching steps.

The Littrow-mount configuration is commonly employed to enhance a grating's first-order efficiency performance, but can cause ghost images due to light recombination, a problem often controlled with antireflective treatments. Part of the research effort presented here uses random antireflective surface structures (rARSS), which are randomly distributed conical nano-features, etched into dielectric surfaces to minimize their Fresnel reflectivity. These structures were fabricated and tested on cylindrical lenses and freeform elements, showing significant transmission enhancement in the visible spectrum, minimal wide-angle scattering losses, and no notable wavefront distortion. rARSS were then applied to proof-of-concept (POC) reactive-ion plasma-etched (RIPLE) gratings for the VIRUS2 spectrograph, which was designed for Littrow-mount configuration. The rARSS-treated gratings successfully suppressed the undesirable reflection from the zeroth-diffraction order, enhanced the transmitted first-order, and reduced Littrow ghost intensities to four orders of magnitude lower than the transmitted spectrum baseline.

In parallel, a grating beam splitting device composed of two alternating crossed-cell-tile first-order diffraction gratings, oriented orthogonal to each-other, was fabricated to function as both a two-way and three-way beam splitter at oblique light incidence. The tiling spatially separates the first-diffraction orders of each grating cell group, while it overlaps the undeflected zeroth-diffraction order, creating three light-splitting pathways in orthogonal directions in three-dimensions. Each grating type was optimized to separate light in the $1^{st}-$ and $0^{th}-$diffraction order, in ratios 96:1 and 2:1 for the two-way and three-way beam splitter respectively. The result was the projection of three equal intensity spots in space for the three-way beam splitter, and two spots off the axial direction for the two-way beam splitter.

ACKNOWLEDGEMENTS

This dissertation would not have been possible without the support and assistance of many individuals. First and foremost, I extend my sincere thanks to my advisor, Dr. Menelaos Poutous, for his exceptional mentorship and unwavering support throughout these five years of my doctoral journey. I couldn't have asked for a better advisor. I would also like to thank my committee members, Dr. Glenn Boreman, Dr. Tino Hoffman, Dr. Tom Suleski and Dr. Fareena Saqib for their time, expertise, encouragement and constructive critiques that helped me shape my research.

I am deeply grateful to Dr. Hanshin Lee for his collaborations and generous support throughout. Thank you McDonald Observatory and University of Texas Austin for the financial support which made this research possible.

I would like to thank the past and present members of my group Dr. Suba Srenevas, Samir Paudel, Dr. Praneeth Gadamsetti and Dr. David Gonzalez for their training and support. I extend my heartfelt thanks to my dear friend and collaborator Dr. Paige Stinson. Our late night brainstormsing sessions and hours of working together have made this journey not just productive but also memorable.

I am thankful to the Center for Optoelectronics and Optical Communications at UNC Charlotte for their facility support. Special thanks to Mr. Scott Williams, Dr. Lou Deguzman, Dr. Tom Hutchens, Mr. Daniel Furr and Dr. Jeffrey Thomas who never failed to assist with the instruments.

Thank you beloved Amma, Achan and Malu for being this incredible family and always believing in me. Without your support I would not have achieved this milestone.

A huge shoutout to my amazing friends, Anna, UV, Laya and Anuja for being my unofficial therapists. Over these five years, you guys have been there for me through every high and low, even from miles away. Our video calls have been a lifeline.

Atlast but not the least, I would like to thank myself for countless hours of persistence, powering through existential crises, and managing to avoid a complete break-

down. Thankyou, me, for sticking it out and not giving in to the tempting urge to buy a one-way ticket back to my home country.

TABLE OF CONTENTS

LIST OF FIGURES x

LIST OF TABLES xvi

CHAPTER 1: INTRODUCTION 1

1.1. Overview 1

1.2. Fabrication using reactive ion plasma etching 4

1.2.1. Fabrication of antireflective nanostructures 4

1.2.2. Fabrication of micro gratings 5

1.3. Littrow configuration 7

1.4. Harvey's model for Conical incidence 7

1.4.1. Case I: Normal incidence 10

1.4.2. Case II: Principal plane of incidence 11

1.4.3. Case III: Oblique incidence 12

1.4.4. Case IV: Rotation along grating normal 13

References 15

CHAPTER 2: ANTI-REFLECTIVE MODIFICATION OF FREEFORM ELEMENTS AND CYLINDRICAL LENSES 18

2.1. Introduction 18

2.2. Fabrication 20

2.3. Test methods 21

2.4. Results 24

2.4.1. Component Transmission Enhancement 24

2.4.2. Component Wavefront Measurements 26

2.4.3. Component Surface Scatter 30

2.5. System-level performance evaluation of the rARSS 32

2.6. Conclusion 34

References 37

CHAPTER 3: REACTIVE-ION PLASMA-ETCHED GRATING 42

3.1. High-efficiency first-order grating for Astronomical applications 42

3.1.1. Introduction 42

3.1.2. Design, Fabrication, and Grating Characterization 44

3.1.3. Spectral measurements 47

3.1.4. Results and Conclusion 49

3.2. Reduction in Littrow recombination ghosts in 1st order gratings 52

3.2.1. Introduction 52

3.2.2. Fabrication and Testing 53

3.2.3. Results 54

3.2.4. Conclusion 59

3.3. Large surface area grating fabrication 60

3.3.1. Fabrication difficulties 61

3.3.2. Proposed Solution 63

3.3.3. Results 64

3.3.4. Conclusion 66

References 68

CHAPTER 4: CROSSED-CELL-TILE MULTIPLEXED 1ST-ORDER GRATINGS FOR THREE-DIMENSIONAL BEAM-SPLITTER APPLICATIONS 70

4.1. Introduction 70

4.2. Conical diffraction by crossed-cell-tile gratings 72

4.3. First-order grating cell design 76

4.3.1. Two-way beam splitter grating cell-tiles 80

4.3.2. Three-way beam splitter grating cell-tiles 82

4.4. Fabrication and test of crossed-cell-tile grating beam splitters 84

4.4.1. Fabrication of crossed-cell-tile devices 84

4.4.2. Performance of three-dimensional beam splitter devices 85

4.5. Conclusions 89

References 91

CHAPTER 5: SUMMARY AND OUTLOOK 95

5.1. Future work : Polarization beam splitter design 97

LIST OF OWN PUBLICATIONS 100

LIST OF FIGURES

FIGURE 1.1: Sequential steps involved in electron-beam direct-write lithography process. A) Mask pattern is written using an electron-beam exposure of a thin photoresist layer, over-coating a 110 nm thick metallic chromium layer deposited on the quartz substrate. B) The unexposed regions of photoresist protect the chromium metal underneath the pattern from the liquid Cr-etchant. C) The excess resist is stripped off leaving a hard chrome mask on quartz. D) Reactive-ion plasma etch of the exposed substrate, followed by chromium metal removal results in a permanent quartz grating lithographic pattern. 6

FIGURE 1.2: A) Littrow condition in a reflective grating with period Λ and fillfactor f. B) Bragg condition in a transmissive grating 7

FIGURE 1.3: Far-field planar projection of transmitted diffraction orders from a grating for: A) Principal Plane Incidence (PPI) and, B) oblique incidence. 9

FIGURE 1.4: Diffraction effects at normal incidence represented in: A) real space with Cartesian coordinates xyz, B) configuration space with direction cosines $\alpha\beta\gamma$. Only one of the possible DO wave vectors is shown for reflection or transmission. 11

FIGURE 1.5: Diffraction effects at θ_i incidence within PPI represented in: A) real space with Cartesian coordinates xyz and, B) configuration space with direction cosines $\alpha\beta\gamma$. 12

FIGURE 1.6: Diffraction effects at θ_i incidence, out of PPI along the yz plane, represented in the A) real space with Cartesian coordinates xyz B) configuration space with direction cosines $\alpha\beta\gamma$ 13

FIGURE 1.7: Diffraction effects at normal incidence, when grating is rotated at an angle θ_i along the normal, depicted in the A) real space with Cartesian coordinates xyz B) configuration space with direction cosines $\alpha\beta\gamma$ 13

FIGURE 2.1: Top-down view of the CASI scatterometer layout used to measure the scatter of the freeform element before and after etch. The BTDF is measured sweeping the detector along the circular path from -90° to +90°. The inset shows the test locations on the freeform component surface facing the light source. The coordinate reference applies to the scatterometer. 23

FIGURE 2.2: Normal incidence axial transmission measurements, averaged across samples, for: (A) PCV lenses, (B) PCX lenses and, (C) the FF elements with 1 nm wavelength resolution. The pre-processed measurements are shown in gray and the rARSS double-sided enhanced measurements are in black. The bars indicate the within-set maximum to minimum range measurements for each wavelength, and are shown in 25 nm wavelength intervals. 25

FIGURE 2.3: Comparative wavefront measurements for all PCX and PCV cylindrical lenses, before (circles) and after (bold font crosses) rARSS enhancement. Fractional deviation of: (A) Wavefront PV amplitude of the cylindrical profile, $\delta(pv)$; (B) Defocus Zernike coefficient $\delta(Z5)$ and; (C) Astigmatism Zernike coefficient $\delta(Z6)$. The bars indicate the maximum deviation range of measurements across time (days). Thin bars belong to the pre processing evaluation and thick bars to post processing tests. The horizontal dashes indicate component specification limits. 27

FIGURE 2.4: Pixel to pixel wavefront measurements of PCXs and PCVs post process with rARSS shown on the left column, and the residual wavefront (pixel to pixel difference in wavefront of pre- and post-processed cylindrical components) shown on the right for four different lenses: a) PCX1, b) PCX2, c) PCV3 and d) PCV4. The colorbar on each figure represents the convexity or concavity of the wavefront in μm from the base at 0 μm. The residual wavefront is within the baseline uncertainty (no sample) wavefront of the SH detector (0.4μm sag.) 29

FIGURE 2.5: BTDF measurements from the freeform element locations tested as shown in the inset of Figure 1, compared with the instrument's signature. The BTDF scale is logarithmic. (A) BTDF measurements displayed as a function of the angle of collection (θ_s). (B) BTDF measurements displayed as a logarithmic function of the angular parameter β_s to accentuate comparisons in the axial direction. The vertical dotted line indicates the angular extent of the instrument's test beam. 31

FIGURE 2.6: BRDF measurements from a fused silica flat (FS flat), compared with a fused silica flat with added ARSS on both surfaces (FS+ARSS). The BRDF measurements were taken at -15° angle-of-incidence (AOI) and are displayed as a logarithmic function of the angular parameter β_c with respect to the surface normal.The incident beam has a full angular width of 6°(w). 31

FIGURE 2.7: Reprinted with permission from [19]. Arrayed wide-angle corrector system made of segmented relay units each of which contains the cylindrical lens pair and freeform component for system level testing. 33

FIGURE 2.8: (Left) End-to-end spectral transmission measurements of AWACS-Duo units: U1 (yellow line and bullets) and U2 (brown line and bullets), including the model prediction (blue line and bullets). The results for U1 and U2 are overlapping. (Right) Per-surface transmission estimate of different anti-reflective treatments applied to U2 components, based on spectral transmission measurements from component substitutions discussed in the text. 34

FIGURE 3.1: Schematic of a diffraction grating in transmission with period Λ. 43

FIGURE 3.2: Reprinted from [1]. Efficiency of 1^{st}-order for the design of a "green" grating A) as a function of wavelength (λ), grating depth (d) and gap width (w/p) B) as a function of λ and d at optimum w/p and C) as a function of λ for optimum d. 45

FIGURE 3.3: Reprinted from [1]. Left: 1x1 sq. inch grating diced into 9 small proxy gratings for tuning the etching parameters. Right: The final 1x1 sq. inch POC-RIPLE grating after wet chrome etch. The proxies in the figure still have chrome on. 47

FIGURE 3.4: Reprinted from [1]. Depth analysis by comparison of measured (orange) 0^{th} order transmission spectra to numerically simulated (black and grey) one for the A) s polarization and B) p polarization both indicating a depth of 1.25 μm. C) Scanning Electron Microscope (SEM) image of the grating with 1.25 μm high pillars and 567 nm spacing 48

FIGURE 3.5: Layout of the WVASE instrument. The detector moves around the dotted line within mechanical limits. The POC RIPLE on a rotating holder along the y-axis allows precise incidence angle adjustment. The 0^{th} order aligns with the source for accurate measurement, while the 1^{st} order may deviate slightly due to grating alignment errors, making it harder to measure accurately. 49

FIGURE 3.6: Comparison of the measured (solid) and simulated (dotted) 0^{th} order transmission spectra of the numerical model and actual POC RIPLE grating at normal incidence for the A) p polarization and B) s polarization. C) Measured transmission spectra at 36.4°angle of incidence for C) the 0^{th} order at both polarizations shown in logarithmic scale and D) the 1^{st} order at u polarization 50

FIGURE 3.7: Enhancement upto 3% in the transmission of quartz witness sample after rARSS treatment (Green curve) compared to the unprocessed quartz (Black Curve). Green shaded region shows the operational wavelength range of the grating where the rARSS performance is featureless and enhanced. 55

FIGURE 3.8: Near-Littrow incidence test mounting for the grating with the grating facing (A) the detector and (C) the source. The incidence (k_i), the axial 0^{th}-order (k_0), and -1^{st}-order diffraction ($k_{\underline{1}}$) directions are indicated. BTDF in logarithmic scale as a function of the angle of collection for the grating facing (B) the detector and (D) the source. The signature (baseline) of the CASI instrument is shown as white data points along the axial direction. Fabrication artifacts (FA) are identified adjacent to the propagating orders. 56

FIGURE 3.9: Measured BTDF for $\pm 2^{\circ}$ near the: (A) -1^{st} and (B) 0^{th} orders for two different orientations of the grating. The Littrow recombination ghosts correspond to the directions in Fig.3.8A and C . 58

FIGURE 3.10: A) Proxy gratings of 2 inch ('V') and the 4 inch target grating ('U') shown with their dimensions marked. B) Depth of the grating as a function of time of etch for different sizes of proxy gratings shown in different colors. The green horizontal line is the target depth of the design and red dotted line is the maximum etch time affordable without Chrome layer depletion. 62

FIGURE 3.11: Iterative step technique of chrome redeposition off axis on shallow reactive ion etched gratings followed by another plasma etch to achieve deeper grooves. 64

FIGURE 3.12: Transmission spectra of the p-polarization of three proxy gratings A, B and C before (solid black) and after (solid red) iterative chrome redeposition process. Depth analysis done using RCWA with numerical simulations shown in dotted curves. D) Master Contour plot of transmission spectra as a function of depth with red dotted lines representing the curves in A, B and C indicated by green arrows. 65

FIGURE 3.13: Transmission spectrum of the highly efficient 1^{st} order (shown in red) and 0^{th} order (shown in black) of the 101.6×101.6 mm^2 RIPLE grating at A) 29° and B) 36° angle of incidence. 66

FIGURE 4.1: A) Direction cosine $\alpha\beta\gamma$-space unit-hemisphere illustrating the transmission DO angular distribution for oblique incidence directions α_i, β_i, γ_i. The grating vector direction is represented by a single point: $\alpha_K = 1$ (with lines parallel to the laboratory y-axis as shown in the inset.) The inset shows the laboratory frame-grating orientation. B) The direction cosine $\alpha\beta$-plane, where the DO projections are equally spaced, along a single line parallel to the α-axis for the conditions shown in the inset. 73

FIGURE 4.2: A) Crossed-cell-tile grating device with two $1^{st}-$order gratings G1 and G2 (blue and red respectively) tiled in an alternating orthogonal pattern. Similar grating tiles are placed at a center-to-center distance of integer multiples (p, q) of the incident wavelength value. B) The $\alpha\beta$-plane in direction-cosine space for the tiled pattern, separating the $1^{st}-$DO shown as red and blue dots and the overlapping $0^{th}-$DO. The empty bullets outside the unit circle are evanescent higher-DO. 74

FIGURE 4.3: Surface contour plots of $F(n_{eff})$ in amber, and the plane $cos(\kappa\Lambda)$ in blue, for the grating cell design G1, from equations **??** as a function of the effective refractive index n_{eff} and normalized fill factor d_1/Λ, for: A) TE polarization and, B) TM polarization. The solid black lines represent the $1^{st}-$DO solutions and the dotted black lines are for the $0^{th}-$DO solutions satisfying the AOI and periodicity from section 4.2. 79

FIGURE 4.4: Effective refractive index, n_{eff} as a function of the grating period-normalized fill factor, for: A) Grating G1 and B) Grating G2. The four different curves correspond to the TE and TM polarizations of the $0^{th}-$ and $1^{st}-$DO. 79

FIGURE 4.5: The difference in the effective refractive index, Δn_{eff}, between the 0^{th} and $1^{st}-$ DO as a function of the normalized fill factor d_1/Λ, for: A) cell G1 and B) cell G2, from the values in figure 4.4. The range of Δn_{eff} values where the TE and TM curves are nearly overlapping (red highlight) corresponds to the range of optimum fill factor values (blue highlight). 81

FIGURE 4.6: RCWA computed diffraction efficiency contour plots of the $1^{st}-$DO (η_{+1}) as a function of depth and fill factor, for TM and TE polarization (left and right columns) of grating G1 and grating G2 (top and bottom rows), for the two-way crossed-cell-grating beam splitter. The red dot represents the chosen common depth (1.15μm) and fill factor (0.56) on all four graphs, that yield diffraction efficiencies η_{+1} >90%. 82

FIGURE 4.7: RCWA computed transmission diffraction efficiency for the $1^{st}-$DO as a function of grating depth, for both gratings G1, G2, and both incident polarizations. Right: Expanded view of the efficiency range: $0.50 < \eta_{+1} < 0.75$. At depth 650 nm, shown by the vertical dotted line, the efficiencies are within the desired range of 0.58-0.69. 84

FIGURE 4.8: A) Schematic of the test setup used for oblique angle of incidence. HWP is the half-wave plate, LP is the linear polarizer, and LA is the linear polarization analyzer. B) Photograph of the three-way beam splitter device block (D), tested at 633 nm. The projection of the three DO after conical diffraction is shown on a square-grid paper card. The 1-in. grid divisions on the card are visible for location comparison. 86

FIGURE 4.9: Detected polarization state polar plots of: A) the diffracted η_{+1} of the two-way beam splitter and, B) the η_0 of the three-way beam splitter, for a 360° rotation of the analyzer in steps of 10°. The red dotted lines show the alignment of the lobes to the incident polarization state, and the red dotted circles indicated the peak efficiency for each device. The maximum efficiency shown in the radial direction is 0.50. 88

FIGURE 5.1: RCWA simulated efficiency contours of the 1^{st}-DO (η_{+1}) as a function of depth and fill factor for: A) grating G1 at TE polarization and, B) TM polarization. 98

LIST OF TABLES

TABLE 2.1: Spectral normalized-transmission ranges, and peak transmission values with ranges, for the lens and FF sets from the measured test data shown in Figure 2.2. 24

TABLE 2.2: Across-sample measured global averages for PV, Z_5, and Z_6, pre- and post-rARSS processing, over all days of measurement. Values shown are in μm. 28

TABLE 3.1: Integrated suppression ratios of the ghost orders w.r.t first order 58

TABLE 4.1: RCWA-simulated diffraction efficiencies of the 0^{th} (η_0) and $1^{st}-$DO (η_{+1}) at a grating depth of 650 nm, for both the grating cells (G1, G2) of the three-way beam splitter device. 84

TABLE 4.2: Efficiencies of the DO from both beam splitter devices. 87

CHAPTER 1: INTRODUCTION

1.1 Overview

The emergence of diffraction gratings dates back to the 18th century, when in 1786 F. Hopkinson made a groundbreaking observation. He noticed unusual patterns of light from a street lamp when viewed through a silk handkerchief held between his hands. Subsequent experiments replicated this phenomenon using man-made diffraction gratings. Today, diffraction gratings are essential tools in spectrometry, contributing significantly to a range of applications-from examining individual biomolecules to analyzing celestial objects in space. They are used in the fields of acoustooptics, holography, data processing, integrated optics, spectroscopy, beam splitting, image processing, multiplexing, demultiplexing, beam shaping, beam expansion and so on [1].

For most applications, the fabrication of high-quality diffraction gratings requires precise control of the period at a nanometer scale. Holographic gratings, where the interference pattern of two superimposing coherent beams were recorded on a photographic plate, was one of the earliest fabrication techniques used [2, 3]. A major issue with optical lithography is that holography captures interference patterns caused by defects like dust, digs, and scratches on the optics, leading to low-contrast ghost holograms on grating modulations. Additionally, photopolymers used for holographic gratings are less thermally and mechanically stable than glass. Electron-beam direct-write lithography techniques generating photomasks on quartz substrates, followed by reactive ion plasma etching, on the other hand defines precise-scale features into the substrate surface making them more durable. The electron-beam lithography technique used throughout this work is presented in section 1.2.2.

Diffraction gratings are vital in astronomical spectroscopy because they use their first-order diffraction to spatially separate the spectrum for spectroscopic measurements [4]. To obtain strong signals from faint astronomical sources, it is essential to optimize the grating's first-order diffraction efficiency. The Littrow mount is widely employed in spectrometers and other optical systems where enhancing spectral resolution and light collection efficiency is essential [5]. This configuration is achieved when light strikes the grating at the Littrow angle, causing the first-order diffracted light in reflection to retrace the incident path (as detailed in Section 1.3). This alignment optimizes diffraction efficiency, particularly for the first order.

However, the Littrow configuration has some drawbacks, such as Littrow recombination ghosts, which are caused by unwanted reflections from the back of the substrate that re-enter the spectrographic optical system [6]. To mitigate these ghost images, applying an antireflective coating to the backside of the substrate is an effective solution. Among the various antireflection techniques for quartz materials, we investigated random antireflective surface structures (rARSS). These structures consist of randomly distributed, densely packed, subwavelength nanostructures that are monolithically etched into the substrate's surface. They are inspired by the "moth eye" structures seen naturally in the cornea of certain moths, known for their broadband antireflective properties [7]. The rARSS structures induce an effective gradient in the refractive index boundary from air to substrate, due to the gradual increase in the ratio of glass to air volume. This gradual transition in refractive index reduces reflective losses and enhances transmission through the interface [8]. For analysis, the rARSS can be approximated using an effective medium layer model. The rARSS also exhibit other properties like polarization insensitivity [9], low wide angle scattering [10], low narrow angle reflection [11] etc.

Chapter 2 concentrates in evaluating the antireflective efficiency of random rARSS applied to a set of cylindrical and freeform optical elements. In addition to improving

component transmission, the study also investigated whether the rARSS fabrication process introduced any wavefront distortion or scattering effects. Unlike previous research that mainly assessed optical transmission performance, this chapter also explores system-level impacts of optical elements with rARSS. End-to-end spectral and imaging tests were conducted using the enhanced elements in a wide-field astronomical camera system assembled with the Harlan J. Smith Telescope (HJST) at McDonald Observatory in Texas. This effort was the first to report on functional performance of broadband antireflective freeform elements with rARSS, highlighting its potential as a superior alternative to thin-film coatings for imaging and spectroscopic systems.

In Chapter 3, the fabrication of random antireflective surface structures on a prototype Reactive-Ion Plasma-Etched (RIPLE) grating with a 25×25 mm^2 surface area is presented. The RIPLE grating, part of the spectral channels ("blue", "green", "red", "deep red") for the new VIRUS2 spectrograph unit of the 2.7m Harlan J. Smith Telescope (HJST), was designed to operate in the Littrow configuration for optimal first-order efficiency. The rARSS treatment on the backside of the grating was meant to mitigate the Littrow recombination ghosts. The chapter details an investigation into mapping the positions and suppression of ghosts orders of the RIPLE grating via angular scatter measurements at near-Littrow incidence. Notably, there were no reports prior to this effort making scatterometric measurements for astronomical high-resolution spectrographic gratings. The final section discusses efforts to scale up the RIPLE gratings to meet the demands of extra-large telescopes, which require larger surface areas due to their larger beam sizes. The area of the gratings was increased from the 25×25 mm^2 proof of concept to a 101.6×101.6 mm^2 target size. This section also addresses the fabrication challenges encountered during this effort and describes an iterative etching technique that was adopted to address these challenges.

After gaining experience with large area lithographic grating fabrication techniques,

Chapter 4 presents the design and fabrication of a versatile crossed-cell-tile grating device that can function as a two-way, three-way and polarization beam splitter, at oblique angles of incidence for the visible wavelength regime. The design features alternating tiles of two first order gratings with their lines perpendicular to each other, effectively spatially separating the two first orders in separate orthogonal planes while the zero orders overlap. The Simplified Modal Method (SMM) was employed for the first time at oblique angles of incidence for the preliminary design of the devices. Rigorous couple wave analysis (RCWA) was later used to accurately optimize the grating parameters by simulations. The diffraction angles were predicted using Harvey's conical incidence model, expressed in terms of direction cosines in three dimensions. This model is detailed in Section 1.4 of the present chapter, to provide a clearer understanding of the design method used in Chapter 4. The key outcomes of these studies, as well as, future project directions are discussed in Chapter 5.

1.2 Fabrication using reactive ion plasma etching

Standard lithographic fabrication techniques comprises two main steps: the writing step and the etching step. The writing step involves generating a metal mask on the substrate surface, while the etching step removes the exposed areas to create the desired pattern. In this study, lithography is employed as the primary fabrication technique and is used in two distinct contexts: to create ordered structures, such as diffraction gratings, and disordered structures, like random antireflective structured surfaces. The key difference between these applications lies in the writing step, while the reactive-ion plasma-etching step remains similar for both implementations.

1.2.1 Fabrication of antireflective nanostructures

For random nanostructures, the writing step involves a straightforward process where the samples are coated with a thin, porous layer of gold (Au), using the AJA International ATC 1800-F sputter deposition system. This gold layer acts as a par-

tial mask for the substrate etching process. The samples are then subjected to a reactive-ion plasma-etch (RIPLE) which is a dry plasma etching process [12]. A vacuum chamber, with two large-surface electrodes powered by a radio frequency (RF) power supply, is required for the process. The sample is placed on the cathode electrode. A mixture of reactive gases, selected based on the substrate of the sample, is pumped into the chamber with a fixed flow rate. For silicon-containing substrates such as quartz, gases with fluorine chemistry such as sulphur hexafluoride (SF_6), trifluoromethane (CHF_3) or octafluorocyclobutane (C_4F_8), are typically employed. The RF-driven power signal has two effects: a) it ignites the plasma, stripping electrons off of the reactive gas molecules, thereby creating a mixture of radicals, free electrons, and positive ions, and b) it creates a bias electric field between the electrodes that is perpendicular to the sample surface. Due to the electric field, a negative charge accumulates on the substrate. This draws the positive ions from the plasma to accelerate towards the substrate thereby removing the substrate molecules due to ion bombardment. There is also some level of etching by the chemical reaction of the gases with the substrate. The volatile byproducts from these reactions are exhausted out of the chamber continuously. Gases like Oxygen (O_2), which increases the fluorine concentration by reacting with Carbon and Sulphur that would otherwise bond with fluorine, is used to expedite the process. During the RIPLE process, the exposed nanopores in the gold mask are etched into columnar nanostructures, forming the random antireflective nanostructures.

1.2.2 Fabrication of micro gratings

The writing step for the ordered structures, such as gratings, as shown in Figure 1.1, was relatively complex and involved e-beam writing for mask formation. A standard quarter-inch thick quartz substrate was initially coated with 110 nm of chromium metal, followed by an e-beam sensitive photoresist layer coating. The photoresist layer decomposes upon exposure. The e-beam exposure tool thus “wrote” the grating

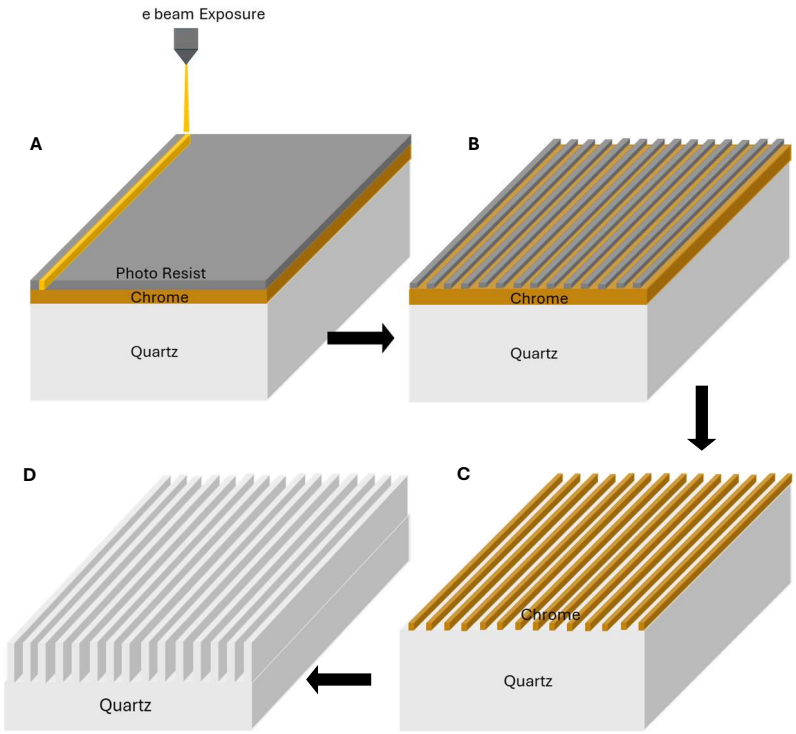

Figure 1.1: Sequential steps involved in electron-beam direct-write lithography process. A) Mask pattern is written using an electron-beam exposure of a thin photoresist layer, over-coating a 110 nm thick metallic chromium layer deposited on the quartz substrate. B) The unexposed regions of photoresist protect the chromium metal underneath the pattern from the liquid Cr-etchant. C) The excess resist is stripped off leaving a hard chrome mask on quartz. D) Reactive-ion plasma etch of the exposed substrate, followed by chromium metal removal results in a permanent quartz grating lithographic pattern.

mask pattern onto the photoresist. The exposed photoresist was washed away using a developer solvent (Figure 1.1B.) This step revealed the chromium metal layer under the pattern of the grating, which was then chemically etched using a chromium liquid etchant. During this step, the remaining photoresist acted as a mask to protect the chromium metal underneath the grating pattern from removal. The quartz beneath the etched chromium layer was exposed. The remaining photoresist was completely stripped off after this process, leaving a hard chromium metal mask on quartz, as shown in Figure 1.1C. Finally, the hard chromium mask underwent a reactive-ion plasma-etching process, similar to the method used for creating antireflective nanos-

tructures. After the process, excess chromium metal is removed using a chemical liquid Chromium etchant. Figure 1.1D shows the final product of the RIPLE process, forming a binary phase transmission grating.

1.3 Littrow configuration

The Littrow configuration mounting is a specific arrangement, as shown in Figure 1.2A, for a diffraction grating with a spatial period Λ, and a fill factor f. When light is incident at the Littrow angle θ_L, the diffracted first order in reflection retraces the path of the incident beam. The term "Littrow" is commonly used for reflective gratings where maximum efficiency of light is directed into a desired diffraction order in reflection. In transmission, this configuration is known as the Bragg condition as illustrated in Figure 1.2B. When light is incident at the Bragg angle θ_B, the diffracted 0^{th} order and -1^{st} order have same magnitude of diffraction angle (equal to the Bragg angle) but are in opposite sense of direction. This configuration ensures first order maximum transmission efficiency, well-suited for applications such as laser resonators, couplers, monochromators, and spectrometers etc.

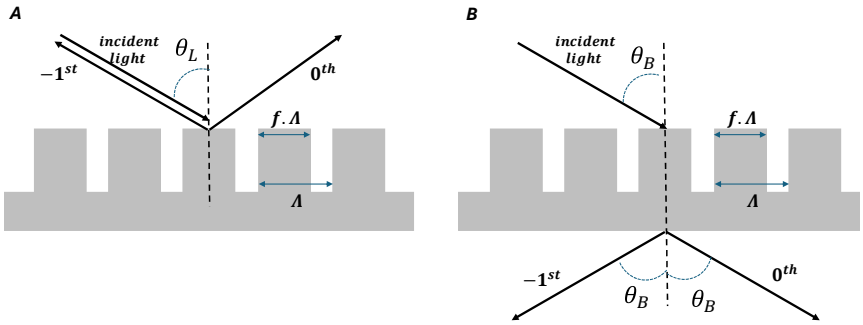

Figure 1.2: A) Littrow condition in a reflective grating with period Λ and fillfactor f. B) Bragg condition in a transmissive grating

1.4 Harvey's model for Conical incidence

The behaviour of gratings at oblique incidence is discussed in this section which will be insightful for the design study in Chapter 4. Gratings are typically operated

at incidence within the principal plane of incidence (PPI), which contains the incident light wave-vector (k_i), the grating vector (K), the normal to the grating surface (N), and all diffracted order vectors as shown in Figure 1.3A. Conventionally the PPI coincides with the xz-Cartesian laboratory reference plane. For small paraxial angles of incidence (AOI), defined for incidence nearly normal to the grating plane and the grating vector, the diffraction orders (DO) are equally spaced and remain invariant with respect to small AOI changes. In contrast, for angles of incidence within the PPI wider than 8° (0.14 rad) the diffraction orders are neither equally spaced nor incidence angle shift-invariant. However, in both cases the diffracted orders align on a single line contained in the PPI, and for a thin grating surrounded by air, the DO off-axis deflection is expressed by the conventional two-dimensional diffraction equation: $sin\theta_i \pm sin\theta_p = p\lambda/\Lambda$; for $p = 0, \pm1, \pm2, ...$ is an integer representing the diffraction order rank, θ_p is the diffracted angle of order p, θ_i is the AOI and Λ is the grating period. In the equation above, the positive sign corresponds to reflected orders, the negative sign to transmitted orders, and the angles of incidence and deflection are measured from the grating-surface normal, which is chosen in opposite direction between transmission and reflection. This induces a symmetry inversion with respect to the transmission and reflection angles θ, φ.

When the AOI is oblique to the plane containing the grating vector and the surface normal as shown in Figure 1.3B, the diffracted orders distribute as a conical section in space, and therefore the two-dimensional grating equation above is not valid. A modification of the grating equation in three-dimensions is required, and as oblique incidence is usually considered for arbitrary AOI, conical diffraction is treated with non-paraxial analysis. Harvey linearized conical diffraction using a variable substitution across the diffracting aperture, which was equivalent to a coordinate transformation from physical space xyz to direction-cosine angular space $\alpha\beta\gamma$ [13]. Harvey also scaled the Cartesian variables using the incident wavelength λ as a normalization con-

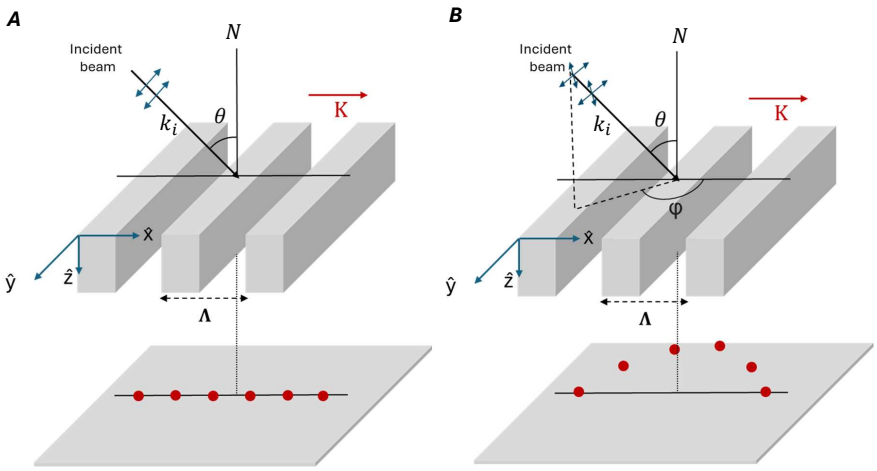

Figure 1.3: Far-field planar projection of transmitted diffraction orders from a grating for: A) Principal Plane Incidence (PPI) and, B) oblique incidence.

stant, yielding new dimensionless coordinate variables: $\hat{x}, \hat{y}, \hat{z}$[14]. The dimensionless variable pairs: $(\hat{x}, \alpha)$,$(\hat{y}, \beta)$,$(\hat{z}, \gamma)$ are conjugate pairs in the Fourier-integral transform that describes grating diffraction. The subtlety is that the calculated diffracted field resides on a spherical surface centered on the aperture, not on a projection plane parallel to the aperture. The direction cosines of a general three-dimensional vector r in real space (or $\hat{r}$ in real wavelength-normalized space) are represented by the direction cosines α, β and γ:

$$\alpha = sin\theta cos\varphi = x/r = \hat{x}/\hat{r}, \beta = sin\theta sin\varphi = y/r = \hat{y}/\hat{r}, \gamma = cos\theta = z/r = \hat{z}/\hat{r} \quad (1.1)$$

which are the projections of vector r on the Cartesian laboratory frame, and r, θ, φ are the spherical-polar coordinates in the same frame. In passing we note that the convention used with ray-tracing software is to measure the sign of the DO deflection angles from the grating output surface-normal to the DO trajectory, and not from a fixed polar laboratory-frame z-axis, which induces a sign reversal for the angles in the set of equations above and requires the substitution: $\theta \rightarrow -\theta$, $\varphi \rightarrow -\varphi$. The direction cosines α_i, β_i used here are negative when converted to Harvey's notation

[15]. The transmission grating equations expressed in direction-cosine variables are:

$$\alpha_p = \alpha_i + p(\lambda/\Lambda)\alpha_K \tag{1.2a}$$

$$\beta_p = \beta_i + p(\lambda/\Lambda)\beta_K \tag{1.2b}$$

$$\gamma_p = \pm\sqrt{1 - \alpha_p^2 - \beta_p^2} \tag{1.2c}$$

where α_K and β_K are the projections of the grating vector $\mathbf{K}$ to the fixed laboratory frame [16]. The direction cosines $\alpha_i, \beta_i, \gamma_i$ represent the projections of the incident beam. The sign of γ_p is positive for transmission DO and negative for reflection DO, for $1 \geq \mid \gamma_i \mid > 0$. The values of direction cosine γ_p are not independent, and are restricted to real values within the unit sphere that spans the configuration space $\alpha\beta\gamma$, but they can be negative or positive depending on the relative orientations of the incident, reflected and transmitted wave-vectors. If γ_p becomes imaginary for large values of $\pm p$, the propagating wave is attenuated, resulting in evanescent diffracted orders. The behaviour of diffraction orders in the configuration space $\alpha\beta\gamma$ for four different cases of incidence are explained below:

1.4.1 Case I: Normal incidence

Figure 1.4A shows the diffraction pattern in real space with the grating resting in the xy-plane, under normal incidence conditions. In this setup, θ_p and θ'_p represent the diffraction angles for transmission and reflection, respectively. The propagation vectors $\mathbf{k_p}$ and $\mathbf{k'_p}$ for the transmissive and reflective diffraction orders lie in the same plane as $\mathbf{K}$, $\mathbf{N}$, and $\mathbf{k_i}$, which defines the principal plane of incidence. Figure 1.4B depicts the diffraction orders in configuration space. Each point on the unit sphere's surface corresponds to a direction. Since $\mathbf{K}$ is aligned along the x-axis in real space, its direction cosines are $(\alpha_K, \beta_K, \gamma_K) = (1, 0, 0)$, placing it on the α axis (shown as a blue dot) in the configuration space.

For normal incidence, both α_i and β_i are zero, which places the incident wave vec-

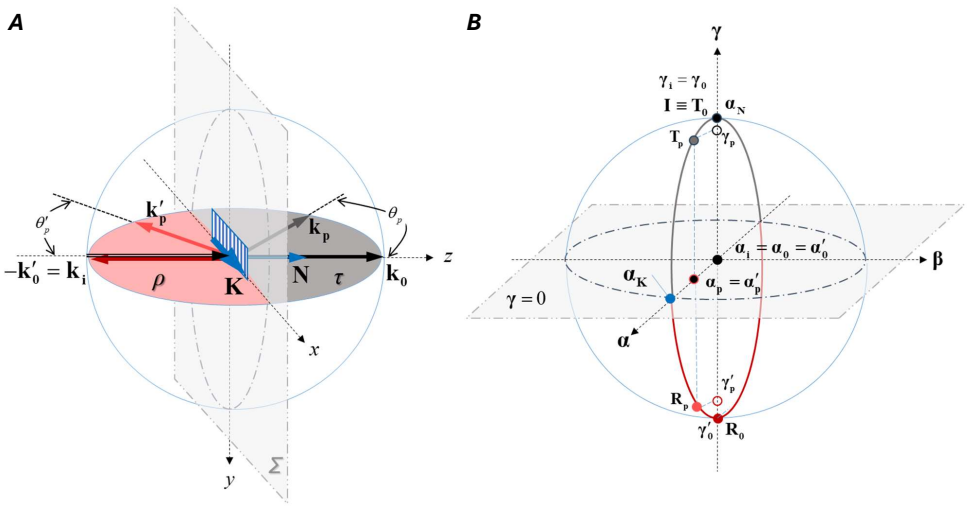

Figure 1.4: Diffraction effects at normal incidence represented in: A) real space with Cartesian coordinates xyz, B) configuration space with direction cosines $\alpha\beta\gamma$. Only one of the possible DO wave vectors is shown for reflection or transmission.

tor (**I**) on the γ axis. The diffracted orders all have $\beta_p = 0$ (according to Equation 1.2), while α_p and γ_p range from -1 to 1, positioning them along the circular longitudinal arc that intersects the angular-space sphere at $\beta = 0$. In transmission, only one hemisphere of the configuration space is required to completely describe the distribution of DO, as the transmitted $0^{th}-$order ($\mathbf{T_0}$) is in the same direction with the incidence wave-vector (**I**), and all propagating higher DO will have positive values for γ_p. Conversely, in reflection, the 0^{th} order is oriented opposite to the incident light, thus appearing in the lower hemisphere along with the higher orders having negative γ_p values. The projections of both reflected and transmitted higher orders overlap in the projection plane $\alpha\beta$, where they are arranged in a straight line, evenly spaced with the 0^{th} order at the center.

1.4.2 Case II: Principal plane of incidence

As the incident angle, θ_i, increases along the xz-plane in real space, as illustrated in Figure 1.5A, the 0^{th} order displaces counter-clockwise with respect to the $\alpha\gamma$-axes, along the longitudinal arc for transmission and clockwise for reflection in the

configuration space, as illustrated in Figure 1.5B. This angular displacement along the arc occurs because α_i and γ_i are no longer zero and one, respectively. Consequently, the orders in the projection $\alpha\beta$-plane shift towards the positive α axis, though they remain equally spaced and aligned on the α-axis.

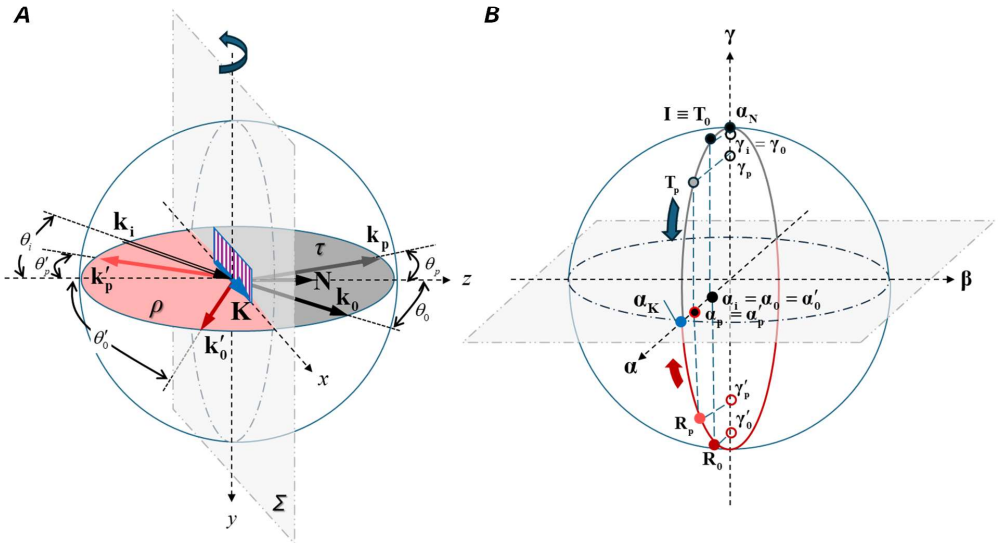

Figure 1.5: Diffraction effects at θ_i incidence within PPI represented in: A) real space with Cartesian coordinates xyz and, B) configuration space with direction cosines $\alpha\beta\gamma$.

1.4.3 Case III: Oblique incidence

For simplicity, we consider the case where the incidence is oblique but confined to the yz plane, as shown in Figure 1.6A. In this case **K**, **N**, and $\mathbf{k_i}$ are not co-planar. For the reflected diffraction orders, $\beta'_p = -\beta_i$ is positive, while for the transmitted diffraction orders, $\beta_p = \beta_i$ is negative. These sign inversions are due to the conventional measurements of θ_i, which is the complement of the projection angle on the y-axis: $\mathbf{k_i} \cdot \mathbf{y} = -k_i sin(\theta_i) = k_i cos(\pi/2 + \theta_i)$. As a result, the longitudinal arc is divided into two semi-arcs and shifts in opposite directions for reflection and transmission, as depicted in Figure 1.6B. The 0^{th} order maintains $\alpha_0 = 0$ due to the incidence being along the yz plane and therefore remains along the β axis in the configuration space.

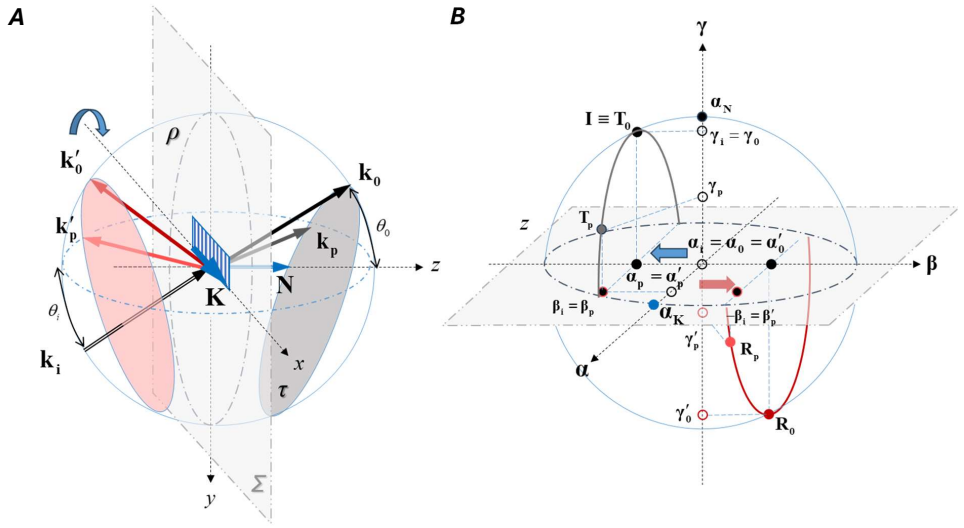

Figure 1.6: Diffraction effects at θ_i incidence, out of PPI along the yz plane, represented in the A) real space with Cartesian coordinates xyz B) configuration space with direction cosines $\alpha\beta\gamma$

1.4.4 Case IV: Rotation along grating normal

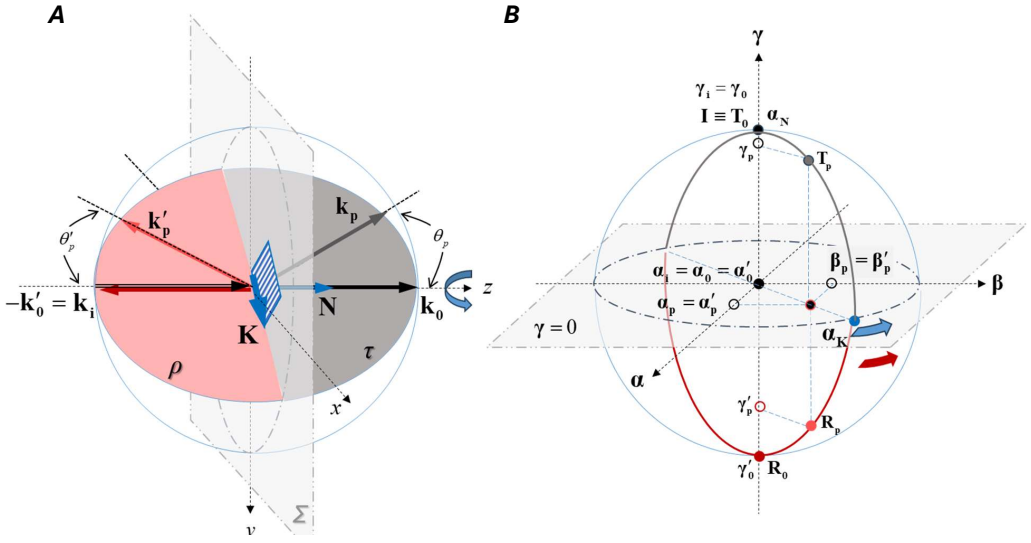

Figure 1.7: Diffraction effects at normal incidence, when grating is rotated at an angle θ_i along the normal, depicted in the A) real space with Cartesian coordinates xyz B) configuration space with direction cosines $\alpha\beta\gamma$

At normal incidence, when the grating rotates along its normal, the PPI rotates along with it as shown in Figure 1.7A. This results in the rotation of the longitudinal arc with the 0^{th} order projection as the pivot in the configuration space as shown in

Figure 1.7B.

REFERENCES

[1] Thomas K Gaylord and MG Moharam. Analysis and applications of optical diffraction by gratings. *Proceedings of the IEEE*, 73(5):894–937, 1985.

[2] G Bianco, MA Ferrara, Fabio Borbone, Antonio Roviello, V Pagliarulo, S Grilli, P Ferraro, V Striano, and G Coppola. Volume holographic gratings: fabrication and characterization. In *Holography: Advances and Modern Trends IV*, volume 9508, pages 43–49. SPIE, 2015.

[3] HJ Jiang, X-C Yuan, Y Zhou, YC Chan, and YL Lam. Single-step fabrication of diffraction gratings on hybrid sol–gel glass using holographic interference lithography. *Optics communications*, 185(1-3):19–24, 2000.

[4] David A Content, Rene A Boucarut, Charles W Bowers, Timothy J Madison, Geraldine A Wright, Don J Lindler, LK Huang, Bernard Peter Puc, Clive Standley, and Todd A Norton. Development and testing of diffraction gratings for the space telescope imaging spectrograph. In *Space Telescopes and Instruments IV*, volume 2807, pages 267–278. SPIE, 1996.

[5] RC Enger and SK Case. High-frequency holographic transmission gratings in photoresist. *JOSA*, 73(9):1113–1118, 1983.

[6] Eric B Burgh, Matthew A Bershady, Kyle B Westfall, and Kenneth H Nordsieck. Recombination ghosts in littrow configuration: Implications for spectrographs using volume phase holographic gratings. *Publications of the Astronomical Society of the Pacific*, 119(859):1069, 2007.

[7] He Lin, Mingzhao Ouyang, Bingxu Chen, Qifan Zhu, Jinshuang Wu, Nan Lou, Litong Dong, Zuobin Wang, and Yuegang Fu. Design and fabrication of moth-eye subwavelength structure with a waist on silicon for broadband and wide-angle anti-reflection property. *Coatings*, 8(10):360, 2018.

[8] Ulrike Schulz, Friedrich Rickelt, Henning Ludwig, Peter Munzert, and Norbert Kaiser. Gradient index antireflection coatings on glass containing plasma-etched organic layers. *Optical Materials Express*, 5(6):1259–1265, 2015.

[9] Abigail Peltier, Gopal Sapkota, Jason R Case, and Menelaos K Poutous. Polarization insensitive performance of randomly structured antireflecting planar surfaces. *Optical Engineering*, 57(3):037109–037109, 2018.

[10] David A Gonzalez and Menelaos K Poutous. Bidirectional scattering distribution function of random antireflective nano-roughened surfaces. In *Optical Components and Materials XVIII*, volume 11682, pages 167–173. SPIE, 2021.

[11] David A. Gonzalez, Jesus Meza-Galvan, David Sharp, Karun Vijayraghavan, and Menelaos K. Poutous. Optical scattering measurements of random anti-reflective nanostructured surfaces in the mid- and long-wave IR. In Ali Adibi, Shawn-Yu Lin, and Axel Scherer, editors, *Photonic and Phononic Properties of Engineered Nanostructures X*, volume 11289, page 112891Q. International Society for Optics and Photonics, SPIE, 2020.

[12] Gottlieb S Oehrlein. Surface processes in low pressure plasmas. *Surface Science*, 386(1-3):222–230, 1997.

[13] James E Harvey and Cynthia L Vernold. Description of diffraction grating behavior in direction cosine space. *Applied optics*, 37(34):8158–8159, 1998.

[14] James E Harvey. Fourier treatment of near-field scalar diffraction theory. *Am. J. Phys*, 47(11):974–980, 1979.

[15] James E. Harvey and Richard N. Pfisterer. Understanding diffraction grating behavior: including conical diffraction and Rayleigh anomalies from transmission gratings. *Optical Engineering*, 58(8):087105, 2019.

[16] Elias N. Glytsis and Thomas K. Gaylord. Three-dimensional (vector) rigorous coupled-wave analysis of anisotropic grating diffraction. *J. Opt. Soc. Am. A*, 7(8):1399–1420, Aug 1990.

CHAPTER 2: ANTI-REFLECTIVE MODIFICATION OF FREEFORM ELEMENTS AND CYLINDRICAL LENSES

2.1 Introduction

[1]Although challenging in design and fabrication, broadband anti-reflection (BBAR) coatings are of significant importance considering photon flux performance improvements in optical instruments like telescopes, or devices such as power sensors, solar cells, and imaging detectors. Conventional anti-reflection optical surface treatments include single-film quarter-wave coatings for limited-band reflectivity suppression (SLAR), and multi-layered thin film coatings (MLAR) for wider bands[1, 2]. For SLAR the major challenge is the availability of materials that match the optical interface impedance for the substrate of choice. Thin films with gradient index profiles can facilitate impedance matching easier and enable effective anti-reflectivity over wider angles of incidence and broader wavelength bands[3–5]. Balanced compromise solutions, between fabrication complexity and desirable performance, are often implemented. Vapor deposition, electrostatic layer to layer deposition, and sputtering are some of the conventional thin film fabrication techniques used [6–8]. The inevitability that materials with thermal and mechanical mismatched properties are deposited on the substrate can be of concern for some instruments or applications, especially if the optics are to function in environments with variable ambient conditions.

In recent years, random anti-reflective subwavelength surface structures (rARSS) have been introduced as substitute for traditional thin film anti reflection (TFAR)

[1]Reprinted with permission from U. Subash, H. Lee, and M. Poutous, "High-efficiency anti-reflective modification of freeform elements and cylindrical lenses for arrayed wide-field astronomical corrector units," *Journal of Astronomical Telescopes, Instruments, and Systems* **10**, 025007 (2024). © SPIE.

coatings. These structures have demonstrated excellent performance as anti-reflective surfaces across various spectral ranges, including the visible, short-wave (SWIR) and mid-wave (MWIR) infrared regions [9–12]. Furthermore, their monolithic fabrication into the substrate surface, primarily through reactive ion plasma etching processes, endows them with higher thermal stability and mechanical durability [13]. Unlike conventional thin film coatings, rARSS do not necessitate complex design efforts, since their random nature makes the optimization of fabrication parameters the primary design objective. While the majority of research on rARSS has focused on planar substrates and interfaces, achieving transmission rates exceeding 99% on fused silica (FS) substrates [14], there have also been a few documented studies on the optical performance of rARSS on non-planar surfaces, such as lenses [15–18].

In Astronomy, these aspects render the rARSS as an attractive broadband alternative to thin film AR coatings for imaging and spectroscopic systems with multiple air-glass interfaces. One example is the Arrayed Wide-Angle Camera System (AWACS) [19, 20]. Unlike the traditional wide-field corrector design based on multiple large lenses or mirrors, the AWACS accomplishes desired field expansion via a suite of small cost-effective electro-opto-mechanical units over a telescope's focal surface, for local and simultaneous telescope field aberration and atmospheric dispersion compensation (ADC). All units share one common electro-opto-mechanical design, featuring imaging lenses for the underlying optical relay, a combination of an adaptive cylinder lens pair and simple free-form lens for field aberration correction, and a miniature prism pair as an ADC element. The design commonality in AWACS allows leverage of significant cost and complexity scaling while transitioning from a 2∼3 m class telescope to 30m-class Extra Large Telescopes and beyond. Due to the large (22×) number of air-glass interfaces in each AWACS unit, it is critical to minimize the loss from Fresnel reflection and scattering over a broad wavelength range from 365 nm to 1000 nm. The rARSS exhibits characteristics that are ideal to meet such

a need[21–23].

Research to-date has primarily focused on assessing the optical transmission performance of random structures including some comparisons between lenses with TFAR and rARSS [15, 16, 18], without investigating optical system-level effects. Potential scattering or wavefront distortions caused by the presence of rARSS-enhanced components in an optical system are not available in the existing literature. The topography of non-planar surfaces may lead to significant alterations of the rARSS average density and local profiles, since their fabrication consists of a top-down high-power reactive etching process. This chapter examines the impact of rARSS on the performance of the freeform elements and cylindrical lenses as used in the AWACS system, as individual elements and at the system level, specifically evaluating their spectral transmission, scattering effects, and wavefront distortion. We conducted measurements of the cylindrical wavefronts emerging through the lenses and the bidirectional scatter distribution function of the freeform element, both before and after applying rARSS. The enhanced elements were placed in an arrayed wide-field astronomical camera system unit assembly, and comparative field tests were performed with the Harlan J. Smith telescope (HJST) at the McDonald Observatory.

2.2 Fabrication

There are two steps in rARSS fabrication on optical surfaces: the deposition of a porous masking layer and, etching the unmasked nanopores into columnar nanostructures directly into the substrate as explained in section 1.2.1. The sputtering process control parameters (time, magnetron power) were optimized based on prior process development steps [24]. We employed an anisotropic reactive-ion plasma etch step (PlasmaTherm RIE7000) to permanently transfer the nanopore random profile into the light entry and exit surfaces of the cylindrical lenses and freeform components. In our process, the 600-W RF-driven reactive plasma contains sulfur-hexafluoride (SF_6). The etching parameters were optimized to achieve the required broadband transmis-

sion enhancement in the visible spectral region between 340-800 nm, with the Fresnel transmission at 633 nm enhanced to 99.5 % per surface, based on planar fused silica witness sample measurements.

Three different optical component sets were used: a plano-concave cylindrical lens set (PCV), a plano-convex cylindrical lens set (PCX), and an optical freeform-surface set (FF). All components were made with Corning Fused Silica 7980. The cylindrical lenses are 11 mm in diameter, with a radius of curvature of 400 mm on the curved side, yielding an effective focal length of +88.8 cm and -88.8 cm for the PCX and PCV sets respectively at 633 nm wavelength. The freeform component has an aperture diameter of 36 mm, and a wavefront surface described by:

$$Sag\,(x,y) = -3.47\,Z_3(x,y;R) - 6.73\,Z_7(x,y;R) \tag{2.1}$$

where x, y are surface coordinates, and R is the normalization radius parameter, and the Zernike polynomials are:

$$Z_3(x,y;R) = 2(\frac{y}{R}) \tag{2.2}$$

$$Z_7(x,y;R) = 2.83\,[3\,(\frac{x}{R})^2 + 3\,(\frac{y}{R})^2 - 2](\frac{y}{R}) \tag{2.3}$$

The freeform total maximum sag across the clear aperture is 52 nm. The AR random structures were fabricated on both surfaces of all three sample sets. A total of six samples of each component set were made available for the study.

2.3 Test methods

A grating spectrophotometer (Cary 60) was used to measure the directional optic axis transmission of all samples, before and after the rARSS etching process. The spectrophotometer uses an unpolarized broad-band lightsource (300 nm - 1900 nm) with a 1 mm beam spot diameter. The on-axis spectral transmission ratio, normalized to the incident intensity, was measured for each component from the three sets and

then averaged within the set.

In order to examine potential wavefront distortion caused by the rARSS etching process, the wavefront of the samples was measured using the Shack-Hartmann (SH) wavefront sensor (ThorLabs WFS150-5C) before and after the process. The sensor is able to perform wavefront measurements within the 300 to 1100 nm peak-to-valley sag (PV) range. The prominent factors that affect the cylindrical lens profiles are the Zernike polynomials for astigmatism (Z_6) and defocus (Z_5), and the PV amplitude of the of the emerging cylindrical wavefront. The nomenclature of the Zernikes with just one parameter (Z_r) follows Malacara [25]. Additional Zernike polynomial terms[26], such as tip and tilt, are reduced with alignment of the pieces under test. The sample was affixed to an axial rotational holder, positioned normal to the optic axis, allowing for adjustment of the azimuth angle. This arrangement ensured consistent alignment of all six samples of both types of cylindrical lenses. The SH source is a 50 mW, 650 nm wavelength diode laser, with a beam diameter of 4 mm. The baseline wavefront from the source is collimated and flattened by minimizing PV to 0.4 μm prior to individual sample measurements. The SH sensor exposure time was 0.27 s per capture, and 20 wavefronts were averaged per measurement. The pupil definition for the sensor was set to 5 mm in diameter to ensure full imaging of the beam. To account for possible light source fluctuations, data was collected for each sample before and after the rARSS process for a period of 3-5 days, and averaged over the number of days for consistency. The freeform lens had a PV amplitude less than 0.4 μm range within the center field, and hence the profile was not discernible from a flat wavefront. We limited the wavefront measurements to the PCX and PCV cylindrical lenses.

To measure the redistribution of radiance on-axis and any possible induced off-axis scatter due to the presence of the rARSS structures, we measured the bi-directional transmission distribution function (BTDF) of a selected freeform sample. A complete equatorial-angle scatterometer instrument was used (CASI, Schmitt Industries Inc.).

The instrument has a Helium-Neon laser source operating at 633 nm wavelength, with a half-wave retarding plate and a linear polarizer, to select the test polarization state. The instrument is capable of measuring scatter over the full 180° angular transmission range, as shown in Figure 2.1. The sample under test was mounted on the linear translation stage perpendicular to the incident beam. The instrument signature (no sample baseline) and the sample BTDF is measured using a Si-detector, with a separate linear polarizer (analyzer), that sweeps the path of the equatorial circle. The detector has auto-selecting multiple aperture diameters, performing a true radiometric detector measurement of irradiance, which allows for a relative sensitivity range of 9-orders of magnitude. The freeform sample was mounted with the curved side facing the source, the sample stage was adjusted to allow for normal incidence, and the linear translator was used to select five test locations within the component. The test areas are labelled according to the inset orientation in Figure 2.1.

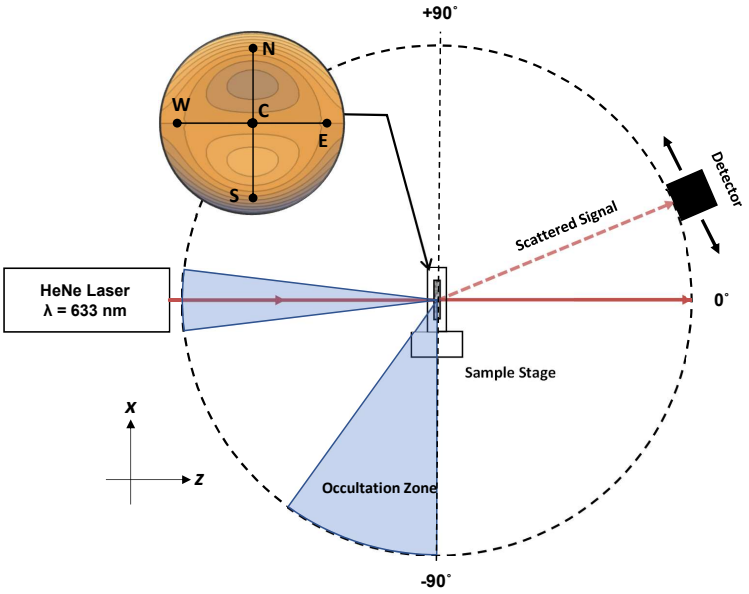

Figure 2.1: Top-down view of the CASI scatterometer layout used to measure the scatter of the freeform element before and after etch. The BTDF is measured sweeping the detector along the circular path from -90° to +90°. The inset shows the test locations on the freeform component surface facing the light source. The coordinate reference applies to the scatterometer.

2.4 Results

2.4.1 Component Transmission Enhancement

Figure 2.2 shows the measured normalized spectral axial transmission of the sample sets before and after rARSS processing for the PCV, PCX, and FF. The pre-process measurements were averaged over all six samples within each set of components. The maximum-minimum transmission range of measurements is shown as vertical bars. The resolution of the spectrometer was set to 1 nm. Following the double-sided rARSS etching process, the best four out of six measured samples were chosen from each set to be used in the corrector unit system. Table 2.1 lists the wavelength ranges where the transmission exceeds 98% for each set. The spectral transmission of the unprocessed samples averages to 93%, corresponding to an average 3.5% Fresnel reflectance per surface at normal incidence. The post-process transmission peaks at 99.1% for all sample types, indicating that the rARSS suppresses Fresnel reflectivity to a maximum of 0.5% per surface. The overall average transmission enhancement for the processed lens sets is 6% across the band of interest. The rARSS transmission curve is devoid of interference swings, compared to conventional thin film BBAR coatings. The bandwidth ($\Delta\lambda$) above 98% transmission is >400 nm for PCX and PCV lenses, and >500 nm for the FF. The peak-efficiency band is 40-50 nm for the lenses and >100 nm for the FF.

Table 2.1: Spectral normalized-transmission ranges, and peak transmission values with ranges, for the lens and FF sets from the measured test data shown in Figure 2.2.

Sample	$\Delta\lambda$ for $T > 0.98$	T_{max}	$\Delta\lambda_{T_{max}}$
PCV	333 nm - 746 nm	0.991	438 nm - 484 nm
PCX	334 nm - 770 nm	0.992	466 nm - 503 nm
FF	347 nm - 851 nm	0.993	478 nm - 601 nm

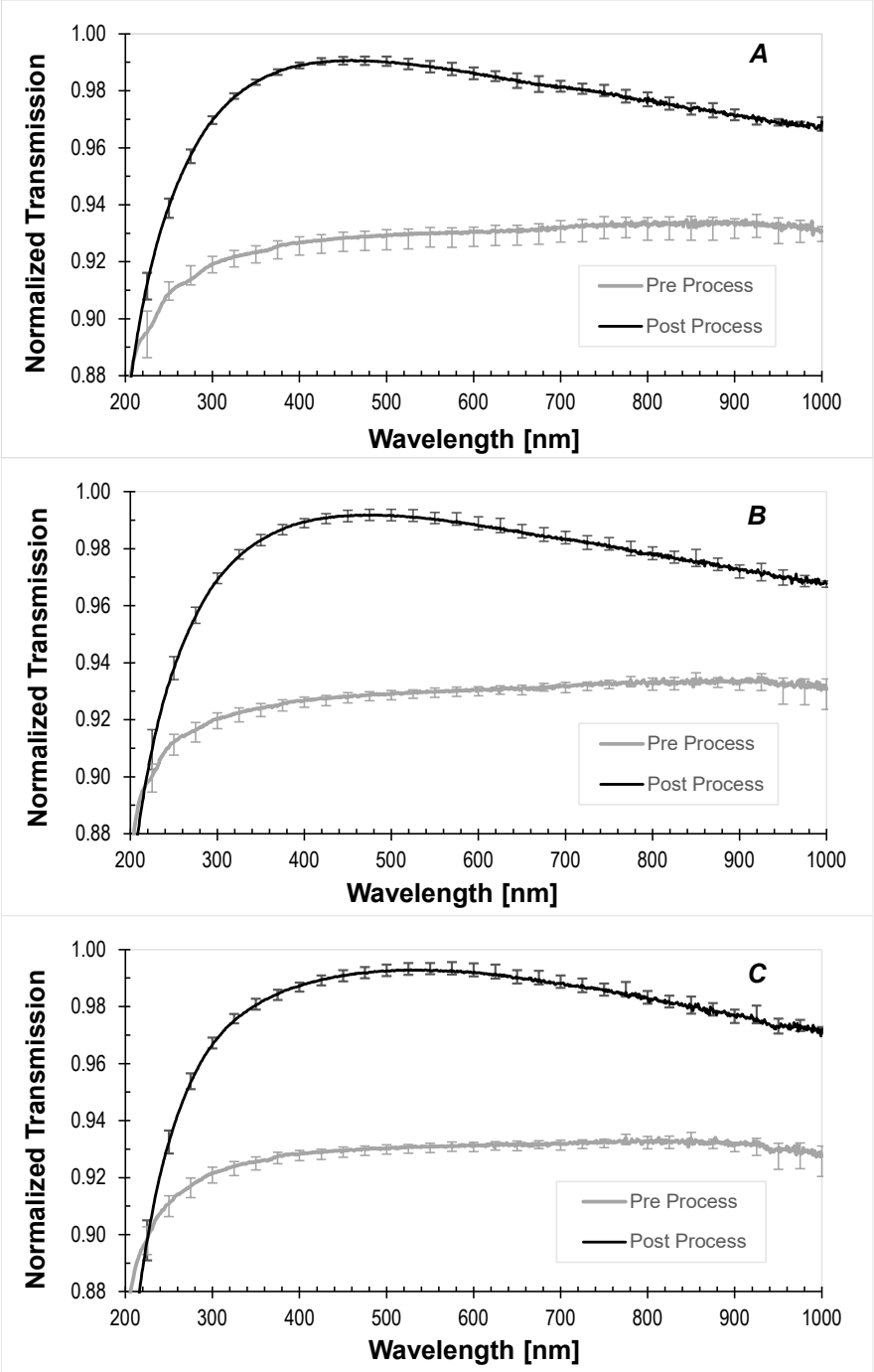

Figure 2.2: Normal incidence axial transmission measurements, averaged across samples, for: (A) PCV lenses, (B) PCX lenses and, (C) the FF elements with 1 nm wavelength resolution. The pre-processed measurements are shown in gray and the rARSS double-sided enhanced measurements are in black. The bars indicate the within-set maximum to minimum range measurements for each wavelength, and are shown in 25 nm wavelength intervals.

2.4.2 Component Wavefront Measurements

As with any surface modification subtractive process such as RIE, there is concern that component sag or functionality could be altered. Since the cylindrical lenses and FF were etched to embed the rARSS on their surfaces, we considered wavefront tests for the PCX and PCV elements before and after processing. The lens-induced wavefront curvature depends on the component surface sag, and to distinguish between manufacturing and processing variations within the groups of lenses tested, we measured the cylindrical converging or diverging wavefront generated by each lens within a set.

The prominent factors that represent the cylindrical profile of the lenses are the wavefront PV-amplitude, Zernike coefficients Z_5 (defocus) and Z_6 (astigmatism). Table 2.2 shows global measurement averages, calculated with the measured values from each lens over time and for each lens set. Figure 2.3 shows the fractional deviation (δ) of the time-averaged measurements from the global average values listed in Table 2.2, and the design specifications where available. The fractional deviation is calculated using:

$$\delta(x) = \frac{[< x >_t]_{pre/post}}{[< x >_{t,s}]_{pre}} - 1 \tag{2.4}$$

$< x >_t$ stands for either wavefront PV, Z_5, or Z_6 values, averaged across time measurements with index t =1,2,..5; and $< x >_{t,s}$ is the global average, i.e. time-averaged measurements averaged across the number of samples per set (s =1,2,..6).

Note that the $\delta(x)$ was calculated always using the global average pre-process to obtain the deviation post-process. The average wavefront PV fractional deviation before and after the rARSS process is within the specification range of -0.03 $< \delta(pv) <$ +0.03 , equivalent to an absolute wavefront $\lambda/10$ at 633 nm. The maximum range of

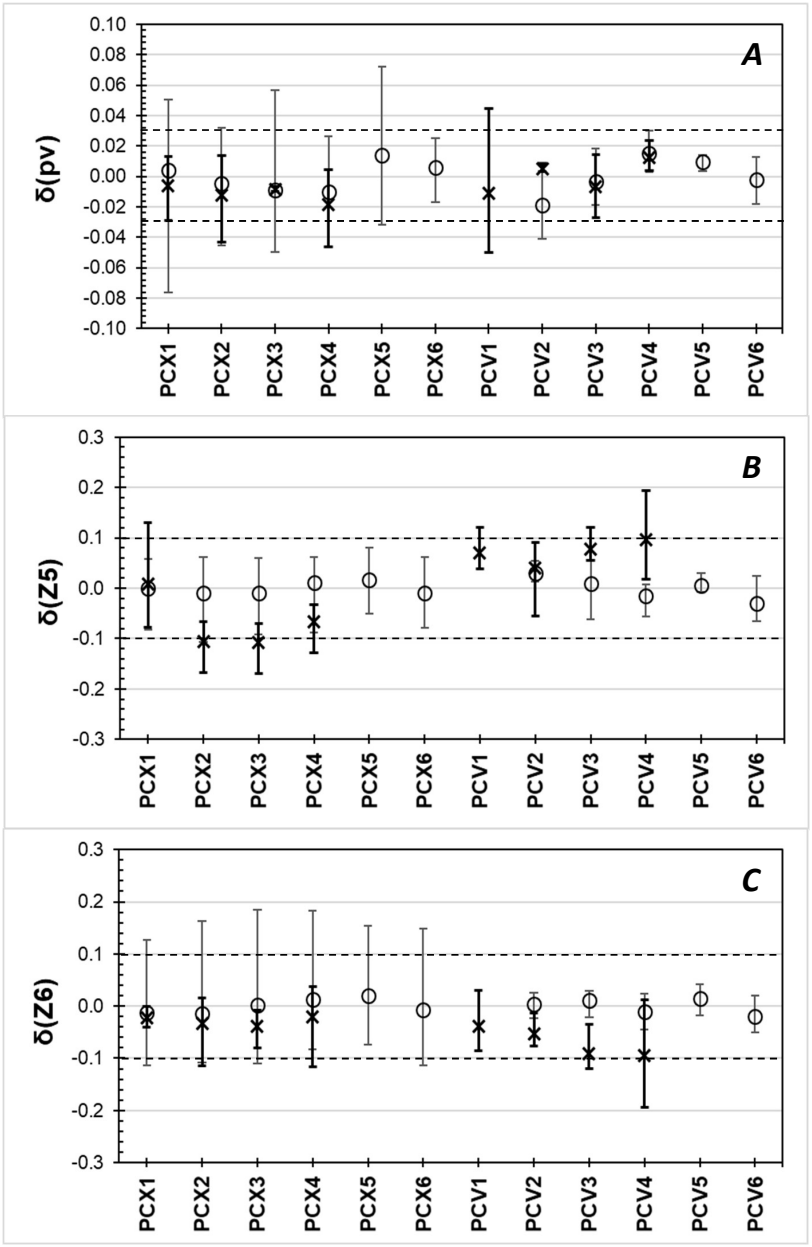

Figure 2.3: Comparative wavefront measurements for all PCX and PCV cylindrical lenses, before (circles) and after (bold font crosses) rARSS enhancement. Fractional deviation of: (A) Wavefront PV amplitude of the cylindrical profile, $\delta(pv)$; (B) Defocus Zernike coefficient $\delta(Z5)$ and; (C) Astigmatism Zernike coefficient $\delta(Z6)$. The bars indicate the maximum deviation range of measurements across time (days). Thin bars belong to the pre processing evaluation and thick bars to post processing tests. The horizontal dashes indicate component specification limits.

wavefront PV fractional deviations within-sample measurements is caused by temporal environmental and alignment fluctuations in the testing conditions. The fractional deviations for Z_5 and Z_6 are within absolute wavefront deviations of $\lambda/8$ and $\lambda/10$ respectively .

Table 2.2: Across-sample measured global averages for PV, Z_5, and Z_6, pre- and post-rARSS processing, over all days of measurement. Values shown are in μm.

Sample	$< pv >_t$		$< Z5 >_t$		$< Z6 >_t$	
	Pre-Proc	Post-Proc	Pre-Proc	Post-Proc	Pre-Proc	Post-Proc
PCV	1.595	1.614	-0.379	-0.406	-0.631	-0.588
PCX	1.544	1.527	0.391	0.365	0.487	0.474

Figure 2.4 shows the 2-dimensional wavefront map with pixels along the x and y axes, for four tested cylindrical lenses. The 4 mm diameter beam spot spans approximately 20 x 20 pixels of the SH sensor. On the left column of the figure, the wavefront maps of the cylindrical components are displayed post-processing with rARSS, where the colorbars represent the wavefront concavity or convexity in micrometers. It is evident that the cylindrical profile is maintained for all four components after process with the first two being convex and the bottom two being concave. The maximum wavefront sag of all four components is nearly 1.6 μm, indicated by the yellow on the colorbar, corresponding to the previously mentioned wavefront PV amplitude, which is tabulated in Table 2.2. On the right column of Figure 2.4, the residual wavefront is shown, calculated by subtracting the pre-processed wavefront map from the post-processed one pixel by pixel. The wavefront PV amplitude of these residuals is approximately 0.4 μm, within the baseline uncertainty (no sample) wavefront of the sensor, further suggesting minimal distortion in the wavefront. While only wavefront maps for four components are presented, all 12 components exhibited similar performances, and the maximum/minimum ranges are incorporated in the data of the wavefront PV amplitude graphs (Figure 2.3.)

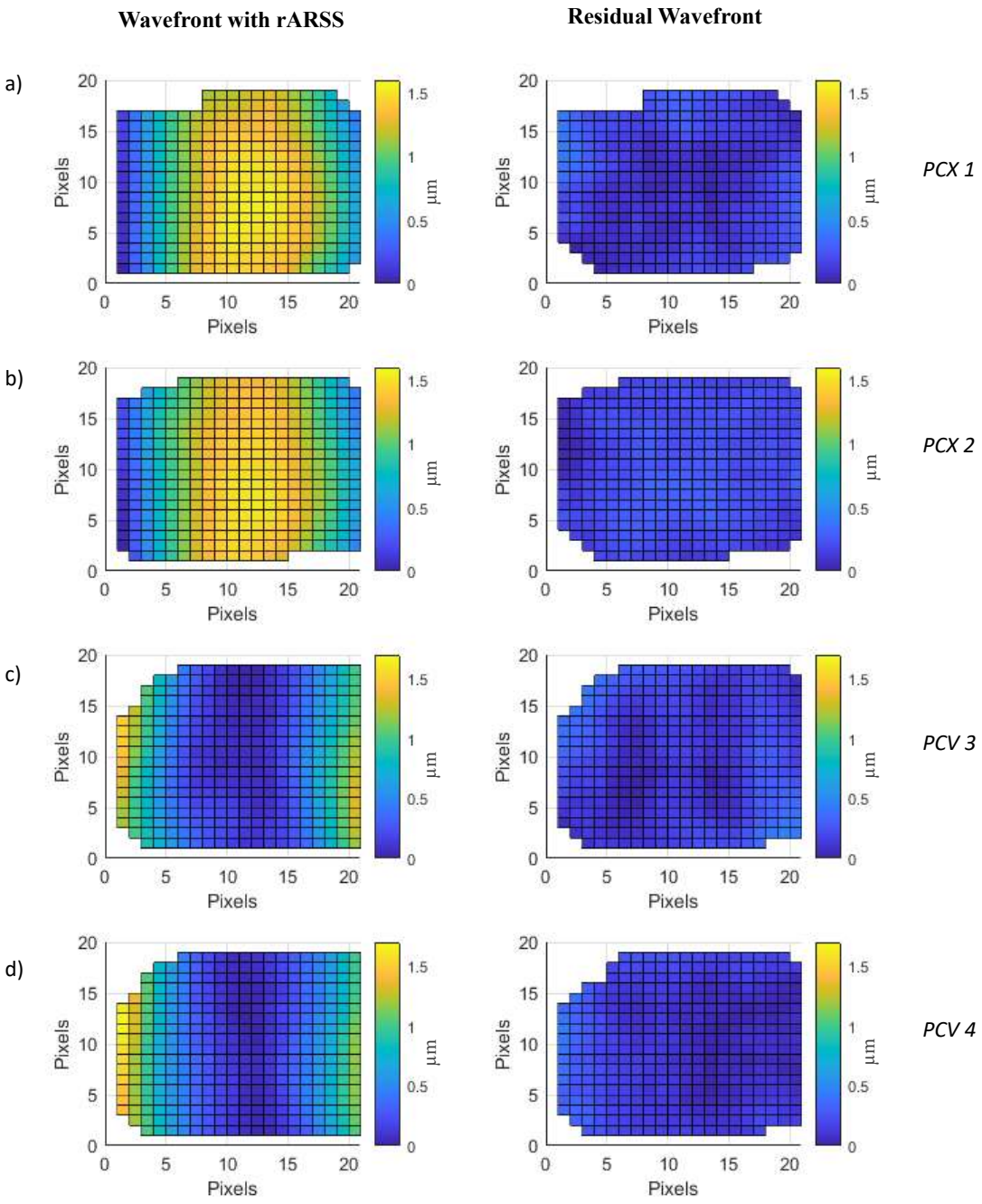

Figure 2.4: Pixel to pixel wavefront measurements of PCXs and PCVs post process with rARSS shown on the left column, and the residual wavefront (pixel to pixel difference in wavefront of pre- and post-processed cylindrical components) shown on the right for four different lenses: a) PCX1, b) PCX2, c) PCV3 and d) PCV4. The colorbar on each figure represents the convexity or concavity of the wavefront in μm from the base at 0 μm. The residual wavefront is within the baseline uncertainty (no sample) wavefront of the SH detector (0.4μm sag.)

2.4.3 Component Surface Scatter

The bidirectional transmission distribution function was measured following the procedure in section 2. Any scattering effects prior-to and post-etching, are detectable within 9-orders of magnitude in radiance across the equatorial optical xz-plane. Figure 2.5 shows the FF logarithmic-scaled BTDF, measured at the five cardinal locations of the component shown in Figure 2.1, as a function of angle of collection of the detector (θ_s) and the associated variable β_s. The collection-coordinate transformation: $\beta_s = \sin\theta_s$, plotted in a logarithmic scale, expands the axial beam profile measurements in order to separate finite-aperture diffraction effects from the axial radiance emerging from the tested component surfaces.The testing system signature beam profile, including the spatial-filtering aperture diffraction is contained within $-3^\circ < \theta_s < +3^\circ$, shown in Figure 2.5(B) as the vertical dotted line. Beyond this region the BTDF measured values are well below six-orders of magnitude with respect to the peak value on-axis. The shoulder asymmetry of the N/E and S/W locations is due to alignment and absolute polar orientation of the FF with respect to the detector orbit. These results indicate that the rARSS doesn't add excessive transmission scatter to the FF component.

Due to the low overall reflectivity (0.5%) and non-plannarity of the FF component tested, we were not able to measure the bidirectional reflection distribution function (BRDF). To provide a quantitative comparison with the BTDF results shown in Figure 2.5, we measured the BRDF of two optical-quality-flat fused silica windows with and without rARSS. Nano-structuring for both surfaces of the flat test-samples was achieved with the same RIE recipe used to modify the FF and cylindrical lenses in this study. Figure 2.6 shows the BRDF with respect to the reflection angle-of-collection (AOR) associated variable β_c. The flats were tested at an angle-of-incidence (AOI) of -15° from the surface normal, and the specular reflected beam was located at $+15^\circ$, corresponding to $\sin\beta_c = 0.26$. The BRDF wide-angle measurements are comparable

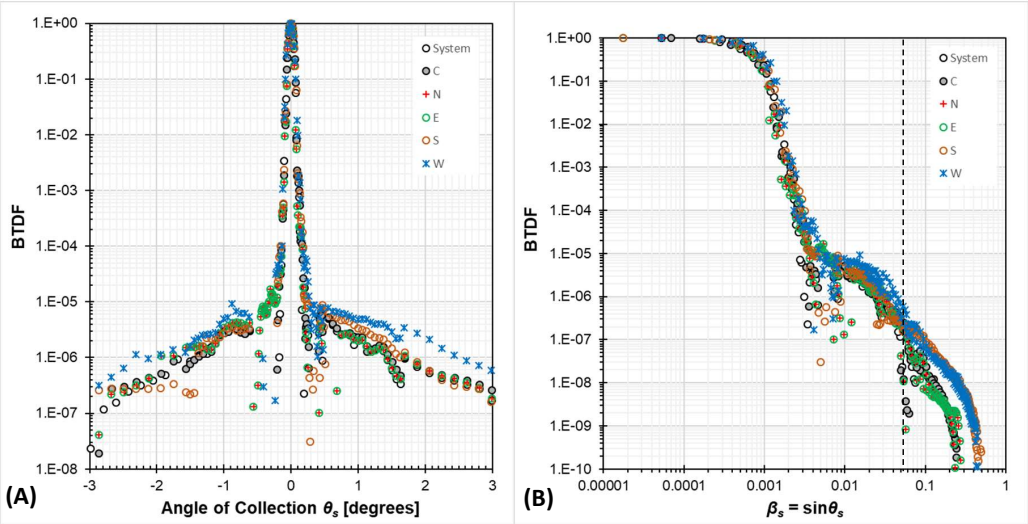

Figure 2.5: BTDF measurements from the freeform element locations tested as shown in the inset of Figure 1, compared with the instrument's signature. The BTDF scale is logarithmic. (A) BTDF measurements displayed as a function of the angle of collection (θ_s). (B) BTDF measurements displayed as a logarithmic function of the angular parameter β_s to accentuate comparisons in the axial direction. The vertical dotted line indicates the angular extent of the instrument's test beam.

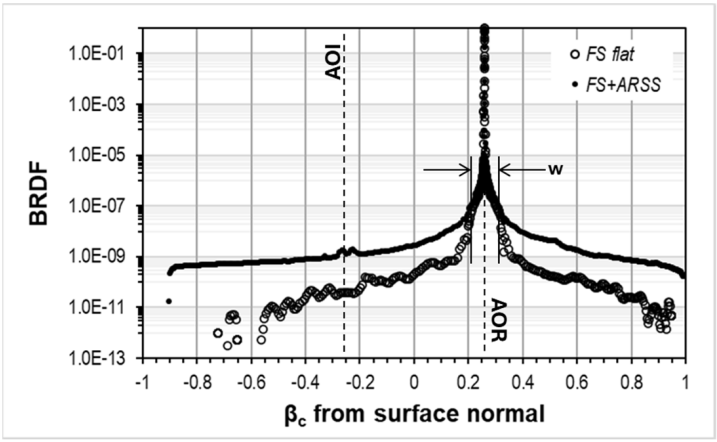

Figure 2.6: BRDF measurements from a fused silica flat (FS flat), compared with a fused silica flat with added ARSS on both surfaces (FS+ARSS). The BRDF measurements were taken at $-15°$ angle-of-incidence (AOI) and are displayed as a logarithmic function of the angular parameter β_c with respect to the surface normal.The incident beam has a full angular width of 6°(w).

with the corresponding BTDF values, indicating that there is bi-directional scatter due to the presence of the rARSS. We note that the reflective near-axis scatter due

to the presence of the nanostructures on the flat surface is on the order of 10^{-8}, an average of an order of magnitude lower than the BTDF. The BRDF of the rARSS-flat is higher than the polished silica flat surface for reflection collection angles wider than AOR$\pm 3^{\circ}$, symmetrically about the specular reflection.

2.5 System-level performance evaluation of the rARSS

The Arrayed wide angle camera system (AWACS) is made of segmented relay units as shown in Figure 2.7. Each unit comprised of a free-form lens, a pair of cylindrical lenses, three relay doublet pairs, and an ADC prism pair. The system-level performance of freeform and cylindrical components was evaluated at McDonald Observatory using two AWACS units to assess throughput consistency. The first unit had all the components treated with conventional MLAR-BBAR coatings, while second unit had the cylindrical lenses that were rARSS-modified along with the conventional AR treated components. Total throughput of the unit were measured using a scanning spectrometer, excluding the freeform lens due to space constraints. The spectral transmission results are shown in Figure 2.8. Compared to model predictions, both units had nearly identical transmission but were less efficient than expected, particularly in the blue spectrum between 370nm and 450nm.

Figure 2.8A illustrates a comparison of the spectral transmission of each unit against model predictions. The measured spectras of both units are shown in brown and yellow curves that has identical transmissions indicating consistency across units. The model prediction, shown in blue, was based on transmission analysis of the AWACS unit design within the Zemax Optics Studio, incorporating published bulk transmission data from Ohara and Schott for all glass materials used, vendor-supplied MLAR-BBAR measurements, and rARSS witness data. Despite careful specification of transmission requirements for optical materials, surface finish, and AR treatments, both units showed significant throughput deficits in the blue part of the spectrum.

To furthur analyze the discrepancy at shorter wavelengths, additional measure-

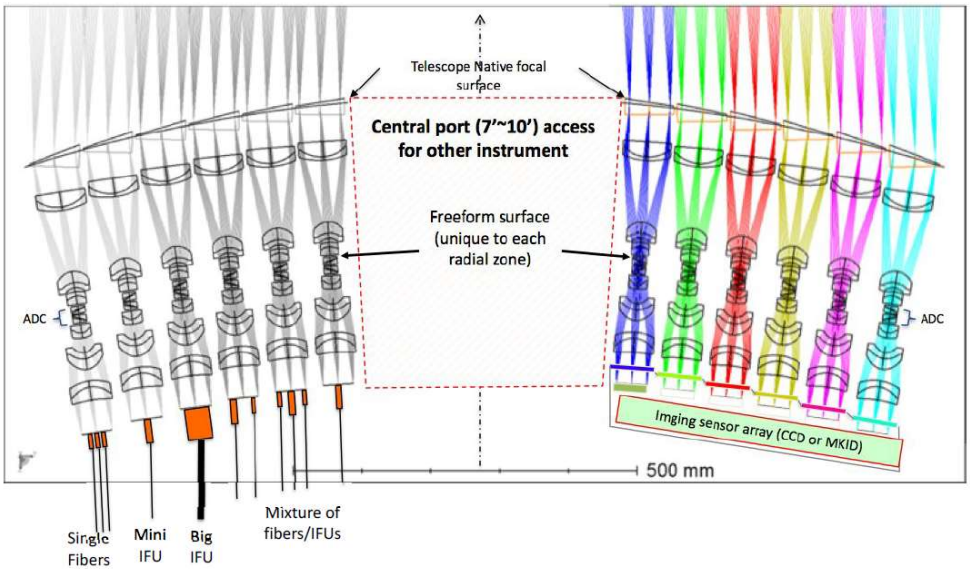

Figure 2.7: Reprinted with permission from [19]. Arrayed wide-angle corrector system made of segmented relay units each of which contains the cylindrical lens pair and freeform component for system level testing.

ments to extract the individual throughput contributions of different optical groups within the AWACS units was done. The mechanics of AWACS unit enables the removal of ADC prism pairs and cylindrical lens pair allowing for measurements with and without these components. This facilitated to individually isolate the contributions of the relay lens system, the ADC prism pair, and the cylindrical lens pair. Figure 2.8B shows the estimated performance of AR treatments applied to these portions. The "Relay per surface (TFAR)" curve was obtained first by calculating T_{relay}, by reducing the bulk transmission of the relay-lens-only unit model from its spectral measurement, leaving contributions primarily from AR treatment. The per-surface transmission was then calculated by taking the N-th root of T_{relay}, with N representing the number of surfaces. Similar procedures were followed to derive the "ADC per surface (TFAR)" and "Cyl per surface (RARSS)" curves.

From the results the MLAR-BBAR coatings incurred about 0.5% more loss per surface than what the vendor-supplied samples suggested, accumulating to a signifi-

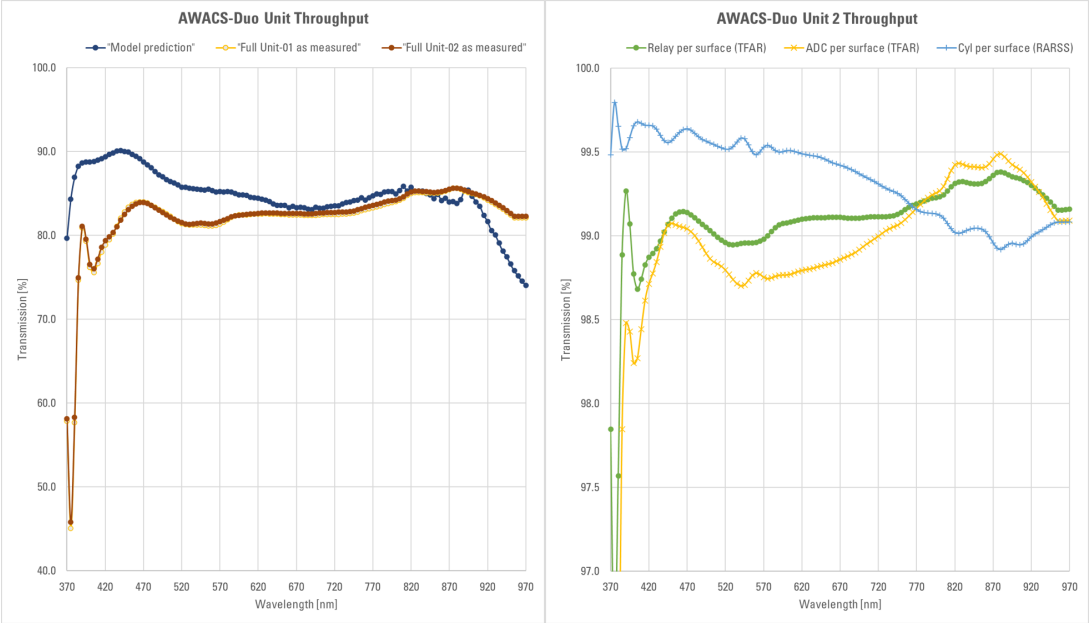

Figure 2.8: (Left) End-to-end spectral transmission measurements of AWACS-Duo units: U1 (yellow line and bullets) and U2 (brown line and bullets), including the model prediction (blue line and bullets). The results for U1 and U2 are overlapping. (Right) Per-surface transmission estimate of different anti-reflective treatments applied to U2 components, based on spectral transmission measurements from component substitutions discussed in the text.

cant throughput loss due to the numerous air-glass interfaces. Conversely, the rARSS treatment largely matched the expected performance, aside from some wavy features in certain wavelength regions, suspected to be artifacts from the reduction procedure. The main takeaway from this analysis is that while the MLAR-BBAR coatings underperformed, the rARSS treatment showed promising performance at the system level and could provide reliable AR capabilities in complex optical systems for astronomy, such as the AWACS units.

2.6 Conclusion

Randomly-distributed anti-reflective nanostructures were fabricated on fused silica cylindrical lenses and freeform optical elements, using a plasma-assisted reactive-ion etching technique. We examined the transmission-enhancing impact of the random nanostructures on the surfaces before their use as components of an arrayed wide-field

astronomical corrector unit.

The total spectral transmission of all component sets tested achieved values over 98%, over a wavelength range of 400-500 nm across the entire visible spectrum, without localized extrema. Component transmission over 99% was measured across a narrower 40-100 nm band, centered around wavelengths of 470 nm for the cylindrical lenses and, 540 nm for the FF. The difference in spectral transmission between the rARSS-enhanced lenses and the FF is attributed to fabrication effects due to the optical component physical dimensions. The FF were three-times larger in aperture diameter and thickness, compared to the lenses. During the rARSS fabrication, the components seat on a platen and are exposed to the RIE plasma driven by a high-power RF-signal. The etch chamber configuration is identical to a large parallel-plate capacitor, with the signal field driven between the platen and the cover plate. The substrate surface etch rate depends on the separation between the exposed surface and the boundary of the plasma. Thicker substrates have smaller separations, resulting in different etch characteristics from thinner substrates. The substrate diameter affects etch uniformity across the surfaces. Larger diameter surfaces result in the generation of more etch by-products that slow the process, and have more center-to-edge uniformity variance. Overall, the results shown in Figure 2.2 are very consistent and meet the spectral transmission requirements of the system unit.

We also found that the cylindrical wavefronts emerging from the lenses were not adversely affected by the rARSS fabrication process, nor the rARSS perturbed the performance of the lenses to a degree of concern. The emerging wavefronts have post-process larger negative values for Z_5 and smaller positive values for Z_6. This observation indicates that the PCX/PCV surfaces are etched somewhat differently from center-to-edge. We measured a Zernike-defocus change from $\lambda/10$ to $\lambda/8$ (at 633 nm), related to the respective convexity or concavity of the lenses, and the Zernike-astigmatism post-process wavefront performance had the same deviation values.

To detect any off-axis light scatter, we measured the bidirectional scatter distribution function of selected locations on the freeform element, after applying rARSS. The testing laser-system-signature spot diameter was not affected at all by the presence of the transmission-enhanced FF, maintaining a $1/e^2$ full-angle divergence of 0.15°, and an unperturbed radiance distribution over 5-orders of magnitude within the entire axially projected full-angle of 10°. This is an indication of absence of scatter to an radiance level equivalent to $1/e^{11}$.

The enhanced elements were placed in an arrayed wide-field astronomical camera system unit assembly, and comparative field tests were performed in the laboratory and with the Harlan J. Smith telescope (HJST) at the McDonald Observatory. The end-to-end spectral and imaging tests clearly indicated that two units exhibited nearly identical imaging and throughput characteristics, that the applied rARSS showed a transmission profile consistent with the expectation based on its sample measurements, particularly near the short wavelengths, and that the system demonstrated no visible degradation in its PSFs across the designed field of view. All of these were confirmed by the on-sky measurement at the HJST.

This work was the first report of functional BBAR-FF elements with rARSS, as well as, this is the only report at present that compares the function of rARSS-enhanced components in a complete optical system. This work was published in the Journal of Astronomical Telescopes, Instruments and Systems (JATIS) [27].

REFERENCES

[1] Hiroomi Shimomura, Zekeriyya Gemici, Robert E Cohen, and Michael F Rubner. Layer-by-layer-assembled high-performance broadband antireflection coatings. *ACS applied materials & interfaces*, 2(3):813–820, 2010.

[2] P.M. Kaminski, G. Womack, and J.M. Walls. Broadband anti-reflection coatings for thin film photovoltaics. In *2014 IEEE 40th Photovoltaic Specialist Conference (PVSC)*, pages 2778–2783, 2014.

[3] Kyoung-Ho Kim and Q-Han Park. Perfect anti-reflection from first principles. *Scientific reports*, 3(1):1–5, 2013.

[4] Kong Wei-Jin, Shen Zi-Cai, Wang Shu-Hua, Shao Jian-Da, Fan Zheng-Xiu, and Lu Chao-Jing. Graded index broadband antireflection coating prepared by glancing angle deposition for a high-power laser system. *Chinese Physics B*, 19(4):044210, 2010.

[5] Minfeng Chen, Hung-chun Chang, Allan SP Chang, Shawn-Yu Lin, J-Q Xi, and EF Schubert. Design of optical path for wide-angle gradient-index antireflection coatings. *Applied Optics*, 46(26):6533–6538, 2007.

[6] Charles Martinet, Victor Paillard, Aline Gagnaire, and J Joseph. Deposition of sio2 and tio2 thin films by plasma enhanced chemical vapor deposition for antireflection coating. *Journal of Non-Crystalline Solids*, 216:77–82, 1997.

[7] Hideshi Hattori. Anti-reflection surface with particle coating deposited by electrostatic attraction. *Advanced Materials*, 13(1):51–54, 2001.

[8] Sang-Hun Jeong, Jae-Keun Kim, Bong-Soo Kim, Seok-Ho Shim, and Byung-Teak Lee. Characterization of sio2 and tio2 films prepared using rf magnetron

sputtering and their application to anti-reflection coating. *Vacuum*, 76(4):507–515, 2004.

[9] Denis Vandormael, Serge Habraken, Jerôme Loicq, Cedric Lenaerts, and D Mawet. Anti-reflective sub-wavelength patterning of ir optics. In *Electro-Optical and Infrared Systems: Technology and Applications III*, volume 6395, pages 198–204. SPIE, 2006.

[10] Douglas S Hobbs, Bruce D MacLeod, and Juanita R Riccobono. Update on the development of high performance anti-reflecting surface relief micro-structures. In *Window and Dome Technologies and Materials X*, volume 6545, pages 242–255. SPIE, 2007.

[11] Rajendra Joshi, Greg J Gbur, and Menelaos K Poutous. Fabrication of broad-band anti-reflective surface on fused silica from visible to swir spectral band. In *Novel Optical Materials and Applications*, pages NoW2D–3. Optica Publishing Group, 2019.

[12] Lynda E Busse, Jesse A Frantz, L Brandon Shaw, Ishwar D Aggarwal, and Jasbinder S Sanghera. Review of antireflective surface structures on laser optics and windows. *Applied optics*, 54(31):F303–F310, 2015.

[13] Lynda E Busse, Jesse A Frantz, Menelaos K Poutous, Ishwar D Aggarwal, L Brandon Shaw, and Jas S Sanghera. Harsh environment tests of random antireflective surface structures on optics. In *2017 Conference on Lasers and Electro-Optics (CLEO)*, pages 1–2. IEEE, 2017.

[14] Lynda E Busse, Catalin M Florea, Jesse A Frantz, L Brandon Shaw, Ishwar D Aggarwal, Menelaos K Poutous, Rajendra Joshi, and Jas S Sanghera. Anti-reflective surface structures for spinel ceramics and fused silica windows, lenses and optical fibers. *Optical Materials Express*, 4(12):2504–2515, 2014.

[15] C Taylor, KJ Major, Rajendra Joshi, LE Busse, J Frantz, JS Sanghera, ID Aggarwal, and MK Poutous. Optical performance of random anti-reflection structures on curved surfaces. In *Optical Components and Materials XII*, volume 9359, pages 178–185. SPIE, 2015.

[16] CD Taylor, LE Busse, J Frantz, JS Sanghera, ID Aggarwal, and MK Poutous. Angle-of-incidence performance of random anti-reflection structures on curved surfaces. *Applied optics*, 55(9):2203–2213, 2016.

[17] Kristin Pfeiffer, Ulrike Schulz, Andreas Tünnermann, and Adriana Szeghalmi. Antireflection coatings for strongly curved glass lenses by atomic layer deposition. *Coatings*, 7(8):118, 2017.

[18] Claudia Pacholski, Christoph Morhard, Joachim P Spatz, Dennis Lehr, Marcel Schulze, Ernst-Bernhard Kley, Andreas Tünnermann, Michael Helgert, Michael Sundermann, and Robert Brunner. Antireflective subwavelength structures on microlens arraysâcomparison of various manufacturing techniques. *Applied optics*, 51(1):8–14, 2012.

[19] Hanshin Lee, John M. Good, Brian L. Vattiat, and Gary J. Hill. Arrayed wide-angle camera system for the Extremely Large Telescopes. In Christopher J. Evans, Luc Simard, and Hideki Takami, editors, *Ground-based and Airborne Instrumentation for Astronomy VII*, volume 10702, page 107021Z. International Society for Optics and Photonics, SPIE, 2018.

[20] Hanshin Lee, John M. Good, Brian L. Vattiat, and Menelaos K. Poutous. Arrayed wide-angle camera system for wide field imaging and spectroscopy on ELTs: proof-of-concept on-sky test results on McDonald Observatory 2.7m telescope. In Heather K. Marshall, Jason Spyromilio, and Tomonori Usuda, editors, *Ground-*

based and Airborne Telescopes VIII, volume 11445, page 114453W. International Society for Optics and Photonics, SPIE, 2020.

[21] Hanshin Lee and Menelaos K. Poutous. Arrayed wide-field astronomical camera system for spectroscopic surveys on Extremely Large Telescopes: system architecture, proof-of-concept, and enabling technologies. *Journal of Astronomical Telescopes, Instruments, and Systems*, 7(3):035007, 2021.

[22] Hanshin Lee, Brian L. Vattiat, Uma Subash, and Menelaos K. Poutous. Integration/test of dual unit arrayed wide-angle camera system and its evaluation in the context of extremely large telescopes. In Christopher J. Evans, Julia J. Bryant, and Kentaro Motohara, editors, *Ground-based and Airborne Instrumentation for Astronomy IX*, volume 12184, page 121848E. International Society for Optics and Photonics, SPIE, 2022.

[23] Uma Subash, Hanshin Lee, and Menelaos K. Poutous. UV to IR high-efficiency antireflective surface modification of freeform and cylindrical lenses for space platform optical instrumentation. In Allison A. Barto, Fanny Keller, and H. Philip Stahl, editors, *UV/Optical/IR Space Telescopes and Instruments: Innovative Technologies and Concepts XI*, volume 12676, page 126760H. International Society for Optics and Photonics, SPIE, 2023.

[24] Abigail P Eckart, Gopal Sapkota, Matthew Potter, Lynda E Busse, Jesse A Frantz, L Brandon Shaw, Jasbinder S Sanghera, Ishwar D Aggarwal, and Menelaos K Poutous. Control of spectral transmission enhancement properties of random anti-reflecting surface structures fabricated using gold masking. In *Advanced Fabrication Technologies for Micro/Nano Optics and Photonics X*, volume 10115, pages 41–47. SPIE, 2017.

[25] Daniel Malacara. *Optical shop testing*, volume 59. John Wiley & Sons, 2007.

[26] Vasudevan Lakshminarayanan and Andre Fleck. Zernike polynomials: a guide. *Journal of Modern Optics*, 58(7):545–561, 2011.

[27] Uma Subash, Hanshin Lee, and Menelaos K Poutous. High-efficiency anti-reflective modification of freeform elements and cylindrical lenses for arrayed wide-field astronomical corrector units. *Journal of Astronomical Telescopes, Instruments, and Systems*, 10(2):025007–025007, 2024.

CHAPTER 3: REACTIVE-ION PLASMA-ETCHED GRATING

3.1 High-efficiency first-order grating for Astronomical applications

3.1.1 Introduction

[1] High-efficiency light throughput is a requirement and at the same time a challenge for astronomical spectrographs. Faint astronomical targets make accurate observation tasks difficult, and require high-efficiency optical systems with reflective, transmissive, and diffractive optical components. Diffraction gratings are important optical components for astronomical spectroscopy, since a grating's first diffraction-order (1DO) is employed for spatially dispersed spectral measurements. It is therefore necessary to optimize the first-order diffraction efficiency (η_1) of gratings, to achieve a good signal-to-noise ratio within reasonable time-scales of measurement. To increase the light collection capabilities of telescopes, researchers are designing and assembling Extremely Large Telescope systems (ELT) and concurrently increase the Strehl ratio requirements of optical systems for better imaging quality. The contribution presented here is in the design and fabrication of high-efficiency diffraction gratings for Astronomical ELT systems. The design, fabrication and functional test results of a proof of concept (POC) high-efficiency first-order grating, using a reactive-ion plasma-etch process (RIPLE) are presented in this Chapter.

The fundamental physical characteristic of a dielectric diffraction grating is the spatial modulation of the refractive index [2]. Upon diffraction, an electromagnetic wave incident on the grating will have its electric field amplitude, or phase, or both, modified in a predictable manner, due to this modulation in the refractive index.

[1] This work was Accepted and Presented at SPIE Astronomical Telescopes + Instrumentation conference held at Montreal, Canada on July 2022. Added as Reference [1] in this chapter

Figure 3.1 helps to visualize the diffraction process in transmission where light of wavelength λ, incident at an angle θ_i on a grating with a periodicity Λ diffracts light along a set of angles θ_{rp} following the diffraction equation :

$$n_r \, sin(\theta_{rp}) - n_i \, sin(\theta_i) = p\lambda/\Lambda \qquad p = 0, \pm 1, \pm 2 \tag{3.1}$$

where p represents the diffraction order number, n_r and n_i are the refractive indices of the two mediums. A first-order grating is when the values of θ_i, λ and Λ is such that, only $p = 0, 1$ has a real value for diffraction angle, θ_{r1}. In this case, the energy of the incident light propagates along the first order making it highly efficient. Rest of the higher orders that have imaginary θ_{rp} values do not propagate and are evanescent. The

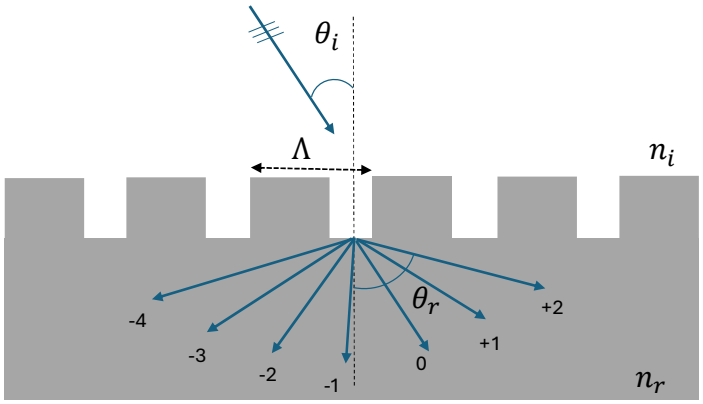

Figure 3.1: Schematic of a diffraction grating in transmission with period Λ.

diffraction equation alone is not sufficient to predict the efficiency of diffraction orders and must be rigorously addressed using Maxwell's equations. To design a highly efficient first-order grating, the rigorous coupled-wave analysis (RCWA) technique was employed [3–5]. RCWA starts with Maxwell's equations that describe the propagation of electromagnetic fields within a medium. It involves expanding the permittivity and electromagnetic fields into Fourier series. By substituting these Fourier expansions into Maxwell's equations and equating the coefficients for each harmonic, a set of

coupled differential equations for the Fourier coefficients is derived, which can be expressed in matrix form. This matrix differential equation is then converted into an eigenvalue problem. The eigenvalues correspond to the propagation constants of the modes, while the eigenvectors represent the mode profiles. It is essential to enforce the continuity of the tangential components of the electric and magnetic fields at the interfaces between different layers of the grating to ensure accurate modeling. The precision of the calculation improves with the number of terms included in the Fourier series. The matrix formulation is implemented computationally and used throughout this work to design the first-order grating.

3.1.2 Design, Fabrication, and Grating Characterization

Designing any grating is specific to the wavelength band of operation (WB) and the light incidence angle (AOI), both parameters specified by the desired application. The grating presented here was designed for the VIRUS2 spectrograph unit for the McDonald Observatory's 2.7 m Harlan J Smith Telescope (HJST) [6]. It has a novel beam splitting module (BSM) [7] that channels the collected light into four different spectral ports ("blue", "green", "red" and "deep red") corresponding to wavebands covering the wavelength range from 370 to 950 nm. Each spectral channel (port) provides light input for a different spectrograph unit that use separate WB gratings, thus gratings are critical components. A proof of concept (POC) RIPLE grating, with a total surface area of 25 mm by 25 mm, was selected for development. The operating band pass of the "red" channel grating spans 470 nm - 700 nm. The period (Λ) of the grating is set at 566 nm for a nominal angle of incidence (AOI) of 36.4° from air. The depth and fillfactor of the grating were optimized using numerical RCWA simulations of grating models, to maximize the unpolarized efficiency of the 1^{st} diffracted order in transmission. The optimization process involved the generation of a master 3-dimensional parameter space cube of the 1^{st} order diffraction efficiency, with depth (d), gap-width (w/Λ) and wavelength (λ) varied from 0 - 3 μm, 0 - 100% and 450 -

750 nm respectively as shown in Figure 3.2.A. The figure is reprinted from [1] and has the notation p for period instead of Λ. Figure 3.2B shows a two-dimensional slice from the parameter cube at a fixed gap-width, with the diffraction efficiency computed as a function of the wavelength and depth. An optimum depth where the overall efficiency goes to $\sim 95\%$ for the operating mid-band wavelength is chosen. The figure illustrates the design of the "green" spectral channel grating. The "red" grating was optimized using a similar approach, which resulted in a gap-width of 30% (170 nm) and a depth of 1.65 μm.

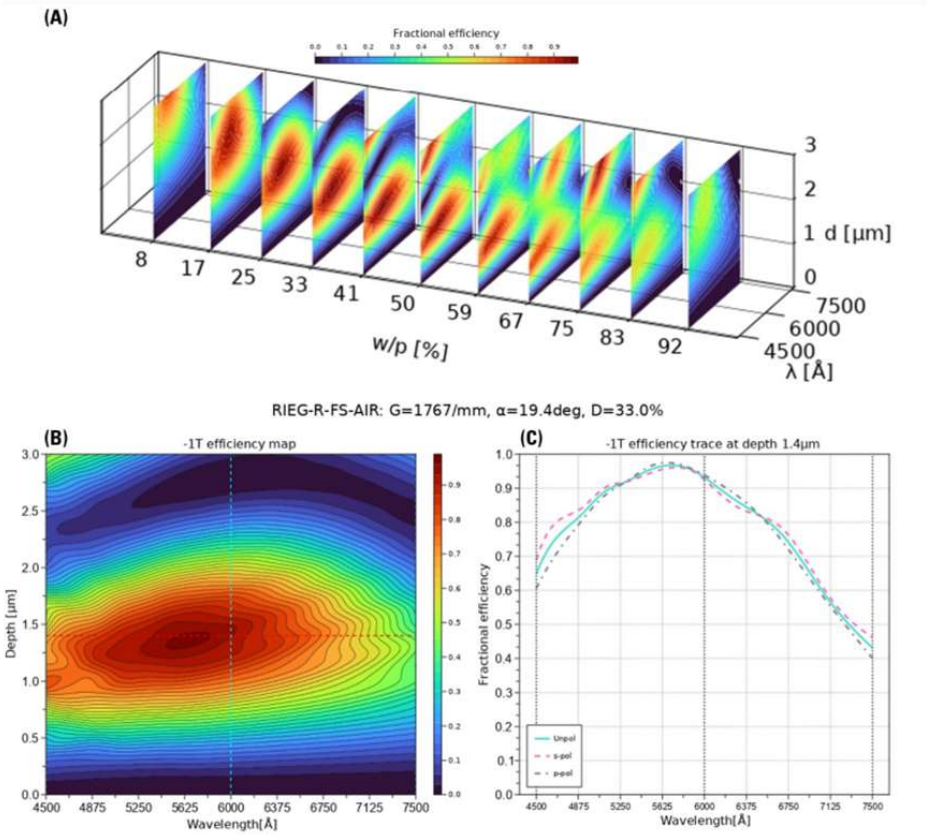

Figure 3.2: Reprinted from [1]. Efficiency of 1^{st}-order for the design of a "green" grating A) as a function of wavelength (λ), grating depth (d) and gap width (w/p) B) as a function of λ and d at optimum w/p and C) as a function of λ for optimum d.

Fabrication of the numerically optimized design grating was done using e-beam lithography as explained in section 1.2.2. For the POC RIPLE grating the reactive gas used was CHF_3 under a 1000 W radio frequency RF signal. To achieve the design etch depth, etching process parameters were varied. These include reactive gas flow rate, RF power, substrate temperature, chamber pressure, and particularly the etching duration. Each of these factors affects the etch depth differently and must be carefully balanced to ensure a consistent increase in depth. Proxy gratings were used as test dummies to fine-tune these parameters and achieve optimal depths. Consequently, during mask design, the entire writing area was divided into four sections, each featuring a grating pattern of 25.4 x 25.4 sq.mm area in the center, to use as proxies.

To dice the mask into four quadrants, a dicing saw with diamond blade was used. A spindle of 18000 rpm was set for the blade with a forward cutting speed of 1mm/s. These thin blades could cut only 1 mm deep at a single pass and atleast three passes along the same dicing line was required both from the top surface and bottom surface to cut the quarter inch thick substrate. One of the four quadrants was further divided into nine smaller sections, as illustrated in Figure 3.3 (left), to create smaller proxy gratings for process development. Prior works have optimized combination of variables like RF Power, CHF_3 flow rate, O_2 flow rate etc in the past and only the duration of etch was varied for different proxies. It is important to note that the optimal etch duration for the smaller proxy grating needed to be slightly increased when applied to the larger surface area grating. This is because, as the etch area increases, the plasma saturation also increases. This will be discussed in detail in Section 3.3. The final POC RIPLE grating, achieving a target depth of 1.65 μm, is shown in Figure 3.3 (right).

The analysis of grating depth after each proxy etch was conducted by comparing the measured and numerically simulated transmission spectra of the 0^{th} order at

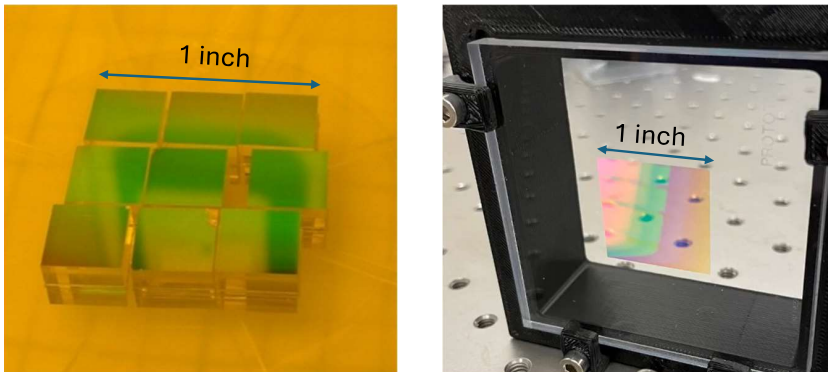

Figure 3.3: Reprinted from [1]. Left: 1x1 sq. inch grating diced into 9 small proxy gratings for tuning the etching parameters. Right: The final 1x1 sq. inch POC-RIPLE grating after wet chrome etch. The proxies in the figure still have chrome on.

normal incidence in s- and p-polarization states as shown in 3.4 A and B respectively. The measured spectra, shown in orange, were obtained using the Woollam Variable Angle Spectroscopic Ellipsometer (WVASE) for both polarizations. The numerical simulation of the grating model, performed using the RCWA algorithm, is represented by the black lines (from UNCC's in-house RCWA package) and the grey lines (from GA Solver at UTA) in the figure. A direct imaging of the grating using Scanning Electron microscope (SEM) in figure 3.4 C shows that the pillars have a height of 1.25 μm, consistent with the depth predicted by the numerical simulations in 3.4. This validation confirmed that the depth verification process through numerical model comparison was accurate, thereby eliminating the necessity for SEM imaging after each etching step.

3.1.3 Spectral measurements

The spectral performance of the POC RIPLE grating in transmission was tested using the WVASE. In the setup, the source remains fixed while the sample is mounted on a rotation stage. This stage rotates along the y-axis to achieve the desired angle of incidence as shown in figure 3.5. The detector rotates along the dotted circle in the xz plane although higher angles of collection are limited by the mechanics of the tool. The source is a Xenon lamp connected to a monochromator, allowing the

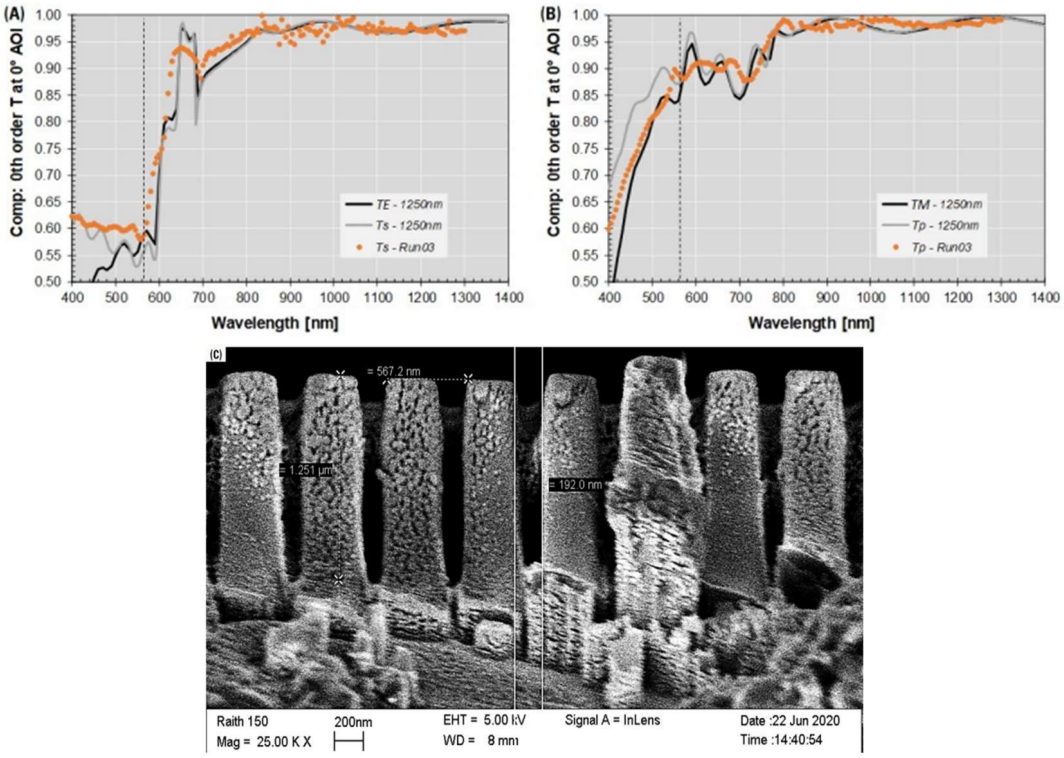

Figure 3.4: Reprinted from [1]. Depth analysis by comparison of measured (orange) 0^{th} order transmission spectra to numerically simulated (black and grey) one for the A) s polarization and B) p polarization both indicating a depth of 1.25 μm. C) Scanning Electron Microscope (SEM) image of the grating with 1.25 μm high pillars and 567 nm spacing

selection of a specific wavelength or wavelength range. Aligning the grating lines to be exactly perpendicular to the xz plane in this tool is very difficult. As a result, the dispersed first order deviates from the plane of the detector sweep, making the first-order measurements less accurate. However, the 0^{th} order remains in the xz plane and was measured at a 36.4°angle of incidence. This method was used to test the performance of the grating, as a highly suppressed 0^{th} order indicates a highly efficient 1^{st} order, provided that light is not lost to reflection, scattering, or higher orders. To ensure high efficiency, the 1^{st} order spectral measurement was performed at the University of Texas at Austin (UTA) using their grating tester.

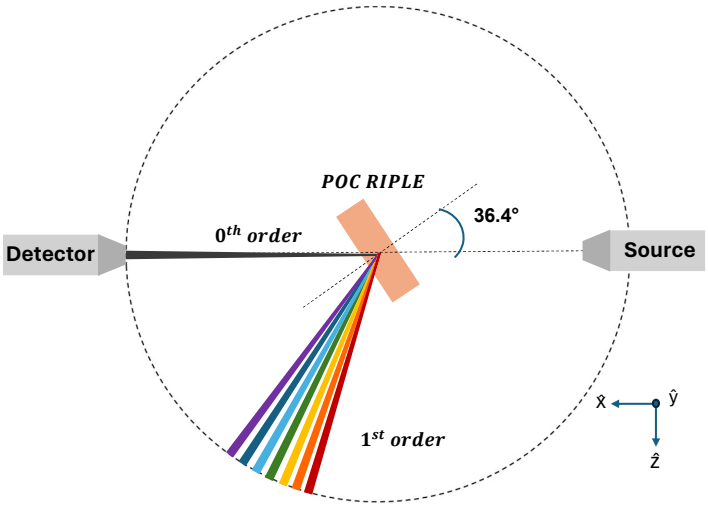

Figure 3.5: Layout of the WVASE instrument. The detector moves around the dotted line within mechanical limits. The POC RIPLE on a rotating holder along the y-axis allows precise incidence angle adjustment. The 0^{th} order aligns with the source for accurate measurement, while the 1^{st} order may deviate slightly due to grating alignment errors, making it harder to measure accurately.

3.1.4 Results and Conclusion

The final depth of the POC RIPLE grating was estimated to be 1.6 μm, based on the comparison of measured and simulated transmission spectra presented in Figure 3.6A and 3.6B for p- and s-polarizations, respectively. Similar transmission spectra, but with an incidence angle of 36.4°, are shown in figure 3.6C for the 0^{th} order. Note that the y-axis, representing transmission, is in logarithmic scale in this case. The 0^{th} order is well suppressed in both polarizations. For p-polarization, the transmission is 1.74% at 658 nm, while for s-polarization, the transmission is less than 1% over a range of 666 nm to 716 nm, reaching a minimum of 0.27% at 690 nm, indicated by black dotted lines in Figure 3.6C. The transmission spectrum of the 1^{st} order, measured at McDonald Observatory and shown in Figure 3.6 D, confirmed that the efficiencies of 1^{st} order is reaching 94% for unpolarized light at a wavelength of 650 nm. This satisfies the design requirements. The red shaded region indicates the

wavelength band where efficiency exceeds 70%, extending from 550 nm to 760 nm. The performance of the RIPLE grating significantly surpasses that of the conventional VPH gratings previously used at McDonald Observatory.

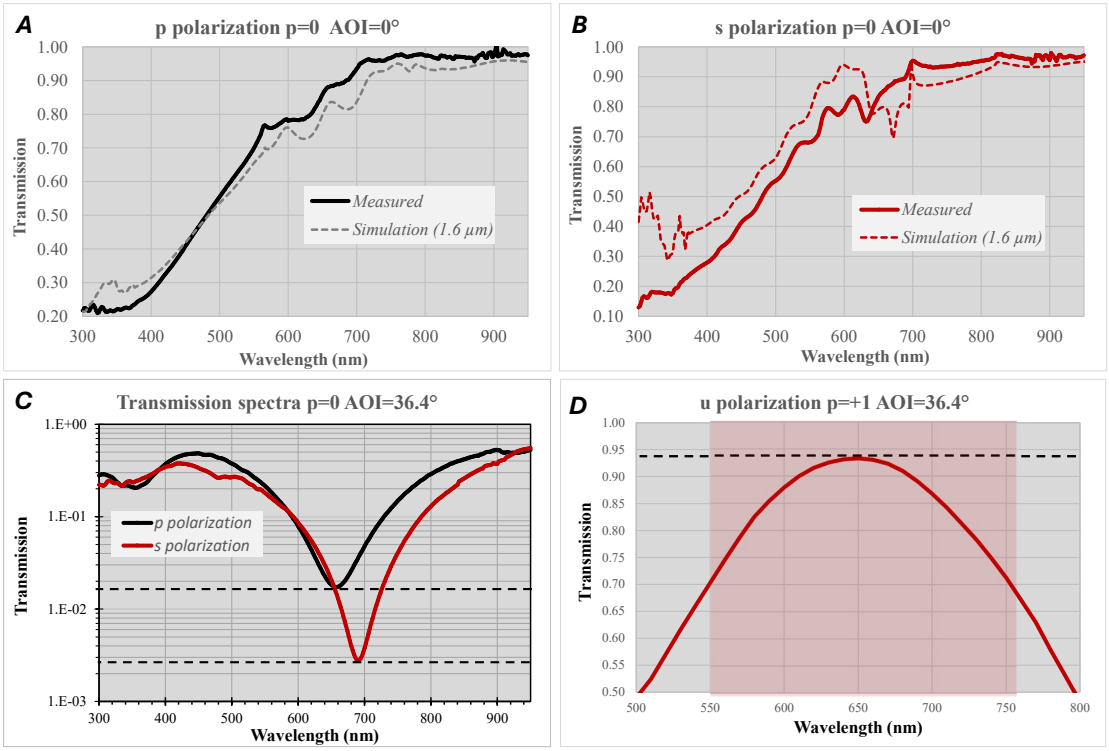

Figure 3.6: Comparison of the measured (solid) and simulated (dotted) 0^{th} order transmission spectra of the numerical model and actual POC RIPLE grating at normal incidence for the A) p polarization and B) s polarization. C) Measured transmission spectra at 36.4°angle of incidence for C) the 0^{th} order at both polarizations shown in logarithmic scale and D) the 1^{st} order at u polarization

In conclusion, we successfully designed, fabricated, and tested a proof-of-concept surface relief 1^{st} order grating in transmission. This grating suppressed the 0^{th} order to less than 1% and enhanced the 1^{st} order to above 90% around a wavelength of 650 nm. The e-beam lithographic technique accurately generated the grating pattern on the substrate. The reactive ion plasma etch process, due to its anisotropic nature, etched the grating in one direction without significant chipping or cracking of the edges, maintaining the rectangular shape of the grating. This technique successfully fabricated grating features with a high depth-to-width ratio of the grooves (known as

aspect ratio), achieving a ratio of 10:1. The development process remained consistent across multiple samples, with only slight deviations in the etching parameters as the surface area of the grating increased. The alignment between the numerically simulated transmission spectra of a perfectly rectangular grating model and the actual measured transmission spectra confirms the accuracy of this fabrication technique.

POC RIPLE gratings fabricated using this technique offer a promising alternative to Volume Holographic Gratings (VHG) for spectroscopic applications. They provide high throughput efficiency and a monolithic structure, which ensures superior mechanical and thermal stability compared to VHGs. These qualities make POC RIPLE gratings highly suitable for instrumentation not only on earth but also in the harsh conditions of space observatories. So far, what we have fabricated and tested is a proof of concept. For the RIPLE grating to be useful in the actual telescope instrumentation, two issues need to be addressed. Firstly, the gratings are operated in the Littrow angles of incidence, which create Littrow recombination ghost images. These ghost images are caused by reflections off the detector that recombine back into the grating, creating unwanted images at the telescope focus. We reduced the ghost order intensities in the RIPLE grating by applying antireflective treatments to the back of the substrate and using slightly off-Littrow incidence, as detailed in section 3.2. Secondly, ground telescope instrumentation requires large aperture sizes to collect more light, necessitating optical elements like the RIPLE grating to have surface areas larger than 100x100 mm. The POC RIPLE is only 25.4 $\times$ 25.4 mm, so the reactive ion etching process needs to be adjusted for larger surface area gratings. Section3.3 discusses the fabrication difficulties encountered with larger surface area gratings and how they were overcome to create highly efficient RIPLE gratings with a surface area of 150 x 150 mm.

3.2 Reduction in Littrow recombination ghosts in 1st order gratings

3.2.1 Introduction

[2].In the previous section, the focus was on enhancing the first-order efficiencies of diffraction gratings for astronomical spectroscopy. While this is crucial for observing faint astronomical targets, some trade-offs associated with operating the grating in the "Littrow configuration" were overlooked. This configuration occurs when light is incident on a grating at the Littrow angle, where the reflected or transmitted first order retraces the incident path (Refer to section 1.3). Research has shown that, in this configuration, gratings become highly efficient in the first order [8]. An example of this is the POC RIPLE grating in section 3.1, where the angle of incidence was about 36° which, according to the diffraction equation (equation 3.1), is the Littrow angle of incidence at a 670 nm wavelength. When the grating is deployed at Littrow angles during the actual imaging of the astronomical objects, the first order often reflects off of the detector, recombines with the grating and re-images at the telescope focus forming spurious spectral features known as Littrow recombination ghosts [9]. This section will discuss how to reduce the intensities of these ghost images.

Large-area (greater than 150 mm in linear dimension) first-order Volume Phase Holographic (VPH) transmission gratings, mounted at oblique angles of incidence, are routinely used for the UV−visible−NIR spectral range. These VPH gratings are typically sandwiched between two glass substrates. In such configurations, the main spectral order deflected from the detector can recombine back into the grating, reflecting from the front of the substrate, the back of the substrate, or the grating surfaces, causing recombination ghosts. To mitigate this issue, the front and back substrates are slanted to deviate the reflected light away from the system. As mentioned in the previous section, high-efficiency monolithic binary gratings on fused

[2]This work was Accepted and Presented at CLEO held at Charlotte, USA, on May 2024. To appear at CLEO proceedings

quartz were fabricated and tested, demonstrating superior spectral efficiency compared to conventional VPH gratings [10]. For the RIPLE grating, there is no front substrate and also the design is such that the reflections are low. This means that the chances of recombination ghosts arise mostly from reflections at the back side of the substrate. To reduce these undesirable ghosts, broadband AR-coatings on the back of the substrate and slightly off-Littrow incidence mounting is required. The substrate's non-dispersive surface was treated with AR random nanostructures (rARSS) to achieve a "featureless" broad spectral transmission across visible wavelengths [1]. Bidirectional-scatter transmission distribution function (BTDF) measurements were conducted to identify the positions and intensities of Littrow ghosts. These measurements, with a relative signal sensitivity of 8 orders of magnitude compared to the highly efficient 1^{st} order, quantify the strength of the features for the monolithic 1^{st} order RIPLE grating treated with rARSS.

3.2.2 Fabrication and Testing

A linear 1^{st}-order spectrographic grating with a 566 nm period and a 50.8-by-50.8 mm^2 surface area was designed and fabricated on a 6.35 mm-thick quartz substrate, using the same method as for the POC RIPLE grating described in section 3.1. The reactive ion etching process was adjusted to accommodate the increased surface area of the grating which will be discussed in detail in Section 3.3. Rigorous coupled-wave analysis (RCWA) was used to optimize performance at 35° angle of incidence (off Littrow). The grating's 1^{st} diffraction order was designed to have a transmission greater than 70% in the range from 568 nm to 773 nm, peaking as 95% at 633 nm.

These specifications necessitated a $\sim$1.6 μm-deep etch of the 169 nm-wide line-groove into the quartz substrate. The fabrication of the grating was achieved using direct write e-beam lithography on Cr-coated quartz, followed by reactive-ion etching process using methyl-fluoride (CHF_3) in a 1000 W RF-driven plasma [10].The technique of using proxy gratings as dummies to achieve the correct depth, as discussed in

Section 3.1, was followed here. The next crucial step in the fabrication process was to monolithically etch randomly distributed columnar nanostructures directly onto the optical substrate's flat surface to act as an AR treatment [11]. These nanostructures have been shown to have polarization insensitive transmission enhancement independent of the angle-of-incidence, for angles as high as the Brewster's [12]. The same recipe as for the cylindrical and freeform element detailed in Section 2.2 was used here.

Birectional transmission distribution function of the grating at 633 nm wavelength was measured using the complete equatorial-angle scatterometer instrument (CASI, Schmitt Industries Inc.). The same instrument was used for scatter measurements of the freeform component in Section 2.3. The grating was mounted at an angle of incidence of 35° (near Littrow). The instrument is capable of measuring scatter as the ratio of radiance to irradiance, over the full plane of incidence in the transmission direction. Since the measurement is in transmission, the detector sweeps from $-90°$ to $+90°$. Here the instrument's reference is with respect to the test sample's orientation which is -35° in this case, resulting in a detector sweep from -125° to 55°. The aperture diameter of the Si detector was fixed at 0.338 mm throughout the entire sweep. Initial measurements were taken with the grating facing the detector. To further examine these ghosts, the grating was oriented facing the source, and the measurements were repeated.

3.2.3 Results

Transmission measurements of rARSS structures on witness quartz samples have shown average enhancement of 3% per surface, from 96.5% to 99.5%, in the 350-1000 nm wavelength range [1]. The single side transmission enhancement of the witness quartz at normal angle of incidence is shown in figure 3.7. The measurement was taken using the CARY60 grating spectrometer from Section 2.3. In the figure, the black curve represents the untreated quartz substrate with a typical transmission of 93% in

the visible wavelength range. The green curve shows the enhanced transmission (96%) after rARSS treatment on one side of the witness sample. The green shaded region indicates the wavelength range for which the RIPLE grating is designed. Within this region, the green curve is broadband, featureless, and exhibits enhanced transmission.

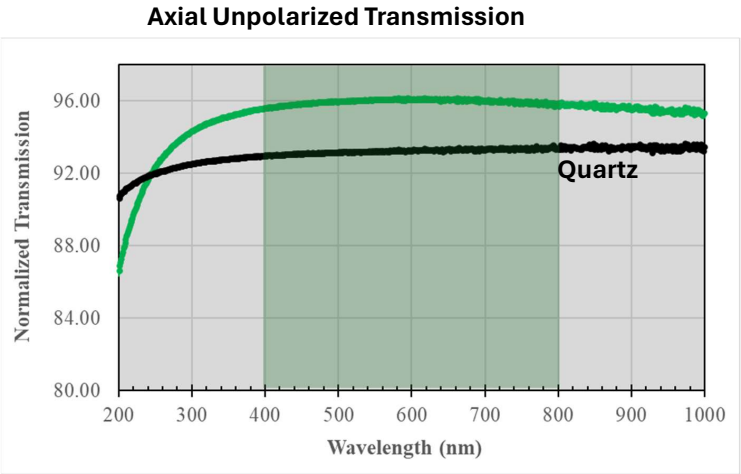

Figure 3.7: Enhancement upto 3% in the transmission of quartz witness sample after rARSS treatment (Green curve) compared to the unprocessed quartz (Black Curve). Green shaded region shows the operational wavelength range of the grating where the rARSS performance is featureless and enhanced.

Figure 3.8 shows the two orientations of the grating (facing the detector and source) with their corresponding BTDF as a function of angle of collection shown on the right. From figure 3.8A and C, all possible paths that the incident light can take after diffracting through the grating and reflecting from the substrate are depicted as dotted red lines within the substrate region. The paths that emerge from the grating are shown as bold red arrows. The actual 0^{th} and -1^{st} orders are labeled as 0 and 1, respectively, while the remaining paths are ghost orders caused by reflections from the back of the substrate. These ghost orders are named based on the sequence of their diffraction paths. For instance, "11" denotes the diffracted first order in transmission resulting from the diffracted first order reflected by the flat surface on the opposite side of the grating. The number of digits in the nomenclature indicates the cycles of

diffraction; for example, 101 represents the diffracted ray that emerges after the third interaction with the grating.

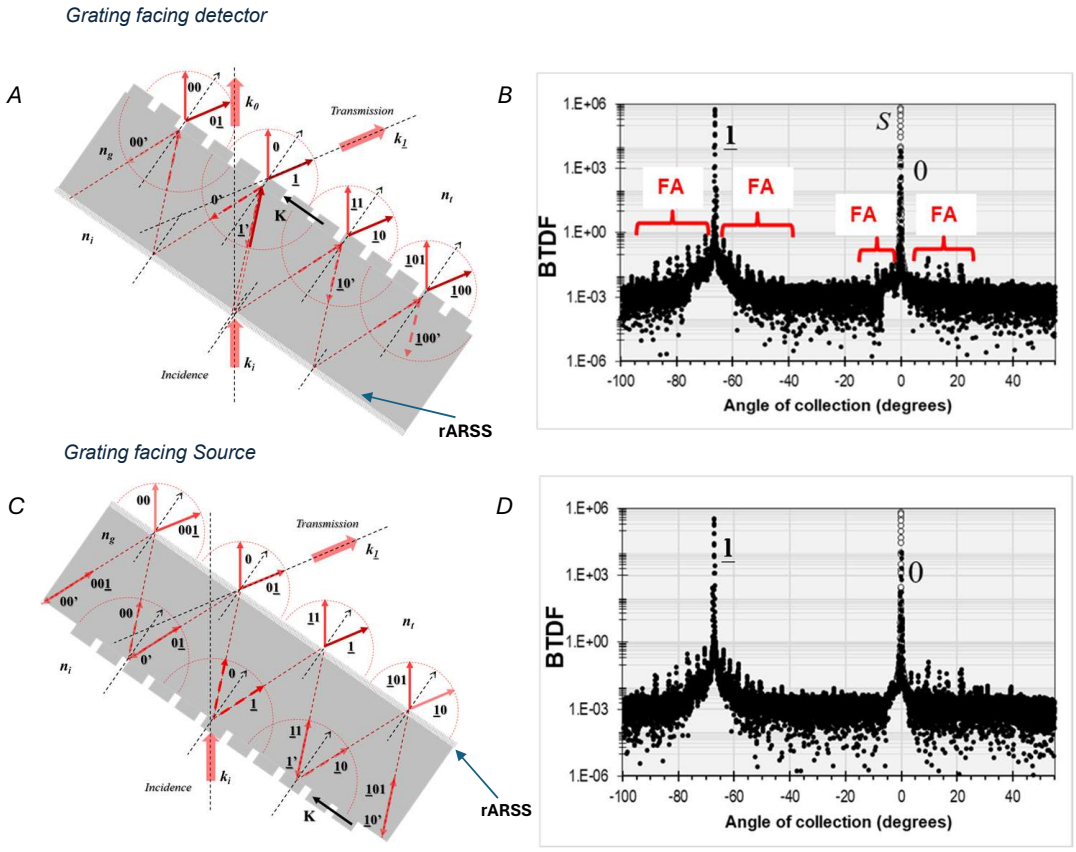

Figure 3.8: Near-Littrow incidence test mounting for the grating with the grating facing (A) the detector and (C) the source. The incidence (k_i), the axial 0^{th}-order (k_0), and -1^{st}-order diffraction ($k_{\underline{1}}$) directions are indicated. BTDF in logarithmic scale as a function of the angle of collection for the grating facing (B) the detector and (D) the source. The signature (baseline) of the CASI instrument is shown as white data points along the axial direction. Fabrication artifacts (FA) are identified adjacent to the propagating orders.

In general for all the orders, both actual and ghost, there are only two directions of propagation denoted by the thick red arrows with propagation constants k_0 and k_1. These directions mainly represent the 0^{th} and -1^{st} order which appear as peaks in the corresponding BTDF graphs, separated by approximately 67°, in agreement with the diffracted-angle calculations. According to the diffraction equation, $\theta_{-1T} = -33°$

and $\theta_{0T} = 35^{\circ}$ at θ_{inc}=35°, summing to 68°. We also accounted for the lateral shift ($\sim -0.6^{\circ}$) of light due to the quarter-inch thick substrate. Both figures are overlaid with the signature (No Sample) of the CASI instrument, shown as white data points and marked as "S". A number of ghost-lines are identified at regular intervals of ∼3° near the propagating diffraction orders tagged as "FA", which stands for Fabrication Artefacts, in figure 3.8B and D. These ghost-line peaks are lower than 6-orders of magnitude compared to the functional -1^{st} order peak value, indicating efficient suppression from the rARSS modified substrate back surface. We are investigating possible fabrication causes for these peaks, as their angular placement does not align with Littrow Ghost conditions and is most likely coming from the stitching errors during the e-beam mask writing of the grating. The actual ghost orders lie very close to the 0^{th} and -1^{st} order and can be seen clearly in the expanded view of the BTDF graph near the -1^{st} and 0^{th} as shown in figure 3.9 A and B respectively. The integrated BTDF values under each peak was compared to find suppression ratios of the ghost peaks w.r.t to the signature and highly efficient -1^{st} order. Table 3.1 shows the integrated suppression ratios of all the ghost orders with respect to the -1^{st} order for both grating orientations.

The results indicate that the integrated suppression ratio for the 0^{th} diffracted order, compared to the -1^{st} order, is 1.20:100 when the grating faces the detector and 1.87:100 when it faces the source, as shown in the table. Additionally, the suppression ratio relative to the axial signature of the instrument's baseline was measured to be approximately 1.14:100 with the grating facing the detector and 1.05:100 with the grating facing the source. All of these measurements meet the design goals. Note that the value for the 1st order is 1.00 in the table because the ratios are relative to the -1^{st} order itself. From the table, the Littrow Ghost orders have suppression ratios in the range of 10^{-4}:1 to 10^{-7}:1 with respect to the -1^{st} order. This suggests that the tallest ghost order peak is less than four orders of magnitude compared to

Table 3.1: Integrated suppression ratios of the ghost orders w.r.t first order

(a) Near 1^{st} order

	Grating to detector	Grating to Source
$\underline{1}00$	–	1.2×10^{-6}
$\underline{1}0$	6.33×10^{-6}	7.56×10^{-4}
$\underline{1}$	1.00	1.00
$0\underline{1}$	1.87×10^{-4}	–

(b) Near 0^{th} order

	Grating to detector	Grating to Source
$\underline{1}01$	3.89×10^{-7}	6.82×10^{-7}
$\underline{1}1$	2.67×10^{-4}	4.47×10^{-4}
0	1.20×10^{-2}	1.87×10^{-2}
00	2.82×10^{-6}	2.52×10^{-5}

the -1^{st} order peak.

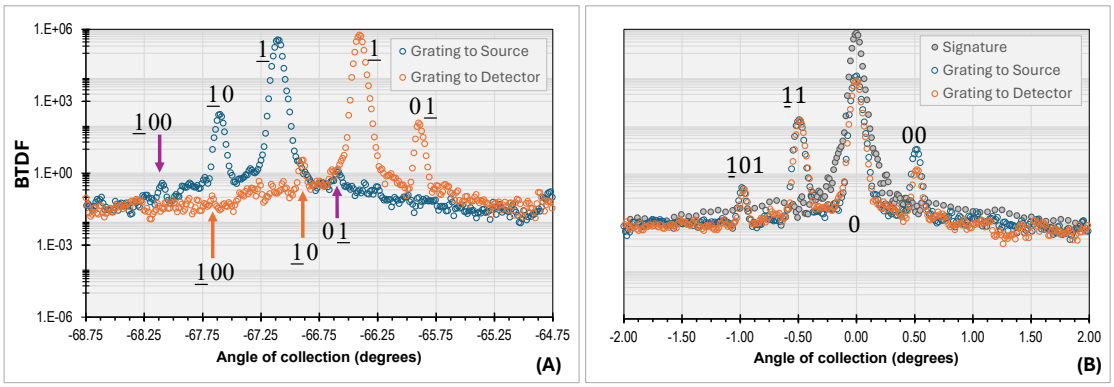

Figure 3.9: Measured BTDF for ±2° near the: (A) -1^{st} and (B) 0^{th} orders for two different orientations of the grating. The Littrow recombination ghosts correspond to the directions in Fig.3.8A and C .

The Fresnel reflection losses at the backside-air interface and diffraction efficiencies at the grating-air interface were simulated using RCWA. The efficiencies of the ghost orders after multiple reflections agree well with the integrated angular radiance of the BTDF for each ghost order. The angular separation between the ghost peaks

($\sim 0.5^{\circ}$) aligns with the angle corresponding to the lateral displacement caused by the substrate thickness, thereby further validating the accuracy of the ghost order locations. Additionally, the -1^{st} orders for both grating test orientations are separated by approximately 0.6° from the incidence axis, also due to the angular displacement resulting from the substrate thickness.

3.2.4 Conclusion

To the best of our knowledge, there are no scatterometric measurements reported to-date for astronomical high-resolution spectrographic gratings. We have successfully identified the positions and intensities of Littrow recombination ghosts in the 1^{st}-order transmission grating that was fabricated. With the current grating design, which features highly suppressed reflections and antireflective treatment (rARSS) on the back of the substrate, the intensities of the Littrow ghosts are reduced by four orders of magnitude compared to the highly efficient -1^{st} order. Additionally, since both fabrication steps involve monolithic etching of the quartz substrate, the RIPLE grating presents a viable alternative to VHG gratings, particularly in terms of thermal and mechanical stability - an essential factor for space telescope instrumentation.

3.3 Large surface area grating fabrication

[3]Over the past two years, our research has focused on the accuracy of the fabrication process for RIPLE gratings. The fidelity and repeatability of this process have been successfully tested using proxy gratings. Additionally, spectral measurements from these prototypes align well with the numerical model simulations discussed in section 3.1. Careful manual inspections of the grating features revealed no significant defects introduced by the process, and different areas of the grating were tested for uniformity. However, these prototypes need to be scaled up to be useful in actual spectrograph units for extremely large telescopes. Scaling up is particularly critical in astronomy, where grating clear apertures need to be at least 4 inches in diameter and can reach up to 12 inches, depending on the beam sizes of many existing and planned spectrographs for 4-10 meter class telescopes. Unlike the millimeter-scale devices used in micro-optics, this represents a substantial increase in device area, necessitating precise processes to uniformly write and etch nano-scale grating structures over large substrates.

The standard e-beam lithography tool that is used to make the hard chrome mask can reliably write up to 5×5 in^2 mask pattern on 6×6 in^2 Quartz substrate without sabotaging the critical dimension accuracy of few nanometers. We exploited this capability of the tool to scale up the RIPLE grating area from the 1×1 in^2 (POC RIPLE) to 2×2 in^2 all the way up to primary 4×4 in^2 area target gratings. This section discusses the fabrication challenges encountered during this process and the slight deviations from conventional techniques implemented to achieve the target depth. The transmission spectra for each grating at various area scales are also presented in the results section.

[3]This work was Accepted and Presented at SPIE Astronomical Telescopes + Instrumentation conference held at Yokohama, Japan on June 2024. To appear at SPIE conference proceedings.

3.3.1 Fabrication difficulties

Similar to the approach taken for the POC RIPLE grating, the etch times were adjusted for various sizes of proxy gratings, ranging from 8.5×8.5 mm^2, 12.7×12.7 mm^2, 19×19 mm^2 , 25.4×25.4 mm^2 to 50.8×50.8 mm^2, in order to achieve the target grating size of 101.6×101.6 mm^2. Figure 3.10A displays the 50.8×50.8 mm^2 and 101.6×101.6 mm^2 gratings with their dimensions marked in inches, while Figure 3.3 shows the smaller proxy sizes. The proxies were dry-etched using the same parameters discussed in section 3.1, with methyl-trifluoride (CHF_3) and oxygen (O_2) reactive gases and a radio-frequency (RF) power of 1000W. This was followed by a wet etch to remove any residual chromium (Cr), resulting in a monolithic quartz binary grating. Several proxies of the same dimensions were used to study etch depth as a function of time.

With each iterative increase in area, several factors need to be addressed during the reactive ion plasma etch process, such as early plasma saturation due to more volatile by-products, which can lead to a slower net etch rate. There is a knowledge gap in the current etching system regarding how power laws govern the relationships between individual etching parameters - such as CHF_3 flow rate, RF power, pressure, temperature, and etch rate. This gap poses a fabrication challenge for scaling up the area, as it is unclear how much these parameters need to be adjusted. This necessitates a detailed experimental study with proxy gratings to validate these relationships. Due to time constraints, only the etch time was varied with each increase in area scale.

Figure 3.10B illustrates the variation of etch depth as a function of etch time for various dimensions of proxies shown in different colors and marked as ‘Z’, ‘Y’, ‘X’, ‘W’ and ‘V’ with their corresponding dimensions marked in the graph. Note that the depth analysis was done using the standard technique described in section 3.1. In the graph, the green dotted horizontal line represents the target depth of the design which is approximately 1.65 μm. The red vertical dotted lines indicate the etch time

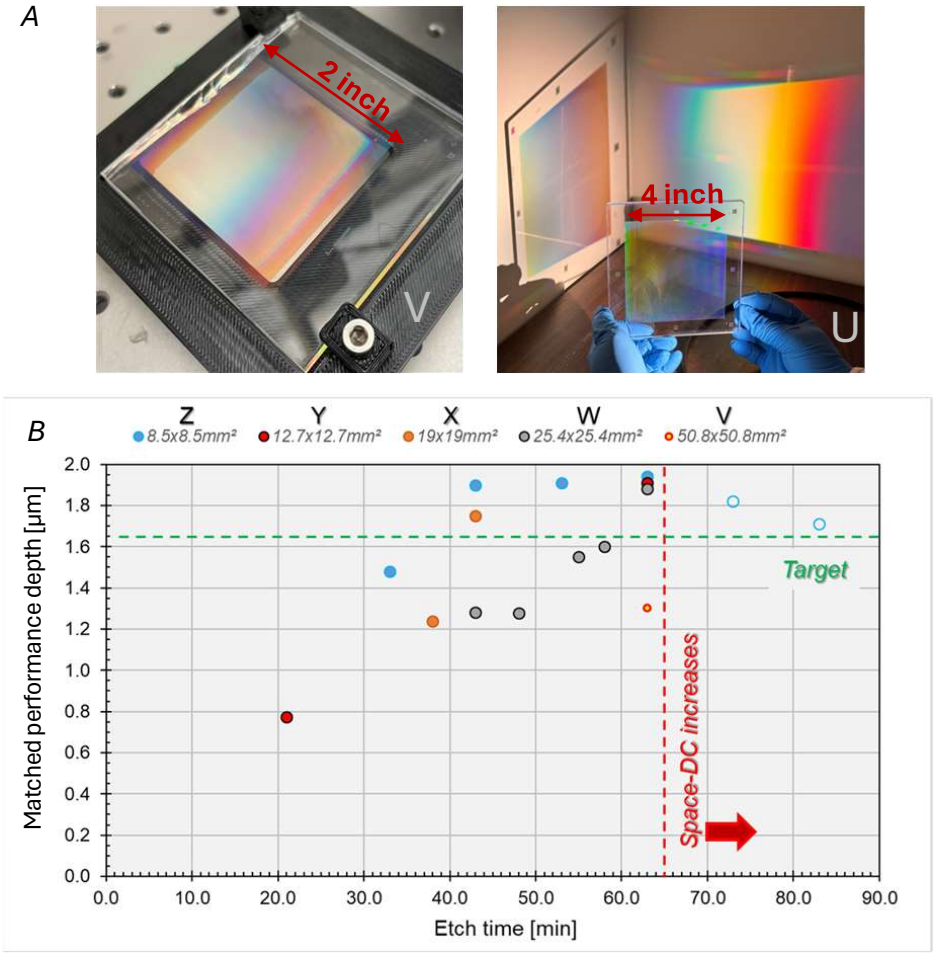

Figure 3.10: A) Proxy gratings of 2 inch ('V') and the 4 inch target grating ('U') shown with their dimensions marked. B) Depth of the grating as a function of time of etch for different sizes of proxy gratings shown in different colors. The green horizontal line is the target depth of the design and red dotted line is the maximum etch time affordable without Chrome layer depletion.

after which the 110 nm metallic chrome layer is completely exhausted. Beyond this point, the protective chrome coating is compromised, leading to faster etch rates of the exposed quartz on the top of the grating compared to the deeper groove channels, where the reactive gases have limited access. This causes non-uniform etching and chipping of the edges, leading to changes in the fill factor of the grating. The hollow dots on the graph denote gratings whose fill factor has been altered. Prototypes with dimensions less than 1 inch reach the target depth before the red dotted line.

However, the 2-inch grating, denoted by hollow red dot, is still 350 nm short of the target depth at the chrome exhaustion line. This poses a problem, as the 4 x 4 square inch grating is expected to fall even shallower in depth. The current lithograhic tool used for the mask generation cannot increase the metal chrome thickness beyond 110 nm to prevent early chrome exhaustion during the etching process. A proposed solution to get to deeper gratings was to redeposit Chrome on these shallow gratings at an angle and is explained in detail below.

3.3.2 Proposed Solution

In the work by E. Bernhard Kley et al. (1999), high aspect ratio gratings with depths up to 3.5 μm for a 440 nm period grating with a 100 nm gap were fabricated [13]. Their technique was adopted to address this fabrication challenge. Figure 3.11 illustrates the steps involved in this iterative chrome redeposition technique. The process begins with the same steps used for the POC RIPLE grating, progressing to a shallow monolithic binary quartz grating. Next, chrome is redeposited at a 45° angle from both sides of the grating, forming a protective coating on the top and sidewalls of the grating, but not on the grooves. This is followed by a reactive ion plasma etch that targets only the exposed quartz at the bottom, resulting in deeper grooves. Excessive chrome is then removed using a chrome etchant. The chrome redeposition and etch steps can be repeated several times to achieve the desired depth.

With the clean room facility support at UNCC, a sputtering tool (AJA International) was used to sputter chrome on the grating at 45°. This tool has a magnetron sputtering source driven by DC power supply with the source head tilted at an angle allowing for off axis deposition. The system has heavy duty hoist mechanics to lift the chamber top for easy access of the inside which was exploited to achieve the 45° alignment of the grating with the source head. The rotation of the substrate holder that usually ensures uniform thin film coating was turned off manually in this case to maintain the alignment. To ensure that chrome did not clog the grooves of the

grating, it was deposited at 100 W DC power for only 5 minutes in each direction sequentially. This procedure was applied to three proxy gratings (12.7×12.7 mm^2 in area) that had been previously etched to different depths (0.77μm, 1.20μm and 1.26μm). Following redeposition, manual inspection under a microscope confirmed that the grating patterns were intact and that the grooves had not been closed by the chrome. Initially, a shorter etch time of 20 minutes in the reactive ion etcher (RIE) was tested on these gratings to evaluate the robustness of the redeposited chrome coating. A significant amount of chrome remained after the etch, which was subsequently removed using a wet chrome etch process.

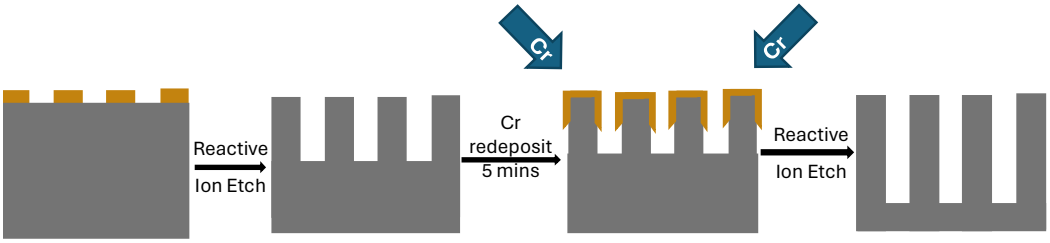

Figure 3.11: Iterative step technique of chrome redeposition off axis on shallow reactive ion etched gratings followed by another plasma etch to achieve deeper grooves.

3.3.3 Results

A depth analysis of the proxy gratings was done before and after the iterative chrome redeposition process. Figure 3.12 A, B and C shows the p polarization transmission spectra of the 0^{th} order at normal incidence for the three proxies. The black and red solid lines on the three graphs represents the measured spectra before and after the process respectively. The dotted curves that represents the numerically simulated transmission spectra at a specific depth matches well with solid lines. The depth changed from 0.77 μm, 1.20 μm and 1.26 μm to 1.03 μm, 1.37 μm and 1.63 μm for the three proxy gratings respectively. Figure 3.12D is a numerically simulated master contour plot that depicts transmission as a function of wavelength and depth

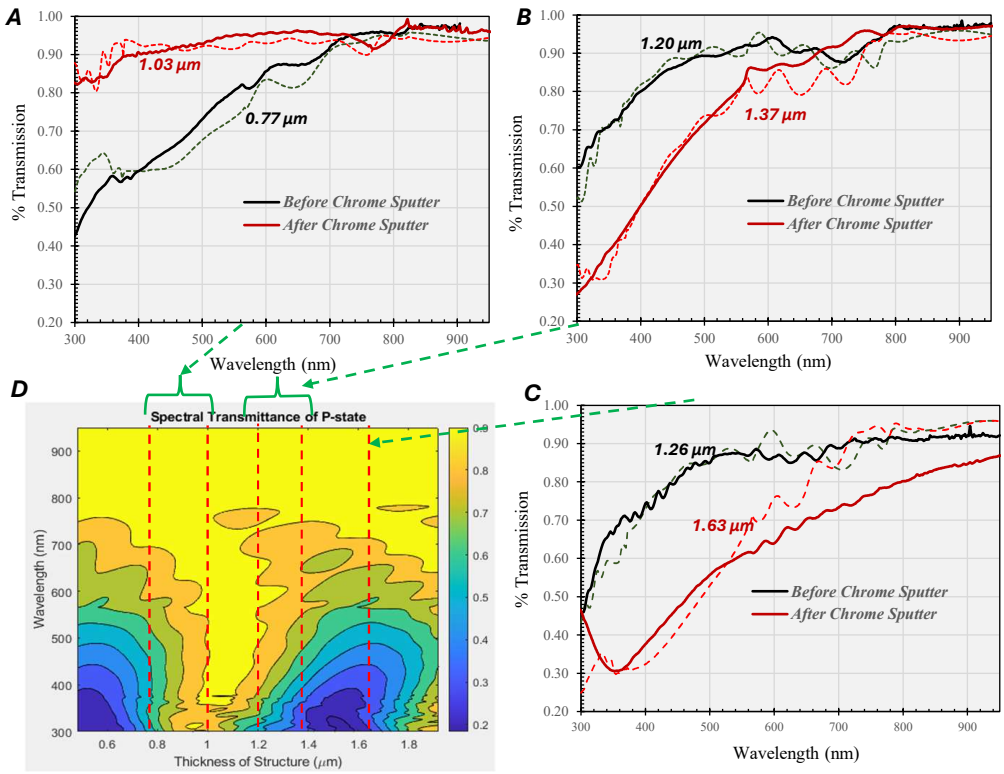

Figure 3.12: Transmission spectra of the p-polarization of three proxy gratings A, B and C before (solid black) and after (solid red) iterative chrome redeposition process. Depth analysis done using RCWA with numerical simulations shown in dotted curves. D) Master Contour plot of transmission spectra as a function of depth with red dotted lines representing the curves in A, B and C indicated by green arrows.

of the gratings from which individual depth curves were adopted. The grating depths are marked in red dotted vertical lines in the contour plot. The increments in depth are 260 nm, 170 nm and 370 nm for the the proxy grating approximately averaging to 270 nm. The reactive ion etching process has shown consistency in previous studies. The variation in increments among different proxies, despite having the same grating area, is due to several reasons like the differences in the surrounding substrate areas around these gratings and the initial depth being different.

Nevertheless the iterative step technique on the gratings with larger surface area (101.6×101.6 mm^2) was endeavored. It took three iterations of chrome redeposition

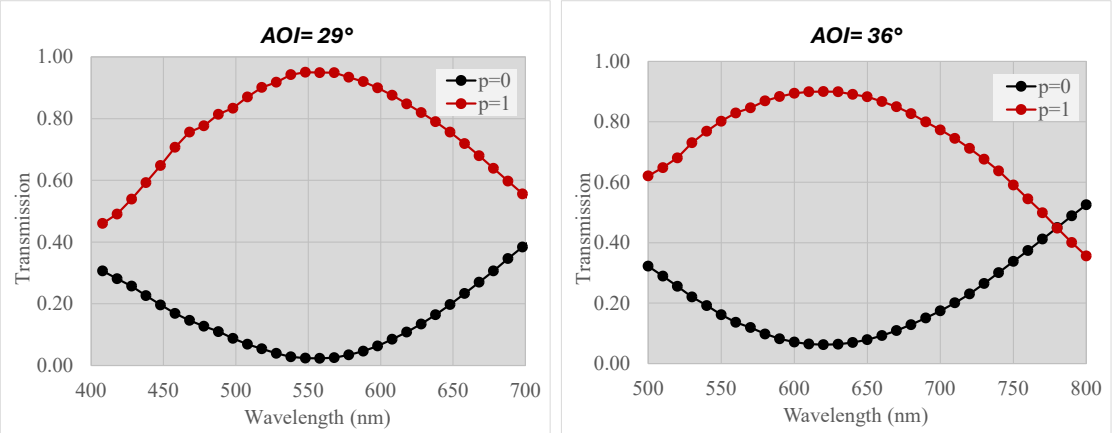

Figure 3.13: Transmission spectrum of the highly efficient 1^{st} order (shown in red) and 0^{th} order (shown in black) of the 101.6×101.6 mm^2 RIPLE grating at A) 29° and B) 36° angle of incidence.

technique to reach the target depth. The functional depth analysis from the 0^{th} order transmission revealed a grating depth estimate of 1μm, 1.2 μm and 1.4 μm after each of the three iterative cycle. Figure 3.13 shows the final transmission data of both orders measured at two different angles of incidence - 29° and 36°. The red curve which represents the 1^{st} order is at the best performance at the angle of 29° peaking to 94.5% at a wavelength of 560 nm and is over 70% for a bandwidth of 210 nm. At 36°, the red curve reaches 90% for a wavelength of about 630 nm and can be tuned to higher efficiency by another iterative step.

3.3.4 Conclusion

The area scaling of astronomical gratings associated with the RIPLE process was briefly discussed. For gratings used in astronomical spectrographs, area scaling is crucial since the clear aperture dimensions of the components can go beyond 4 inches. This is because of the huge beam sizes of such telescopes. In this work, the fabrication challenge associated with etching large surface area, high aspect ratio gratings such as early chrome layer exhaustion during the reactive ion plasma etch process is encountered. To overcome this challenge, the iterative chrome redeposition technique

is demonstrated on 101.6×101.6 mm^2 gratings. The technique involves the deposition of chrome at an angle to prevent coating the grooves while covering the top and sidewalls of the grating. The iterative chrome redeposition technique was tested on three proxy gratings with areas of 12.7×12.7 mm^2, etched to initial depths of 0.77 μm, 1.20 μm, and 1.26 μm. After redeposition, there was significant depth increments in the gratings averaging to 270 nm per iteration and manual inspection these gratings confirmed that the grating patterns remained intact. The iterative chrome redeposition technique, initially tested on smaller proxy gratings, was successfully applied to larger gratings measuring 101.6×101.6 mm^2. Through three cycles of redeposition, these gratings achieved target depths, with final functional depth estimates of 1 μm, 1.2 μm, and 1.4 μm after each iterative step. Transmission analysis revealed optimal performance, with the first order peaking at 94.5% efficiency at a wavelength of 560 nm and over 70% efficiency for a bandwidth of 210 nm at an incidence angle of 29°. At 36°, efficiency reached 90% at a wavelength of 630 nm. These results confirm the robustness and effectiveness of the redeposition technique for large-scale gratings, enhancing their optical performance significantly.

REFERENCES

[1] Hanshin Lee, Uma Subash, and Menelaos K Poutous. Fabrication and evaluation of reactive ion-plasma etched astronomical diffraction grating with anti-reflective surface nanostructures. In *Advances in Optical and Mechanical Technologies for Telescopes and Instrumentation V*, volume 12188, pages 794–805. SPIE, 2022.

[2] Christopher Palmer and Erwin G Loewen. Diffraction grating handbook. 2005.

[3] Song Peng and G Michael Morris. Efficient implementation of rigorous coupled-wave analysis for surface-relief gratings. *JOSA A*, 12(5):1087–1096, 1995.

[4] Elias N Glytsis, Thomas K Gaylord, and David L Brundrett. Rigorous coupled-wave analysis and applications of grating diffraction. In *Diffractive and Miniaturized Optics: A Critical Review*, volume 10271, pages 5–33. SPIE, 1993.

[5] MG Moharam and Thomas K Gaylord. Rigorous coupled-wave analysis of planar-grating diffraction. *JOSA*, 71(7):811–818, 1981.

[6] Gary J Hill, Hanshin Lee, Brian L Vattiat, John M Good, Jason Ramsey, Niv Drory, Trent Peterson, and Briana L Indahl. Virus2: a next generation replicated integral field spectrograph with wide field and broad wavelength coverage. In *Ground-based and Airborne Instrumentation for Astronomy IX*, volume 12184, pages 358–375. SPIE, 2022.

[7] Hanshin Lee, Brian L Vattiat, Gary J Hill, Niv Drory, Jason Ramsey, and John Good. Mix and match as you go: integration/test of the first beam switch module production that splits wavelengths, scrambles beams, and switches fibers for the virus2 instrument. In *Ground-based and Airborne Instrumentation for Astronomy IX*, volume 12184, pages 2091–2105. SPIE, 2022.

[8] RC Enger and SK Case. High-frequency holographic transmission gratings in photoresist. *JOSA*, 73(9):1113–1118, 1983.

[9] Eric B Burgh, Matthew A Bershady, Kyle B Westfall, and Kenneth H Nordsieck. Recombination ghosts in littrow configuration: Implications for spectrographs using volume phase holographic gratings. *Publications of the Astronomical Society of the Pacific*, 119(859):1069, 2007.

[10] Hanshin Lee and Menelaos K Poutous. Reactive ion plasma etched surface relief gratings for low/medium/high resolution spectroscopy in astronomy (erratum). *Journal of Astronomical Telescopes, Instruments, and Systems*, 8(4):049801–049801, 2022.

[11] Karteek Kunala and Menelaos K Poutous. Random antireflective nanostructuring on binary near-wavelength period gratings. *Optical Engineering*, 57(8):087106–087106, 2018.

[12] Abigail Peltier, Gopal Sapkota, Jason R Case, and Menelaos K Poutous. Polarization insensitive performance of randomly structured antireflecting planar surfaces. *Optical Engineering*, 57(3):037109–037109, 2018.

[13] Ernst-Bernhard Kley, Hans-Joerg Fuchs, and Karsten Zoellner. Fabrication technique for high-aspect-ratio gratings. In *Micromachine Technology for Diffractive and Holographic Optics*, volume 3879, pages 71–78. SPIE, 1999.

CHAPTER 4: CROSSED-CELL-TILE MULTIPLEXED 1ST-ORDER GRATINGS FOR THREE-DIMENSIONAL BEAM-SPLITTER APPLICATIONS

4.1 Introduction

[1]Beam splitters are crucial in many applications including: optical interconnections, signal routing, information processing, and active optical component alignment. Beam splitters fabricated on coated thin substrates or pellicles involve challenging manufacturing processes and have lower thermo-mechanical stability, which can cause structural deformations. In contrast, pure dielectric binary gratings offer high thermal and mechanical stability, are compact and have low power losses due to absorption or scatter. Various configurations of gratings have been demonstrated as efficient beam splitters, from simple binary[1] and triangular groove[2] designs, to more complex form-birefringent multilayer structures[3, 4]. Numerous 50/50 polarization-insensitive beam splitters based on dielectric diffraction grating designs have been reported as reflective[5] , transmissive[6, 7] and waveguide coupling components[8, 9]. Besides two-way beam splitters, dielectric binary gratings have also been designed as polarization-insensitive three-way beam splitters, commonly used in holography, interferometry, and photonic crystal fabrication[10, 11]. The majority of beam-splitting gratings are designed to operate in the near infrared spectral range, dividing light equally between the 0^{th} and $\pm 1^{st}-$diffraction orders contained in a single diffraction plane.

Most reported beam splitter gratings operate with the incident ray, the diffracted rays, and the grating-surface normal being co-planar. This chapter addresses de-

[1]Reprinted with permission from U. Subash and M. Poutous, "Crossed-cell-tile multiplexed 1st-order gratings, for three-dimensional beam-splitter applications," *Optics Express* **32**, 38407–38421 (2024).

sign and fabrication of oblique angle-of-incidence beam splitters, resulting in conical diffraction effects. Multilayer-grating conical diffraction beam splitters have been reported for extreme ultraviolet [12] and X-ray [13] applications. These grating devices split light in fixed ratios for given wavelengths and angles of incidence, with efficiencies less than 40%. We propose an efficient and versatile composite-grating device, that can split the incident beam onto diffraction orders contained in intersecting planes in three-dimensions, with design specified beam splitting ratios. In this chapter, the design and experimental demonstration of a two-way and a three-way grating-based beam splitter for visible range wavelength unpolarized spectral applications is presented.

In general, fabrication specifications for diffraction gratings used with coherent monochromatic incident light are very strict. When the spatial period of the grating is mismatched by large-scale fabrication errors, stray light is generated resulting in Rowland ghosts that appear along the diffraction-order distributed spots[14]. Such defects are typical in most fabrication process like electron beam lithography[15] , deep-ultraviolet lithography[16] and direct laser writing[17] , all of which use a sequentially aligned exposure approach during the fabrication of large-area gratings. Using the reference methods, medium-scale (device area of few mm^2) to large-scale (device area of 100's of mm^2) optical gratings are created from many smaller, identical cells (area of 10's of μm^2) arranged side-by-side to cover the entire functional area of the grating device, leading to cell-stitching errors. Although the ghost features are four orders of magnitude less than prominent diffraction orders (As discussed in Section 3.2.4, they may introduce critical artifacts for applications such as astronomical telescope spectrographs[18].

The devices presented in this chapter involve alternating orthogonal cell-tiles of two first-order linear gratings, allowing significant stitching error tolerance due to orientation independence between adjacent tiles. Section 4.2 presents the conical

diffraction principle for the devices breifly, and details the crossed-cell-tile grating device designs, which are to function as polarization-insensitive, two-way and three-way spectral beam splitters, and polarization sensitive beam splitter. A similar crossed-tile layout made of subwavelength grating cells has been used in the past by Deguzman et al. [19] as an antireflective treatment on diffractive beam splitting polarizers[20]. In our work, the crossed-cell-tiles act as spatial light distributors in three spatial dimensions. The polarizer design we are proposing in this work is meant for the visible regime. In Section 4.3 the individual grating cell designs are discussed, using first the Simplified Modal Method to determine the grating structural parameter space extent, and then using Rigorous Coupled-Wave Analysis simulations of the grating cells, to affix the grating parameters to specified beam splitting functions. Fabrication and test results are presented in Section 4.4, followed by our conclusions in Section 4.5.

4.2 Conical diffraction by crossed-cell-tile gratings

The optical response of diffraction gratings at oblique incidence provides insights for the design study done in this chapter and was discussed in some detail in Section 1.4. In the following analysis we chose to have a fixed laboratory frame and tilt or rotate the grating surface normal, as it is equivalent to our experimental component layout.

Figure 4.1A depicts the DO distribution for oblique incidence on a linear, straight-sidewall, binary-profile, transmission grating aligned to the laboratory x-axis ($\alpha_K = 1, \beta_K = 0$), where the propagating DO direction cosines are located along the circular latitude arc intersecting the angular-space sphere. The individual propagating DO direction cosines are the projections to the configuration axes $[\alpha, \beta, \gamma]$. The same configuration-space relations in Equation 1.2 can be obtained if the fixed space-axes are changed from the grating normal to the incidence ray in the laboratory z-axis direction ($\alpha_i = \beta_i = 0, \gamma_i = 1$), with the grating rotated first about the z-axis ($1 > (\alpha_K, \beta_K) > 0$), and then about the new y-axis ($1 > (\alpha_i, \beta_i, \gamma_i) > 0$), as one would

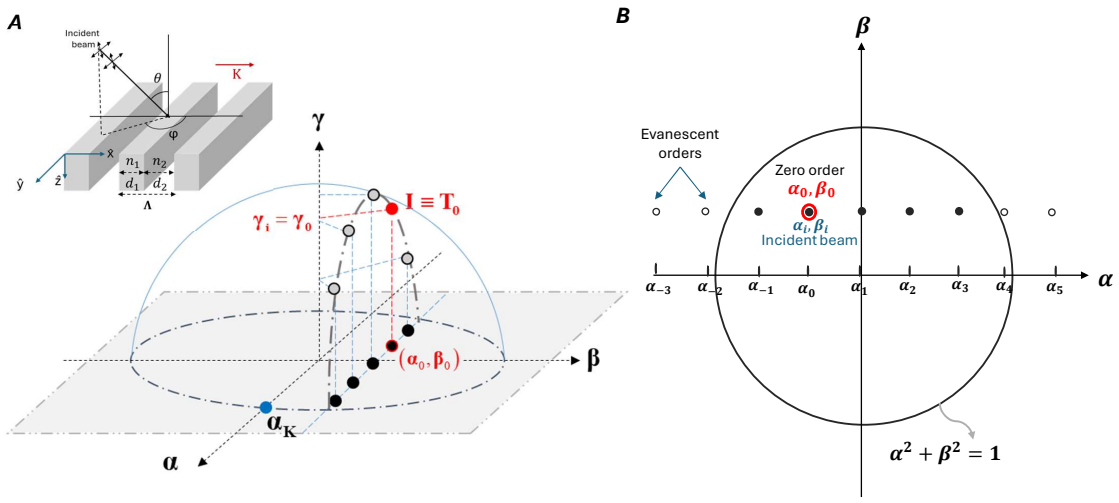

Figure 4.1: A) Direction cosine $\alpha\beta\gamma$-space unit-hemisphere illustrating the transmission DO angular distribution for oblique incidence directions α_i, β_i, γ_i. The grating vector direction is represented by a single point: $\alpha_K = 1$ (with lines parallel to the laboratory y-axis as shown in the inset.) The inset shows the laboratory frame-grating orientation. B) The direction cosine $\alpha\beta$-plane, where the DO projections are equally spaced, along a single line parallel to the α-axis for the conditions shown in the inset.

have to do when testing the grating. Harvey refers to the $\alpha\beta$-plane as the direction-cosine space (Figure 4.1B), and uses only one angle: $\psi = arcsin(\alpha_K) = arccos(\beta_K)$, to project the orientation of the grating vector to the laboratory y-axis. The diffracted direction projections α_p, β_p all lie along a straight line, are evenly spaced, and their in-line separations remain shift-invariant with respect to the incidence angle for both reflection and transmission conditions. The position of the zeroth-order remains unchanged unless the angle of incidence is varied. If the grating vector is rotated around the grating surface normal, the circular latitude arc intersection will pivot around the incidence (**I**) projection line to the $\alpha\beta$-plane. The angular configuration space facilitates the calculation of the DO deflection in real space for the tiled grating pattern which is proposed following.

The multiplexed crossed-cell-tile grating device consists of alternating tiles of two $1^{st}-$order transmission phase-gratings, independently optimized to perform under oblique incidence, arranged in orthogonal directions on a rectangular grid on the sub-

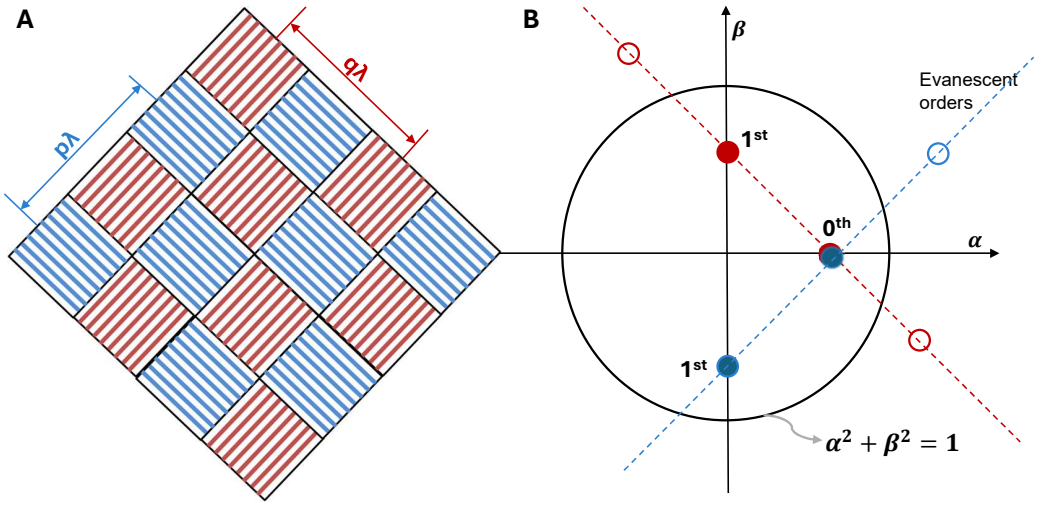

Figure 4.2: A) Crossed-cell-tile grating device with two $1^{st}-$order gratings G1 and G2 (blue and red respectively) tiled in an alternating orthogonal pattern. Similar grating tiles are placed at a center-to-center distance of integer multiples (p, q) of the incident wavelength value. B) The $\alpha\beta$-plane in direction-cosine space for the tiled pattern, separating the $1^{st}-$DO shown as red and blue dots and the overlapping $0^{th}-$DO. The empty bullets outside the unit circle are evanescent higher-DO.

strate surface. The grid layout is shown in Figure 4.2A. Following the discussions above and Section 1.4, the desired $\alpha\beta$-plane projections are shown in Figure 4.2B, with the corresponding color-code for the grating tile orientations. The gratings are to be designed to propagate only the $0^{th}-$ and $1^{st}-$orders, under conical incidence conditions that will produce their respective $0^{th}-$DO to overlap in direction, and their $1^{st}-$DO to distribute in orthogonal angular directions. Note that the $0^{th}-$order overlap in direction-cosine space is also the direction of incidence to the device surface, and each of the grating tiles and the alternating tile grating vectors are oriented perpendicular to one-another. This arrangement requires establishment of the incidence direction with respect to the grating plane normal and grating vector $(\alpha_i, \beta_i, \gamma_i$ and $\alpha_K, \beta_K)$ for one of the grating tiles, followed only by a $\pi/2$ rotation of the grating vector around the surface normal for the other (crossed) tile. The angular separation between the diffraction orders depends on the period of the gratings and

could be designed different for the red and blue tile gratings. In Figure 4.2A each grating tile of the same type (blue or red) are spaced by an integral multiple of wavelengths ($q\lambda$ or $p\lambda$) parallel to their respective grating vector. This implies that the real-space lateral separation between the periodic tiles of the same type will induce a diffraction field transverse 2π phase-shift in Fourier space, and as a consequence the directed diffraction orders will constructively interfere in the far-field. The size of the individual tiles for either grating should contain a number of grating periods to result in a well-defined DO line shape. The device should operate with the incident beam illuminating multiple crossed-tiles at once.

An advantage of this device design is that the two types of cross-tiled gratings can be optimized independently of each other, for orthogonal polarization incident states, to manipulate the efficiencies of the four propagating desired orders. The optimization process consists of fill-factor and depth adjustments for the blue grating tile (G1) and the red grating tile (G2), to achieve a highly efficient $1^{st}-$order (more than 90%) and a highly suppressed $0^{th}-$order (less than 1%). These conditions will result in a two-way beam splitter using the two $1^{st}-$orders. Accounting for reflective losses, the total transmitted light could be divided in ratios of 1:47:47 respectively along the 0^{th}, 1^{st}_{G1} and 1^{st}_{G2} orders. The device can be used for unpolarized incident light, as each tiled grating set will diffract an orthogonal polarization state. A similar approach can also be used to create a three-way beam splitter, by splitting the efficiencies of $1^{st}-$ and $0^{th}-$DO of each crossed grating tile in a 2:1 ratio. Note that the $0^{th}-$order of both crossed tiles overlap in space and thus the total light will be split equally among the three spots in ratios of 1:1:1. The range of optimized grating structural parameters, to achieve the DO efficiencies in the desired proportions mentioned above, are discussed in Section 4.3 below.

4.3 First-order grating cell design

To compute the DO efficiencies from each grating cell (G1,G2) based on the grating structure parameters, it is necessary to rigorously solve Maxwell's equations for the electromagnetic fields within the grating, since the desired grating designs have sub-wavelength periodicity. There are several conventional numerical methods to compute the power in each propagating diffracted order such as the Finite-Difference Time Domain (FTDT) [21], the Fourier Modal Method (FMM) [22], and the Rigorous Coupled Wave Analysis method (RCWA)[23]. Although these methods are accurate when all grating parameters are specified, they are not suitable for solving the inverse diffraction problem, i.e., to determine the grating parameters when the efficiencies are specified. This necessitates inversion of the rigorous vector analysis and may not yield unique solutions. The Simplified Modal Method (SMM) was used to determine the range of structural parameter solutions for the desired grating cells, which is briefly presented below for completeness. The SMM has been applied to designs of simple binary phase gratings[24, 25] and slanted gratings[26], to determine the ranges of the periodic fill-factors and phase depth values for pre-specified performance. However, it has been limited to cases under PPI conditions, where the electric or magnetic fields are perpendicular to the transverse cross section of the grating. To the best of our knowledge, there is no literature references on the application of the Simplified Modal Method to oblique angles of incidence, as illustrated in the inset in Figure 4.1A, where the polarizations are not perpendicular to the grating plane structural cross section.

Thorough analysis of the scattering phenomenon involving a uniform plane wave interacting with a dielectric grating, as illustrated in the inset in Figure 4.1A, has been reported by S.T. Peng[27]. The study addressed the general case where light is incident at an oblique angle (θ_i, φ_i) on a binary grating with period Λ. For PPI conditions the general SMM approach computes the field inside the grating region from an

eigenvalue equation, where the eigenmodes have to satisfy continuity conditions and pseudo-periodicity conditions at the grating walls[28]. Peng's approach involved a significant refinement: he rotated the coordinate system to encompass both TE and TM modes simultaneously within the context of a three-dimensional vector boundary-value problem, contrasting with the conventional two-dimensional boundary-value problem where TE and TM waves are treated separately. His methodology involves formulating a transfer matrix for the electric and magnetic fields along one unit cell of the grating, using the boundary conditions at the ridges and grooves of the grating. The condition that after diagonalizing the matrix, the sum of eigenvalues are the trace of the matrix, results in a set of characteristic equations. A simplified version of the set of the characteristic equations $F_{pol}(n_{eff})$ is:

$$F_{TE}(n_{eff}) = cos\,\kappa\Lambda = cos(k_1 d_1)cos(k_2 d_2) - \frac{(k_1^2 + k_2^2)}{2k_1 k_2} sin(k_1 d_1)sin(k_2 d_2) \tag{4.1}$$

$$F_{TM}(n_{eff}) = cos\,\kappa\Lambda = cos(k_1 d_1)cos(k_2 d_2) - \frac{(n_2^4 k_1^2 + n_1^4 k_2^2)}{2n_1^2 n_2^2 k_1 k_2} sin(k_1 d_1)sin(k_2 d_2) \tag{4.2}$$

where,

$$\kappa = k_0 sin(\theta_i)cos(\varphi_i) + \frac{2m\pi}{\Lambda} \tag{4.3}$$

$$k_1 = k_0\sqrt{(n_1^2 - n_{eff}^2)} \tag{4.4}$$

$$k_2 = k_0\sqrt{(n_2^2 - n_{eff}^2)} \tag{4.5}$$

Here the numbered subscripts indicate the ridge (1-dielectric) and groove (2-air) regions of the grating cell, d and n are the width and optical index of each region respectively, and k_0 is the incidence medium wavenumber. The term κ represents the propagation of the $m^{th}-$Floquet vector along the transverse direction within the grating region, and it simplifies to the left-hand side term of equations 4.3, because

the cosine function repeats every integral multiple of 2π. In equations 4.1 and 4.2, d_1 and d_2 can be expressed in terms of the fill factor. The effective optical index of the grating region (n_{eff}) is the only unknown variable in the set of equations. Solving the equations for n_{eff} satisfying the equality with known θ_i, φ_i, n_1, n_2, and Λ, can optimize the fill factor for a specific wavelength of operation. In our design we used a fused silica ($n_1 = 1.47$) binary grating with period of 604 nm, to operate at a wavelength of 604 nm. The values of $F(n_{eff})$, plotted as a surface function of n_{eff} and the normalized fill factor d_1/Λ, for both TE and TM polarizations, are shown as the respective curved surfaces in figures 4.3A and 4.3B. The $cos(\kappa\Lambda)$ in equations 4.1 and 4.2 depends on the AOI and the normalized ratio λ/Λ determined in the previous section, but is independent of d_1 and n_{eff} and is depicted as an intersecting plane in the same space (in blue). The intersection between the surface and the plane generates the line paths shown by the black traces. We note that for almost all values of the fill factor fraction d_1/Λ there are two solutions of n_{eff} along the intersection path, corresponding to the two propagating DO (0^{th},1^{st}). Figure 4.4 shows the TE and TM polarization intersection paths on the effective index normalized fill factor plane. Possible negative solutions of n_{eff} correspond to evanescent DO and are of no consequence. The SMM parameter determination procedure is applied to the design for each crossed-cell-tile grating G1 and G2.

The difference of the DO effective index solutions (Δn_{eff}) for each polarization state is plotted as a function of the fill factor d_1/Λ in Figure 4.5. Clausnitzer points out that when the SMM is applied to a binary grating the diffraction process is comparable to the operation by a Mach-Zehnder interferometer[24]. In this analogy, the incident light is divided equally between the 0^{th} and 1^{st} orders, each propagating through media with different effective indices ($n_{eff}^{(0)}$ and $n_{eff}^{(1)}$). The intensity distribution between the orders, after it exits the grating medium, is governed by the optical path difference: $\Delta s = (n_{eff}^{(0)} - n_{eff}^{(1)})h$. When the grating depth h is zero, the phase difference between

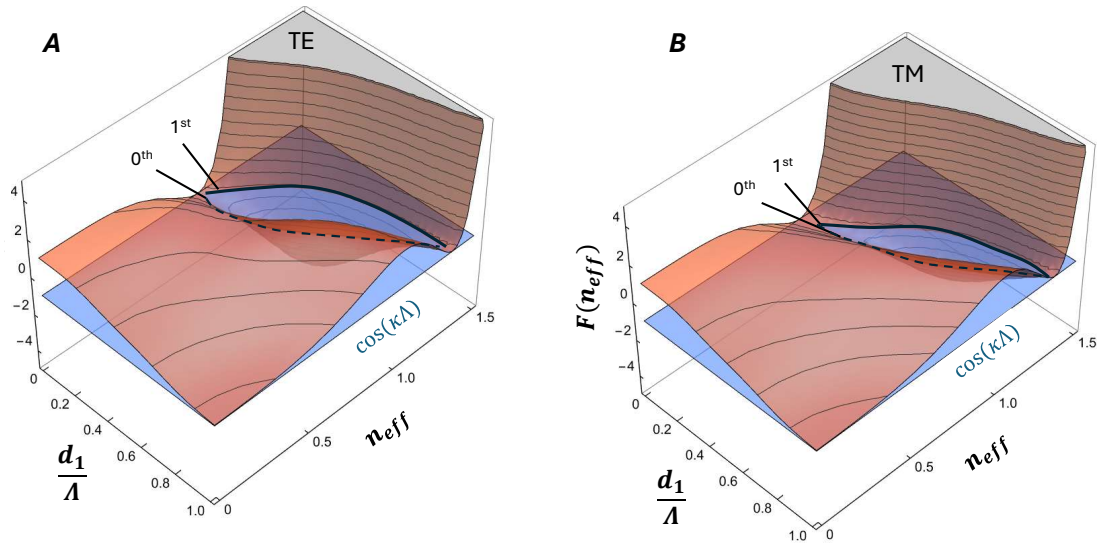

Figure 4.3: Surface contour plots of $F(n_{eff})$ in amber, and the plane $cos(\kappa\Lambda)$ in blue, for the grating cell design G1, from equations **??** as a function of the effective refractive index n_{eff} and normalized fill factor d_1/Λ, for: A) TE polarization and, B) TM polarization. The solid black lines represent the $1^{st}-$DO solutions and the dotted black lines are for the $0^{th}-$DO solutions satisfying the AOI and periodicity from section 4.2.

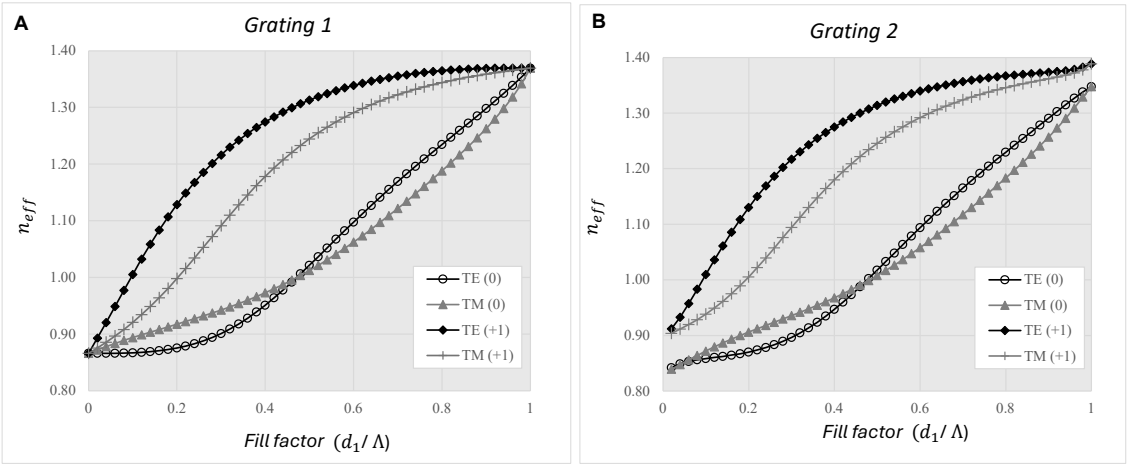

Figure 4.4: Effective refractive index, n_{eff} as a function of the grating period-normalized fill factor, for: A) Grating G1 and B) Grating G2. The four different curves correspond to the TE and TM polarizations of the $0^{th}-$ and $1^{st}-$DO.

the DO is also zero, resulting in all of the light propagating through the $0^{th}-$order only. As the depth of the grating increases, the efficiency shifts from the 0^{th} to the $1^{st}-$DO. For the phase difference equal to an odd multiple of π, all the light is diffracted into the $1^{st}-$order. This is shown in equation 4.6 where $\Delta\psi$ is the phase difference between the DO:

$$\Delta\psi = \frac{2\pi}{\lambda}|\Delta s| = \frac{2\pi}{\lambda}\Delta n_{eff} h = (2m-1)\pi, \quad m = 1, 2, 3.... \tag{4.6}$$

The parametric dependence of Δn_{eff} to the fill factor d_1 is critical for the design optimization and is analyzed differently for a two-way and three-way grating beam splitter.

4.3.1 Two-way beam splitter grating cell-tiles

The objective of the two-way beam splitter grating design is to achieve efficient beam splitting of unpolarized light into a distribution ratio of 1:47:47 across the 0^{th}, 1^{st}_{G1} and 1^{st}_{G2} orders, as outlined in Section 4.2. To accomplish this, the period and fill factor of both gratings G1 and G2, were further optimized to maximize the first-order diffraction efficiency for both TE and TM polarizations. For effective first-order diffraction, the period of the gratings was set to match the operational wavelength of the laser at 604 nm.

The diffracted intensity distribution optimization included considerations of the experimental testing apparatus. For instance, to achieve oblique incidence the device is rotated with respect to the laboratory y-axis, followed by a rotation around the resulting x'-axis. For the two-way beam splitter device, this involves sequential rotations of 30° (y-axis), followed by a 40° (x'-axis). The incident directions in spherical-polar coordinates with respect to the grating normal (θ_i, φ_i) for both gratings were determined using coordinate rotation matrices, yielding respectively $\theta_{i1} = 48°$ and $\varphi_{i1} = 48°$ for G1, and $\theta_{i2} = 48°$ and $\varphi_{i2} = -42°$ for G2.

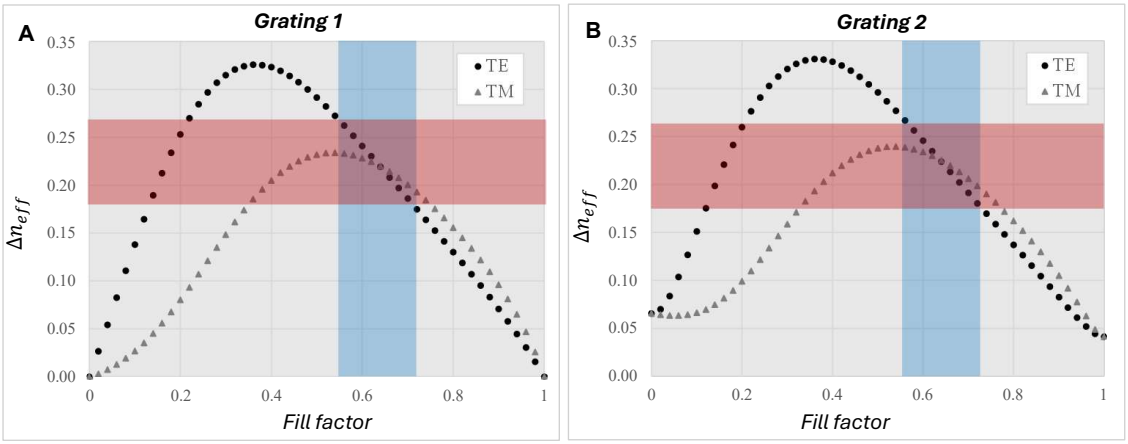

Figure 4.5: The difference in the effective refractive index, Δn_{eff}, between the 0^{th} and $1^{st}-$ DO as a function of the normalized fill factor d_1/Λ, for: A) cell G1 and B) cell G2, from the values in figure 4.4. The range of Δn_{eff} values where the TE and TM curves are nearly overlapping (red highlight) corresponds to the range of optimum fill factor values (blue highlight).

In figures 4.5A and 4.5B, the blue-shaded region indicates the optimal range of fill factor values where the TE and TM curves nearly overlap, which is crucial to achieve polarization insensitivity for the two-way grating beam splitter. The red-shaded region indicates the corresponding range of Δn_{eff}, from which the optimal grating depth range h can be calculated using Equation 4.6. Typically, the parameter m in Equation 4.6 is set to 1 to maintain a shallow grating profile, which is preferred due to fabrication challenges associated with high aspect ratio gratings. Consequently, for the two-way beam splitter device, the optimal depth and fill factor of both grating types is required to be within the range of 1.11 μm to 1.57 μm and 0.55-0.70 respectively.

Rigorous Coupled-Wave Analysis (RCWA) simulations were executed to assess the $1^{st}-$DO power efficiencies (η_{+1}) within the range of fill factors and depths specified above, for both TE and TM polarizations, as presented in figure 4.6 for both grating types. The optimal performance, achieving over 90% efficiency in the $1^{st}-$DO, on all

four cases was selected at a fill factor of 0.56 and a grating depth of 1.15 μm, indicated by the red dotted lines in figure 4.6. These values fall within the ranges predicted by the Simplified Mode Method. This demonstrates the reliability of the SMM technique employed here to generate solutions to the inverse diffraction problem under oblique incidence conditions.

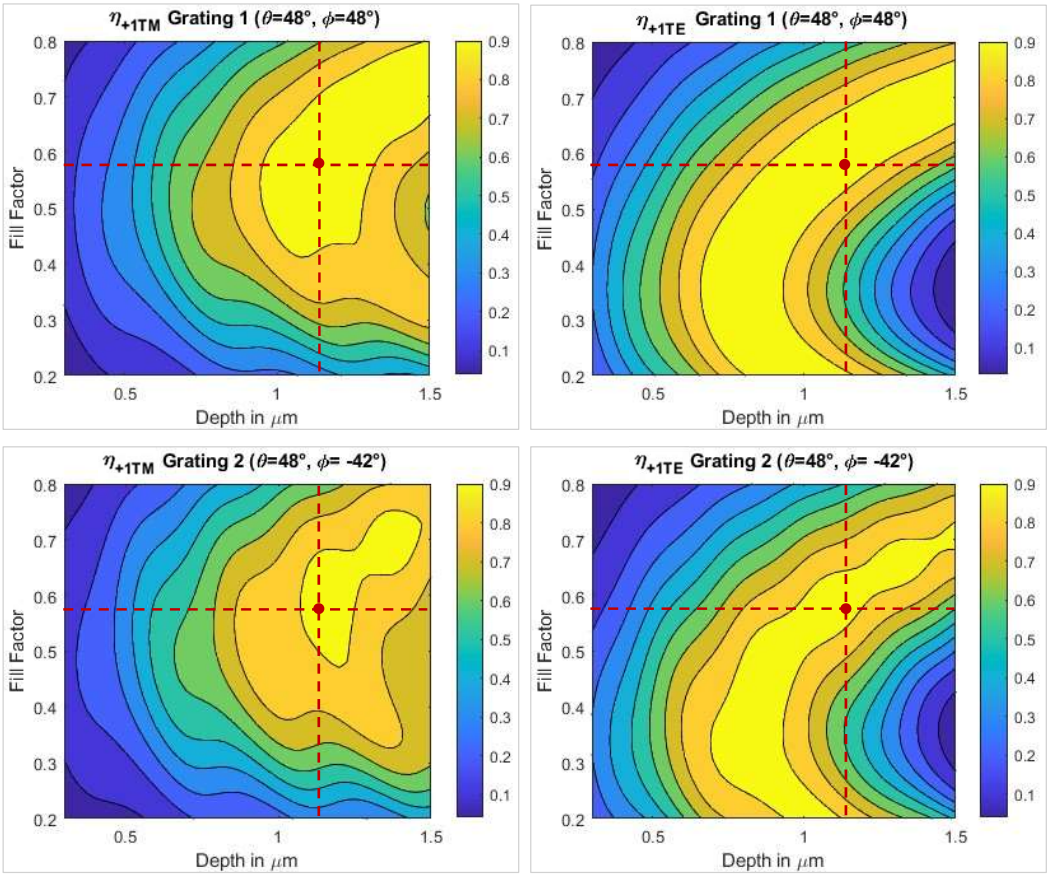

Figure 4.6: RCWA computed diffraction efficiency contour plots of the $1^{st}-$DO (η_{+1}) as a function of depth and fill factor, for TM and TE polarization (left and right columns) of grating G1 and grating G2 (top and bottom rows), for the two-way crossed-cell-grating beam splitter. The red dot represents the chosen common depth (1.15μm) and fill factor (0.56) on all four graphs, that yield diffraction efficiencies η_{+1} >90%.

4.3.2 Three-way beam splitter grating cell-tiles

The objective of the design for the three-way crossed-cell-tile grating beam splitter is to achieve light distribution with 66% of the incident power directed into the

$1^{st}-$DO and 33% into the $0^{th}-$DO, for each grating cell G1 and G2. Key grating parameter values, such as the period Λ, the fill factor d_1, the incidence directions θ_i and φ_i, were specified equal to the ones used for the two-way beam splitter design, with the grating cell depths h alone as the optimization variables. As a result, the Δn_{eff} as a function of fill factor is the same (figure 4.5), except that the desired fill factor range (blue highlight) is chosen between 0.46 and 0.66, yielding different ranges for Δn_{eff}. Optimizing the grating depth to achieve 66% efficiency in the $1^{st}-$DO using the SMM is challenging, because the relationship between η_1 and Δn_{eff} is not well-defined. According to Clausnitzer[24], the efficiency of the $1^{st}-$DO follows a sine-function dependence as the phase difference increases from 0 (minima) to π (maxima). Given that the primary use of the simplified mode method is to identify the ranges of the grating parameters rather than their exact values, we approximated the efficiency as quasi-linear with respect to the phase difference, which is a reasonable approximation of sinusoidal behavior for values of the phase difference near $\pi/2$. Under this assumption, the phase difference in Equation 4.6 was set to 0.66π, to achieve 66% diffraction efficiency in the $1^{st}-$order. The modified Δn_{eff} range values yielded an optimum depth range between 640 nm and 960 nm for the three way beam splitter device. The 1^{st} order transmission efficiency (η_{+1}) was subsequently simulated using RCWA for variable grating depth values (h), and the results are presented in figure 4.7, with the values of $0.50 < \eta_{+1} < 0.75$ shown in more detail. The mean polarization state transmission efficiency value is 0.65, for a depth of 650 nm which is within the depth range predicted by SMM. The rigorous simulations for grating groove-depths of 650 nm show that our assumption of linear dependence for η_{+1} as a function of the DO phase differences ($\Delta\psi$) is slightly off-target. The efficiency η_{+1} averages 0.66 for phase difference values below 0.66π. The rigorous simulation values for η_0 and η_{+1} for both grating cells and incidence polarizations are listed in table 4.1.

Table 4.1: RCWA-simulated diffraction efficiencies of the 0^{th} (η_0) and $1^{st}-$DO (η_{+1}) at a grating depth of 650 nm, for both the grating cells (G1, G2) of the three-way beam splitter device.

	η_{+1}	η_0
G1 (TM)	0.601	0.345
G1 (TE)	0.693	0.280
G2 (TM)	0.572	0.390
G2 (TE)	0.638	0.331

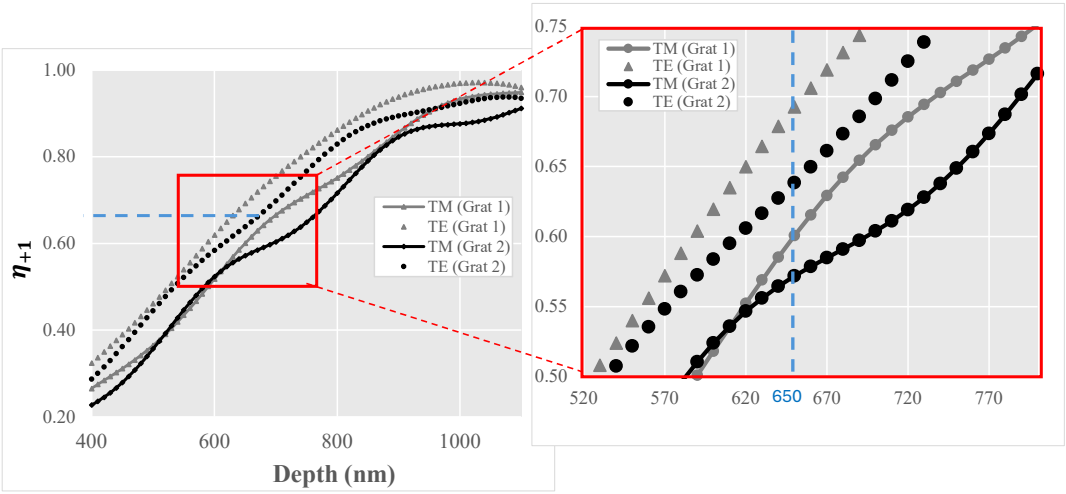

Figure 4.7: RCWA computed transmission diffraction efficiency for the $1^{st}-$DO as a function of grating depth, for both gratings G1, G2, and both incident polarizations. Right: Expanded view of the efficiency range: $0.50 < \eta_{+1} < 0.75$. At depth 650 nm, shown by the vertical dotted line, the efficiencies are within the desired range of 0.58-0.69.

4.4 Fabrication and test of crossed-cell-tile grating beam splitters

4.4.1 Fabrication of crossed-cell-tile devices

Fabrication of the crossed-cell-tile devices were using the e-beam lithography technique as detailed in Section 1.2.2 involving two major processing steps . A standard 6×6 inch square, quarter-inch thick quartz was used as the substrate and an electron-beam compatible polymethyl methacrylate (PMMA) was used as the photoresist. The crossed-cell-tile grating patterns designed in sections 4.2 and 4.3 are written into

the photoresist using the electron beam exposure tool. The photomask substrate was diced using a diamond blade dicing saw into eight blocks, each measuring 38×38 mm^2, with the device pattern occupying the central of 4×4 mm^2 area. Among these blocks, four contained the actual pattern made of crossed and tiled grating cells with a 604 nm period and a 0.56 fill factor, as shown in Figure 4.2. The other four blocks were not cross-tiled and serve as grating G1 and G2 proxies. Each proxy block then undergoes a reactive-ion plasma etch process using a PlasmaTherm RIE7000 tool, with methyl-trifluoride (CHF_3) as the reactive gas under a RF power supply of 1000 W. Once the target depth is achieved using the proxies, the crossed-cell tiles are etched using the optimized process parameters.

4.4.2 Performance of three-dimensional beam splitter devices

To monitor the etch depth of the process, the transmission spectrum of the $0^{th}-$DO of the proxy grating cells is measured in the 300-1000 nm wavelength range, with 1 nm resolution at normal incidence, using the WVASE discussed in Section 3.1.3. The measured spectrum is then compared to simulations of variable depths of the proxy grating to find the best fit. Functional testing of the crossed-cell-tile devices was performed using the setup shown in figure 4.8A, illuminating the sample at the design oblique incidence conditions with a polarized tunable He:Ne laser source (REO Inc., Model No:30602). The source operates at around 604 nm and can be tuned to produce five lasing lines between 543 nm and 633 nm. The oblique angle of incidence is achieved by mounting the device block on a rotating holder that can rotate along the $y-$ and $x'-$axes. A linear polarizer (LP) and a half-wave-plate (HWP) are used to control the incident light polarization state between 0° (TM), 30°, 45°, 60° and 90° (TE). A second linear polarizer is used as an analyzer (LA) to measure the polarization state before the detector. The beam-splitter DO measured data is normalized with the baseline power of the laser, measured with the test device absent. Figure 4.8B is a photograph of the three prominent DO from the three-way beam splitting device on

a square-grid paper screen, indicating that the 1^{st}_{G1} and $1^{st}_{G2}-$DO are equidistant from the overlapping $0^{th}-$DO, arranged on two separate orthogonal planes. The intensities of the DO are measured by placing a photodiode detector along the corresponding diffracted angle directions. Measurements are collected for various input polarization states.

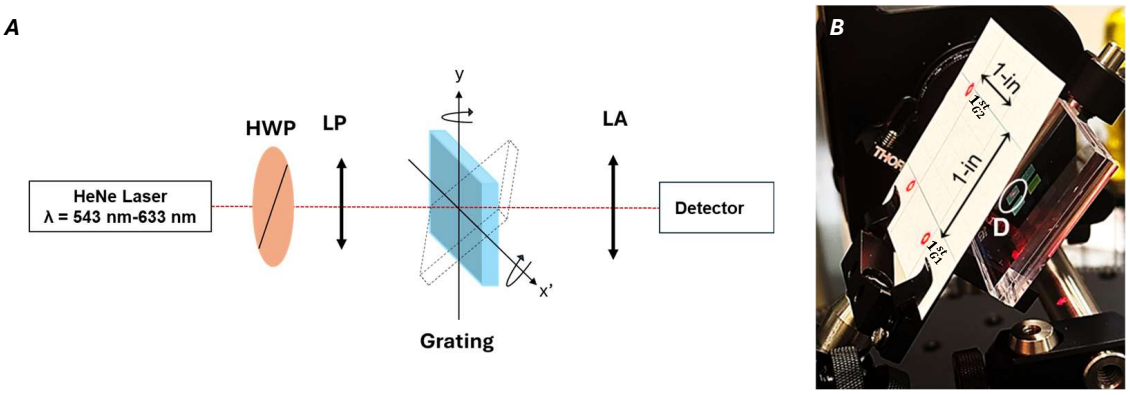

Figure 4.8: A) Schematic of the test setup used for oblique angle of incidence. HWP is the half-wave plate, LP is the linear polarizer, and LA is the linear polarization analyzer. B) Photograph of the three-way beam splitter device block (D), tested at 633 nm. The projection of the three DO after conical diffraction is shown on a square-grid paper card. The 1-in. grid divisions on the card are visible for location comparison.

The two-way beam splitter device was etched to a depth of 1.13 μm, confirmed by the transmission measurements from WVASE. This matched with the design depth of 1.15 μm within a -1.9% fractional deviation. The measured and simulated efficiencies of the four DO for this device, at an incident wavelength of 604 nm and five different input polarizations states including TE and TM, are listed in Table 4.2A. The table includes the fractional deviation of the measured from the simulated efficiencies. The $0^{th}-$DO spots coincide, forming only three spots in space. From the measurements, the $0^{th}-$DO is well suppressed, while the first orders are highly efficient reaching a split ratio of $\eta_0^{(G1+G2)} : \eta_{+1}^{(G1)} : \eta_{+1}^{(G2)} = 0.026{:}0.463{:}0.460$, averaged across the five input polarization angles. The measured efficiencies agree well with the simulated data with

deviations within ±1.9% as evident from the table.

The three-way beam splitter was over etched during the process, reaching a device depth of 680 nm, confirmed by the WVASE measurements. This is a deviation of +4.6% from the design depth of 650 nm, which induces a phase difference beyond 0.66π for the design wavelength of 604 nm. However, for an incident wavelength of 633 nm the phase difference condition is satisfied. The measured, simulated, and fractional deviation efficiencies, for the three-way beam splitter at 633 nm wavelength are listed in table 4.2B. An average split ratio of $\eta_0^{(G1+G2)} : \eta_{+1}^{(G1)} : \eta_{+1}^{(G2)} = 0.313{:}0.309{:}0.307$ was measured for the five polarization input states. Although the simulated data split ratios across the TE and TM polarization deviate as from the curves shown in figure 4.7, the measured efficiencies were consistent in achieving split ratios close to 1:1:1. The fractional average deviations of the measured and simulated efficiencies are within 6%.

Table 4.2: Efficiencies of the DO from both beam splitter devices.

(a) Two-way beam splitter tested at 604 nm wavelength

	Measured			Simulated			Deviation		
Input Pol	η_0	$\eta_{+1}^{(G1)}$	$\eta_{+1}^{(G2)}$	η_0	$\eta_{+1}^{(G1)}$	$\eta_{+1}^{(G2)}$	η_0	$\eta_{+1}^{(G1)}$	$\eta_{+1}^{(G2)}$
0° (TM)	0.021	0.464	0.461	0.025	0.476	0.463	0.004	0.012	0.002
30°	0.031	0.468	0.457	0.016	0.465	0.462	-0.015	-0.004	0.005
45°	0.029	0.464	0.460	0.020	0.461	0.462	-0.009	-0.003	0.002
60°	0.028	0.461	0.458	0.029	0.464	0.462	0.001	0.003	0.004
90° (TE)	0.023	0.459	0.465	0.042	0.474	0.462	0.019	0.015	-0.003

(b) Three-way beam splitter tested at 633 nm wavelength

	Measured			Simulated			Deviation		
Input Pol	η_0	$\eta_{+1}^{(G1)}$	$\eta_{+1}^{(G2)}$	η_0	$\eta_{+1}^{(G1)}$	$\eta_{+1}^{(G2)}$	η_0	$\eta_{+1}^{(G1)}$	$\eta_{+1}^{(G2)}$
0° (TM)	0.323	0.319	0.316	0.382	0.306	0.286	0.059	-0.013	-0.030
30°	0.326	0.313	0.317	0.367	0.283	0.274	0.041	-0.030	-0.043
45°	0.329	0.318	0.311	0.323	0.297	0.289	-0.006	-0.021	-0.022
60°	0.306	0.304	0.298	0.281	0.323	0.310	-0.025	0.019	0.012
90° (TE)	0.284	0.293	0.291	0.270	0.356	0.336	-0.014	0.063	0.045

The polarization angle of the diffracted beam was measured to be same as the input

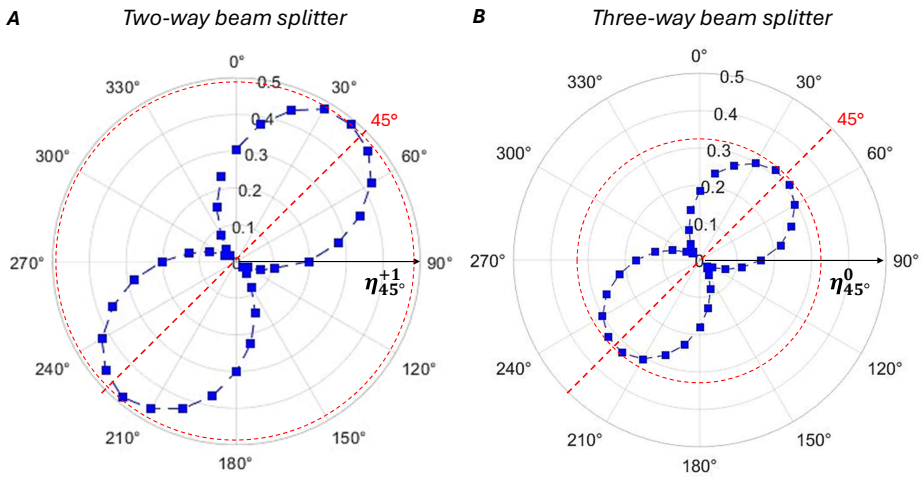

Figure 4.9: Detected polarization state polar plots of: A) the diffracted η_{+1} of the two-way beam splitter and, B) the η_0 of the three-way beam splitter, for a 360° rotation of the analyzer in steps of 10°. The red dotted lines show the alignment of the lobes to the incident polarization state, and the red dotted circles indicated the peak efficiency for each device. The maximum efficiency shown in the radial direction is 0.50.

polarization angle for both devices. As an example, for an input polarization state at 45° the polar plots of the $1^{st}-$DO for the two-way beam splitter and the $0^{th}-$DO for the three-way beam splitter are illustrated in figure 4.9A and 4.9B respectively. The analyzer was rotated 360° in steps of 10° to collect the data shown. In both cases, the polarization lobes are aligned to 45° with the vertical, indicating that the incidence polarization is not changed by the devices. The three-way beam-splitter shows a small deviation due to differing TE and TM efficiency ratios after diffraction. There is no mixing of polarization states, as evidenced by the polar plot minima at 135° alignment of the analyzer. The efficiencies are indicated along the radial direction, peaking at 0.47 for the two-way beam splitter and 0.32 for the three-way beam splitter. The polarization angle of $1^{st}-$DO from G2, which has diffraction angles along a different plane for each device, could not be measured due to the mechanical positioning limitations of the experimental set up.

4.5 Conclusions

Two devices, consisting of alternating crossed-cell-tile first-order diffraction gratings, were designed and fabricated to function as two-way and three-way beam splitters for oblique incidence of unpolarized light. The designs feature alternating tiles of the same grating cells with their lines crossed to each other, effectively spatially separating the first diffraction orders of the two grating sets of cells in orthogonal planes, while the zeroth diffraction orders overlap axially. The ability to independently optimize each grating cell allows the beam splitter devices to separate light into designed ratios and directions. The design uses conical diffraction to separate the orders in different planes in space, which is desired for applications where optical paths along the same diffraction plane are component congested. The diffraction angles are predicted using Harvey's conical incidence model, expressed in terms of direction cosines in three dimensions.

To the best of our knowledge, the simplified modal method was used for the first time to optimize grating parameters at oblique angles of incidence. For the two-way beam splitter, the fill factor and depth of both grating cells were optimized for high throughput light efficiency, achieving over 90% in the first diffracted order and suppressing the zeroth order to less than 1% at a wavelength of 604 nm. The light beam splitting power distribution was designed to be 5%:93%:93% for the $0^{th} : 1^{st}_{G1} : 1^{st}_{G2}$ diffracted orders, projected as an isosceles triangular pattern in space with the $0^{th}-$order at the apex. For the three-way beam splitter, shallower grating depths were designed to distribute efficiencies between the first and zeroth diffracted orders at a 2:1 ratio, achieving an overall equal split of the incident intensity among the three diffracted spots at ratios of 1:1:1. The crossed-cell-tile pattern was fabricated on a quartz substrate using e-beam lithography, and etched to the designed depth with a plasma-assisted reactive-ion process. Testing the two-way beam splitter yielded light average power ratios of 2%:46%:46%, for five different incident polar-

ization states, including the TE and TM polarization at 604 nm wavelength. The three-way beam splitter yielded light ratios of 32%:32%:32% for incident TM polarization, and 28%:29%:29% for incident TE polarization at 633 nm wavelength, matching with rigorous numerical simulation expectations. Polarization sensitivity measurements showed that the input polarization states are preserved after diffraction through the devices. This polarization insensitivity is due to the individual cell-tile device optimization for both mutually orthogonal polarization states.

The crossed-cell-tile beam splitter devices are intended to use with unpolarized, incoherent polychromatic light, to direct fractions of the incident light power in three-dimensional directions in space. Applications that could benefit from the devices presented in this work include astronomical spectrographs and spectro-photometric instrumentation, which require high spectral efficiency and operate in the green-red part of the visible spectrum (500 nm to 670 nm.) Traditionally, astronomical instrumentation has large dimensional scales, recently however very compact designs have been implemented and tested, that make use of segmented field images into Arrayed Wide-Angle Camera Systems (AWACS)[29]. These recently developed instruments have considerable compaction and reduction in volume, and can benefit from three-dimensional beam splitter designs. Spectrographic optical element assembly could also be impacted by use of crossed-cell-tile beam splitter devices, as current spectral alignment procedures require use of linear gratings that are rotated by 90° in sequence to achieve mutual alignment. The three-way beam splitter presented here is capable of providing orthogonal-axes spectral alignment, based on the orientational distribution of diffracted spots shown in figure 4.2B, with a single procedural step.

REFERENCES

[1] Danae Delbeke, Roel Baets, and Peter Muys. Polarization-selective beam splitter based on a highly efficient simple binary diffraction grating. *Applied optics*, 43(33):6157–6165, 2004.

[2] Jiangjun Zheng, Changhe Zhou, Jijun Feng, and Bo Wang. Polarizing beam splitter of deep-etched triangular-groove fused-silica gratings. *Optics letters*, 33(14):1554–1556, 2008.

[3] Rong-Chung Tyan, Pang-Chen Sun, Axel Scherer, and Yeshayahu Fainman. Polarizing beam splitter based on the anisotropic spectral reflectivity characteristic of form-birefringent multilayer gratings. *Optics Letters*, 21(10):761–763, 1996.

[4] Junbo Feng and Zhiping Zhou. Polarization beam splitter using a binary blazed grating coupler. *Optics letters*, 32(12):1662–1664, 2007.

[5] Stephan Fahr, Tina Clausnitzer, Ernst-Bernhard Kley, and Andreas Tünnermann. Reflective diffractive beam splitter for laser interferometers. *Applied optics*, 46(24):6092–6095, 2007.

[6] Wenjing Fang, Xinye Fan, Xia Zhang, Huijuan Niu, Hengying Xu, Jiarui Fei, Yongqing Huang, and Chenglin Bai. Polarization-insensitive high-index contrast gratings beam splitter with focusing ability. *IEEE Photonics Technology Letters*, 30(8):708–711, 2018.

[7] Jijun Feng, Changhe Zhou, Jiangjun Zheng, Hongchao Cao, and Peng Lv. Design and fabrication of a polarization-independent two-port beam splitter. *Applied Optics*, 48(29):5636–5641, 2009.

[8] Junbo Yang and Zhiping Zhou. Double-structure, bidirectional and polarization-

independent subwavelength grating beam splitter. *Optics Communications*, 285(6):1494–1500, 2012.

[9] Jinbiao Xiao and Zhenzhao Guo. Ultracompact polarization-insensitive power splitter using subwavelength gratings. *IEEE Photonics Technology Letters*, 30(6):529–532, 2018.

[10] Wenhao Shu, Bo Wang, Hongtao Li, Liang Lei, Li Chen, and Jinyun Zhou. High-efficiency three-port beam splitter of reflection grating with a metal layer. *Superlattices and Microstructures*, 85:248–254, 2015.

[11] Jijun Feng, Changhe Zhou, Bo Wang, Jiangjun Zheng, Wei Jia, Hongchao Cao, and Peng Lv. Three-port beam splitter of a binary fused-silica grating. *Applied Optics*, 47(35):6638–6643, 2008.

[12] Christoph Braig, L Fritzsch, T Käsebier, E-B Kley, C Laubis, Ying Liu, F Scholze, and A Tünnermann. An euv beamsplitter based on conical grazing incidence diffraction. *Optics express*, 20(2):1825–1838, 2012.

[13] Liangliang Du, Limin Meng, Ran An, and Yan Ye. Tender x-ray beam splitting with high efficiency by use of multilayer grating based on conical diffraction. In *Second Target Recognition and Artificial Intelligence Summit Forum*, volume 11427, pages 498–503. SPIE, 2020.

[14] Martin Heusinger, Thomas Flügel-Paul, and Uwe-Detlef Zeitner. Large-scale segmentation errors in optical gratings and their unique effect onto optical scattering spectra. *Applied Physics B*, 122(8):222, 2016.

[15] Wiebke Freese, Thomas Kämpfe, Werner Rockstroh, Ernst-Bernhard Kley, and Andreas Tünnermann. Optimized electron beam writing strategy for fabricating computer-generated holograms based on an effective medium approach. *Optics express*, 19(9):8684–8692, 2011.

[16] Gerard de Zwart, Martin A van den Brink, Richard A George, Danu Satriasaputra, Jan Baselmans, H Butler, Jan BP van Schoot, and Jos de Klerk. Performance of a step-and-scan system for duv lithography. In *Optical Microlithography X*, volume 3051, pages 817–835. SPIE, 1997.

[17] Shahin Bagheri, Ksenia Weber, Timo Gissibl, Thomas Weiss, Frank Neubrech, and Harald Giessen. Fabrication of square-centimeter plasmonic nanoantenna arrays by femtosecond direct laser writing lithography: effects of collective excitations on seira enhancement. *ACS Photonics*, 2(6):779–786, 2015.

[18] Eric B Burgh, Matthew A Bershady, Kyle B Westfall, and Kenneth H Nordsieck. Recombination ghosts in littrow configuration: Implications for spectrographs using volume phase holographic gratings. *Publications of the Astronomical Society of the Pacific*, 119(859):1069, 2007.

[19] Panfilo C Deguzman, Yang Cao, Thomas J Suleski, Michael A Fiddy, Rich Jones, Robert TeKolste, and Jim Morris. Wafer-based diffractive polarizer design for low-reflectivity applications. *Optical Engineering*, 46(3):038001–038001, 2007.

[20] Fang Xu, Rong-Chung Tyan, Pang-Chen Sun, Yeshayahu Fainman, Chuan-Cheng Cheng, and Axel Scherer. Form-birefringent computer-generated holograms. *Optics letters*, 21(18):1513–1515, 1996.

[21] Hiroyuki Ichikawa. Electromagnetic analysis of diffraction gratings by the finite-difference time-domain method. *JOSA A*, 15(1):152–157, 1998.

[22] Lifeng Li. New formulation of the fourier modal method for crossed surface-relief gratings. *JOSA A*, 14(10):2758–2767, 1997.

[23] Elias N. Glytsis and Thomas K. Gaylord. Three-dimensional (vector) rigorous coupled-wave analysis of anisotropic grating diffraction. *J. Opt. Soc. Am. A*, 7(8):1399–1420, Aug 1990.

[24] Tina Clausnitzer, T Kämpfe, E-B Kley, A Tünnermann, Ulf Peschel, Alexandre V Tishchenko, and Olivier Parriaux. An intelligible explanation of highly-efficient diffraction in deep dielectric rectangular transmission gratings. *Optics Express*, 13(26):10448–10456, 2005.

[25] Yanan Wang, Zhiwen Chen, Keqiang Qiu, Zhengkun Liu, Yilin Hong, and Xiangdong Xu. High line density fused silica transmission gratings by deep reactive ion beam etching for ultra-short pulse laser compression. In *Second Target Recognition and Artificial Intelligence Summit Forum*, volume 11427, pages 438–445. SPIE, 2020.

[26] Shubin Li, Changhe Zhou, Hongchao Cao, and Jun Wu. Simple design of slanted grating with simplified modal method. *Optics Letters*, 39(4):781–784, 2014.

[27] ST Peng. Rigorous formulation of scattering and guidance by dielectric grating waveguides: general case of oblique incidence. *JOSA A*, 6(12):1869–1883, 1989.

[28] IC Botten, MS Craig, RC McPhedran, JL Adams, and JlR Andrewartha. The dielectric lamellar diffraction grating. *Optica Acta: International Journal of Optics*, 28(3):413–428, 1981.

[29] Hanshin Lee, John M. Good, Brian L. Vattiat, and Gary J. Hill. Arrayed wide-angle camera system for the Extremely Large Telescopes. In Christopher J. Evans, Luc Simard, and Hideki Takami, editors, *Ground-based and Airborne Instrumentation for Astronomy VII*, volume 10702, page 107021Z. International Society for Optics and Photonics, SPIE, 2018.

CHAPTER 5: SUMMARY AND OUTLOOK

First-order diffraction gratings are essential in spectrograph units of telescopes, as the spatially dispersed first orders are used for spectroscopic measurements. In astronomy, there is an increasing need to observe fainter celestial objects, creating a demand for highly efficient optical components in telescopes. Our contributions addressed two key areas: fabricating random anti-reflective surface structures to improve the anti-reflective treatment for optical elements within the telescope unit, and developing highly efficient designs of first-order transmission gratings for the spectrograph unit. Photolithography was utilized for the fabrication of both the ordered structures (micro gratings) and the disordered structures (random nanostructures). The rARSS was adopted as an antireflection treatment on the backside of the RIPLE grating to mitigate recombination ghost orders associated with Littrow orientation of the grating. Additionally, a crossed-cell grating device was fabricated using photolithography to function as a two-way and three-way beam splitter in the visible regime.

In chapter 2, the random antireflective surface structures (rARSS) fabricated on a set of fused silica cylindrical lenses and freeform elements were investigated. The spectral transmission was featureless and reached values above 98% for a spectral band from 400 nm to 800 nm wavelength meeting the system unit requirements. The maximum transmission reached 99% for a smaller spectral band of width 40nm centered around 470 nm for the cylindrical lens and a bandwidth of 100 nm centered around 540 nm for the freeform components. The difference in performance for the two types of optical elements is due to differences in their physical dimensions, that affect the etch rate during fabrication. The wavefront measurements emerging

from the cylindrical lens before and after rARSS fabrication revealed no significant wavefront distortion imparted by the process. Complete-angle directional transmission scatter measurements, at selected locations of the freeform component, show a difference of six orders-of-magnitude in transmission intensity between specular and off-specular angles indicating low wide angle scatter. Compared to conventional thin film coated components, the rARSS components showed higher transmission particularly near shorter wavelengths when tested using a single unit of the arrayed wide-field astronomical camera system (AWACS) unit at McDonald Observatory.

In Chapter 3, a highly efficient first order transmission grating operated at Bragg incidence was successfully fabricated as a proof of concept (POC) using the reactive ion plasma etching (RIPLE) technique. The 0^{th} order efficiency was suppressed to less than 1% while the $1st$ order efficiency reached 90% for wavelengths in 650 nm range for incident u polarized light. The back of the substrate was treated with rARSS structures to minimize the Littrow recombination ghost intensities. Complete angle scatter measurements at near Littrow (Bragg) incidence was done to map the positions and intensities of the ghost orders revealing a difference of 4 orders of magnitude between the highly efficient 1^{st} order and the ghost orders. To realize the 101.6×101.6 mm^2 target grating for the telescope from the 25.4×25.4 mm^2 proof concept grating, an area scaling was done which was crucial since the clear aperture of the telescope can go beyond 4 inches. The fabrication challenge of early chrome exhaustion associated with high aspect ratio gratings was overcome using an iterative chrome redeposition technique. With three iterations of the chrome redeposition technique we successfully fabricated 1.4 μm deep target grating that was tested to reach first order efficiencies of 90% at Bragg incidence and 94.5% at slightly off Bragg incidence. The results out performs the conventional Volume Holograph gratings (VHG) used at MCDonald observatory.

In Chapter 4, the crossed-cell-tile grating device featuring two alternate first-order

diffraction gratings tiled perpendicular to one another, was successfully fabricated to function as both a two-way and three-way beam splitter at oblique angles of incidence. There were four propagating orders emerging from the device; the two firsts orders lying in separate orthogonal planes and the two zeroth orders that overlapped in space, creating three main light-splitting pathways arranged as the apexes of an isosceles right triangle. The fill factor and depth of each grating type was optimized to split light in the 1^{st} and 0^{th} order in the ratio 96:1 and 2:1 for the two-way and three-way beam splitter respectively. This results in an equal split of the total light among three orders for the 3-way beam splitter and among the two first orders in case of 2-way a beam splitter. Testing of the devices at five different input polarization angles, yield a light-split ratio of approximately $\eta^0 : \eta_{G1}^{+1} : \eta_{G2}^{+1}$= 2%:46%:46% for the two-way beamsplitter at 604 nm wavelength and 32%:32%:32% for the three-way beamsplitter at 633 nm wavelength. The polarization angle of the incident beam was preserved after diffraction making the device insensitive to polarization.

In summary, the studies conducted in this dissertation were a part of ongoing projects with direct application in the field of astronomy. These results pave the way for future innovations. The current crossed cell tile grating device, due to its versatility in the design, can be tailored for specific applications such as polarization beam splitters. Polarization beam splitters (PBS), that splits incident beam into two cross-linear polarized light beams, are applicable in many areas like laser systems for polarization control, optical communication to manage signals with different polarization, imaging system for polarization based image separation etc. An example of the design of PBS for 604 nm wavelength is briefly discussed in Section 5.1.

5.1 Future work : Polarization beam splitter design

The advantage of the crossed-cell tile device that the two types of grating can be designed independent of each other, as discussed in Section 4.3, will be exploited in this section to design a polarization beam splitter that separates out TE and TM in

the first orders of the grating leaving the 0^{th} order unpolarized.

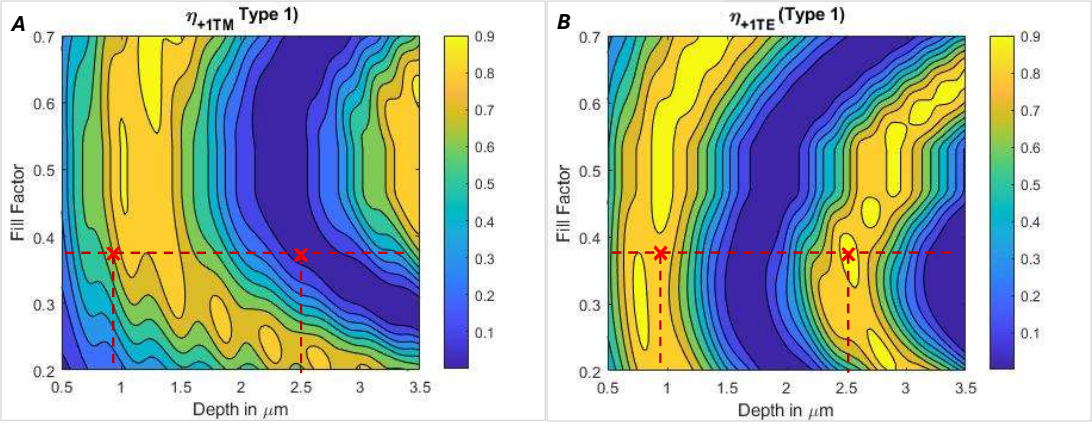

Figure 5.1: RCWA simulated efficiency contours of the 1^{st}-DO (η_{+1}) as a function of depth and fill factor for: A) grating G1 at TE polarization and, B) TM polarization.

A crossed-cell pattern, where both gratings have a period of 650 nm, is optimized to behave as a polarization beam splitter, at an operating wavelength of 604 nm. For oblique incidence, the y-axis is rotated by 28°, followed by an x′-axis rotation of 32°. Notably, this sequence of rotations results in identical values of θ and φ for both grating types, set at 42° and 45° respectively. As a consequence, the Δn_{eff} as a function of the fill factor is identical for both grating types and resembles the graph shown in Figure 4.5. In this configuration, Grating 1 is optimized for TE polarization, where 95% of TE-polarized light is directed to the 1st order, while Grating 2 is similarly optimized for TM polarization. Due to orthogonal alignment, the TE polarization incident on Grating 1 is equivalent to the TM polarization incident on Grating 2. This simplifies the design process, as optimizing Grating 1 for TE polarization automatically optimizes Grating 2 for TM polarization. However, it's important to note that this alignment is effective only because the θ and φ values are identical for both grating types.

A fill factor is selected where TE and TM polarizations exhibit distinct Δn_{eff} val-

ues, in the Δn_{eff} vs fillfactor graph, to ensure polarization sensitivity. The optimum values of fill factor and depth was found to be 36% and 935 nm respectively. RCWA simulations at $(\theta, \varphi) = (42^{\circ}, 45^{\circ})$ are presented in Figures 5.1A and 5.1B for TE and TM polarizations, respectively. At a depth of 935 nm, the efficiencies of TE and TM polarization, although different, do not achieve the desired 95%-5% ratio, as marked by the red dotted vertical line on the left of both figures. However, setting m = 2 in Equation 4.6, corresponding to a phase difference of 3π instead of π, predicts a new depth within the range of 2.8 μm using SMM. This prediction is confirmed in RCWA simulations at a depth of 2.5 μm, as shown by red dotted vertical lines on the right of both figures, achieving efficiencies of TE and TM polarization in the desired 95%-5% ratio.

The development of the polarization beam splitter device is still underway. Fabricating high aspect ratio gratings presents significant challenges, particularly when cross-tiling. To address this, the redeposition of chromium technique outlined in Section 3.3 may be employed; however, it can only be applied to one tile orientation at a time, as the chromium metal tends to coat grooves aligned with the sputtering direction. If this approach proves successful, the results will be detailed in forthcoming journal publications

LIST OF OWN PUBLICATIONS

PEER REVIEWED TECHNICAL ARTICLES

1. V. P. Stinson, **U. Subash**, M. K. Poutous, and T. Hofmann, "Towards Two-Photon Polymerization-Compatible Diffractive Optics for Micro-Mechanical Applications," *Micromachines* **14**, 1319 (2023).

2. **U. Subash**, H. Lee, and M. K. Poutous, "High-efficiency anti-reflective modification of freeform elements and cylindrical lenses for arrayed wide-field astronomical corrector units," *Journal of Astronomical Telescopes, Instruments, and Systems* **10**, 025007 (2024). © SPIE.

3. **U. Subash** and M. K. Poutous, "Crossed-cell-tile multiplexed 1st-order gratings, for three-dimensional beam-splitter applications," *Optics Express* **32**, 38407–38421 (2024). © Optica Publishing Group.

CONFERENCE PROCEEDINGS

1. H. Lee, **U. Subash**, and M. K. Poutous, "Fabrication and evaluation of reactive ion-plasma etched astronomical diffraction grating with anti-reflective surface nanostructures," *Advances in Optical and Mechanical Technologies for Telescopes and Instrumentation V*, SPIE, 12188 (2022).

2. H. Lee, B. L. Vattiat,**U. Subash**, and M. K. Poutous, "Integration/test of dual unit arrayed wide-angle camera system and its evaluation in the context of extremely large telescopes," *Ground-based and Airborne Instrumentation for Astronomy IX*, SPIE, **2722–2738** 12184 (2022).

3. **U. Subash**, H. Lee, and M. K. Poutous, "UV to IR high-efficiency antireflective surface modification of freeform and cylindrical lenses for space

platform optical instrumentation," *UV/Optical/IR Space Telescopes and Instruments: Innovative Technologies and Concepts XI*, SPIE, 12676 (2023).

4. V. P. Stinson, **U. Subash**, M. K. Poutous, and T. Hofmann, "Mechanical Tuning of Diffractive Gratings Compatible with Two-Photon Polymerization," *2023 IEEE Research and Applications of Photonics in Defense Conference (RAPID)* **1**–**2**, IEEE, (2023).

5. V. P. Stinson, **U. Subash**, N. Shuchi, M. K. Poutous, and T. Hofmann, "Dynamic polarization and mechanical tuning of slanted wire diffraction gratings," *MOEMS and Minitiarized Systems XXIII* **12899**, SPIE, 1289902 (2024).

6. **U. Subash**, H. Lee, and M. K. Poutous, "Reduction of Littrow Recombination Ghosts in Astronomic Spectrograph 1^{st}-Order Transmission Gratings," *CLEO: Applications and Technology*, **ATh4E**–**1**, Optica Publishing Group, (2024).

7. V. P. Stinson, **U. Subash**, N. Shuchi, M. K. Poutous, and T. Hofmann, "Slanted Wire Diffraction Gratings Fabricated by Two-Photon Polymerization," *CLEO: Science and Innovations*, **SM1D**–**2**, Optica Publishing Group, (2024).

8. N. Shuchi, V. P. Stinson,**U. Subash**, M. K. Poutous, and T. Hofmann, "Mechanical Tuning of the Diffraction Efficiency of THz Slanted Wire Gratings,"*CLEO: Applications and Technology*, **JTu2A**–**58**, Optica Publishing Group, (2024).

9. Lee, H., **Subash, U.**, & Poutous, M. K., " Evaluation of Area Scaling of the Reactive Ion-plasma Etched Astronomical Diffraction Gratings,"*Advances in Optical and Mechanical Technologies for Telescopes and Instrumentation VI*, SPIE, **594**–**601** 13100 (2024).

10. Lee, H., **Subash, U.**, & Poutous, M. K., " On-sky evaluation of AWACS-Duo (dual-unit arrayed wide-angle camera system),"*Advances in Optical and Mechanical Technologies for Telescopes and Instrumentation VI*, SPIE, **418–430** 13100 (2024).